UCLouvain

epl

École polytechnique de Louvain

Study, design and characterization of a CMOS vibration and dynamic strain sensing microsystem

Author: **Thomas Degouys**
Supervisor: **Denis Flandre**
Readers: **Ottilie Bonfanti, Laurent Francis, Nicolas Roisin**
Academic year 2023–2024
Master [120] in Electrical Engineering

Abstract

Structural Health Monitoring is one of the most important tools for maintaining the safety and integrity of structures, such as in the fields of civil engineering or aerospace. Because the consequences of inadequate structural integrity monitoring leading to failure can be devastating, it is important to be able to detect the smallest defect in a structure as quickly as possible. An increasing number of powerful technologies are emerging in the field of structural monitoring.

This work is based on the study and dynamic characterization of strain sensor exploiting the piezoresistive effects of silicon in CMOS technology. Silicon is a semiconductor material with a high sensitivity to deformation, mainly due to its intrinsic piezoresistive properties, which derive from its crystalline structure and the modulation of charge carrier mobility under stress. The combination of these properties with the ease of integration of silicon into electronic systems makes it an ideal candidate for use in strain sensors.

The two main objectives and results of this work are: firstly, to develop a model based on an experimental setup consisting in a vibration generator, which is simulated by a piezoelectric actuator, and a strain sensor. An initial model has been established using a simple silicon strain gauge as a sensor with a gauge factor of 150. The model has been studied, simulated, tested and validated in the WELCOME laboratories at UCLouvain. Secondly, the strain gauge has been substituted with a CMOS strain sensor developed and patented at UCLouvain. This is a self-biased current reference circuit with a high supply rejection based on a β-multiplier configuration. Two distinct topologies have been analysed. The first involves eight transistors and a resistor, while the second is a full-transistor configuration. These devices demonstrate a gauge factor of over 300 in a previous work. The frequency responses of the two topologies have been extracted over a wide frequency range while subjected to excitations, ranging from a few hertz to hundreds of kilohertz. An additional static operation study at high temperatures, up to 80°C, and a differential analysis before and after bonding the sensor have been carried out.

Acknowledgements

First of all, I would like to sincerely thank my supervisor, Prof. Denis Flandre, who aroused my interest and enthusiasm for this subject which has given me so much both intellectually and practically. Many thanks for all the advice throughout the year and for the resources you enabled me to use to develop my skills in this field.

I would like to extend a special thank you to Nicolas Roisin for guiding me through the whole year. His motivation and exemplarity have been an endless source of inspiration throughout this journey. I also wish to thank Ottilie Bonfanti for dedicating her time to my work and for consistently responding to my requests with remarkable speed.

The completion of this work also marks the end of my academic career. I would also like to thank all the people without whom these years could not have been what they were. Thank you to all my course colleagues and peers met in extra-academic activities.

And of course, most importantly, my deepest thanks go to my family. In particular my parents, my brother and my girlfriend, who never doubted me for even a single second. Even though for an electronic engineering student, a lot can happen in a second, on a human scale I understood and felt the strength of their support. The end of this thesis is a reflection of the confidence they have shown in me all these years.

Contents

Abstract **i**

Acknowledgements **ii**

Contents **iv**

List of Figures **vii**

List of Tables **viii**

Nomenclature **ix**

Introduction **1**

1 State of the art **3**
1.1 Dynamic strain analysis in structural health monitoring for damage detection and localization 4
1.1.1 Overview 4
1.1.2 Frequency response function 6
1.1.3 Mode shape curvature method 9
1.1.4 Frequency response function shape curvature method 11
1.2 Overview of dynamic strain monitoring sensors. 12
1.2.1 Accelerometers 12
1.2.2 Fiber Bragg grating sensor 19
1.2.3 Sensor comparison 22
1.3 Objectives of this work 23

2 Vibration and dynamic strain analysis of semiconductor strain gauge **24**
2.1 Silicon strain gauge fundamentals 24
2.1.1 Piezoresistive effect in silicium 24
2.1.2 Non-idealities in strain gauge 27
2.2 Piezoelectric actuator model 28
2.2.1 Modelisation of the piezoelectric actuator 30
2.2.2 Mechanical noise in actuator 31
2.3 Experimental methodology 32
2.3.1 Setup 33

2.3.2 Semiconductor strain gauge . . . 34
2.3.3 Piezoelectric actuator . . . 36
2.4 Measurements and results . . . 37
2.4.1 Extraction methodology . . . 37
2.4.2 Experimental model . . . 40
2.4.3 Results . . . 44
2.4.4 Conclusion . . . 50

3 Characterization and dynamic strain analysis of the CMOS strain sensor 52
3.1 Theoretical specifications of the CMOS strain sensor . . . 52
3.1.1 Impact of strain on transistor operation . . . 54
3.1.2 Current equations for β_R topology . . . 54
3.1.3 Current equations for β_+ topology . . . 56
3.1.4 Temperature and dopant dependencies in CMOS strain sensor . . . 56
3.2 Experimental methodology . . . 60
3.2.1 Static analysis setup . . . 60
3.2.2 Dynamic analysis setup . . . 60
3.3 Measurements and results . . . 63
3.3.1 Temperature testing and differential analysis with glued device . . . 63
3.3.2 UMC180 sensor under dynamic strain characterization . . . 67
3.4 Conclusion and recommendations . . . 71

Conclusion 73

Bibliography 75

List of Figures

1.1 Structural health monitoring system process flow from [6]. 4
1.2 Classification of structural damage detection methods [7]. 5
1.3 A schematic of a parametric vibration-based damage detection methods [7]. 6
1.4 Single-degree-of-freedom mass-spring-damper system. 7
1.5 Sweep sinusoidal and impulse signals on the left and their Fourier transform on the right. 8
1.6 Typical FRFs of undamaged (dashed line) and different levels of damages (solid lines) beams from [16]. 9
1.7 Two mode shapes representation (modes 2 and 3) and an example of mode shape difference usage under three damage locations on three structures from [19]. 10
1.8 Beam analysed from [11] with sensor locations from 1 to 13 and damage locations highlighted by yellow dots. 10
1.9 Numerical and experimental values of the absolute difference method (ADM) indicator for the first three modes in the damage scenarios D1 (a) and D2 (b). Vertical red lines indicate damage locations [10]. 11
1.10 Simulation results obtained using FRFSCM on the left and number of maximum occurrences on the right from [10]. 12
1.11 Schematic representation of the structure of an accelerometer. 13
1.12 Accelerometer relative displacement frequency response reproduced from [22]. 14
1.13 Illustration of the dimensional change in a conductor with an applied force reproduced from [26]. 15
1.14 Three-dimensional schematic of a piezoresistive accelerometer on the left and the same system under stress on the right using finite element analysis from [28]. 16
1.15 Accelerometer structure with capacitive sensing reproduced from [31] on the left and an exemple of a capacitive accelerometer with lateral sensing technique from [30] on the right. 17
1.16 Longitudinal (left) and transverse (right) configurations of piezoelectric sensor from [25]. 19
1.17 Schematic of signal conditioning circuit for piezoelectric sensor reproduced from [34]. 20
1.18 Schematic of the working principle of Fiber Bragg grating sensors, and its response to strain from [37]. 21

2.1 Longitudinal π_l and transverse π_t piezoresistive coefficients for an P-type silicon on the left and an N-type silicon on the right at room temperature in (001) silicium wafer [23]. 26
2.2 Typical noise density curve of a piezoresistor from [72]. 28
2.3 Mechanical representation of a piezoelectric actuator reproduced from [73]. 29
2.4 Electrical representation of a Piezoelectric actuator reproduced from [73]. . 30
2.5 Butterworth Van Dyke (BVD) model of the piezoelectric actuator. 31
2.6 Setup for dynamic characterization of the silicon gauge strain sensor. . . . 33
2.7 Silicon gauge on actuator setup. 33
2.8 Scheme of the connections for the silicon gauge experimental setup. 34
2.9 Dimensions of B-series of gauge length of 2.6mm from BMC sensor [39]. . . 35
2.10 Technical draws and picture of the actuators from [65]. 36
2.11 Measurement example composed of the generator output in blue and the amplifier output in dark blue with the values displayed on the left y-axis. And the output voltage of the gauge in orange displayed on the right y-axis. 39
2.12 Flow diagram of the data extraction methodology. 40
2.13 Equivalent Circuit of the actuator setup. 40
2.14 Equivalent circuit of the actuator setup without the amplifier used. 42
2.15 Equivalent Circuit of the actuator setup with the amplifier. 42
2.16 Gain Bode diagrams on the left and phase Bode diagrams on the right for the two setup presented. 43
2.17 System block diagram. 43
2.18 Equivalent circuit of the setup with amplifier and a series resistor connected to the amplifier output. 45
2.19 45
2.20 Frequency response of the system for three different configurations simulated on the left and measured on the right. 46
2.21 The Bode phase plot of the setup for the case where the amplifier is not included on the left, and for the case where the amplifier is included on the right. 48
2.22 The Bode phase plot of the setup with the amplifier and the series resistor. 48
2.23 Silicon gauge measurement noise extraction. 49
2.24 Signal-to-noise ratio on the left and experimentally estimated noise power on the right as a function of the frequency. 50

3.1 β-multiplier reference circuits. β_R topology with polysilicon resistor R on the left and full-transistor implementations β_+ topology on the right. The reference currents are, respectively, written I_{β_R} and I_{β_+} [63]. 53
3.2 Evolution of carrier concentration in a semiconductor as a function of temperature reproduced from [85]. 58
3.3 Correction factor $P(N,T)$ as a function of doping concentration and temperature for (a) p-type silicon and (b) n-type silicon from [72]. 58
3.4 PM8PS prober employed for static characterization of the CMOS strain sensor. 60
3.5 Setup for dynamic characterization of the CMOS strain sensor. 60

3.6 Assembly of the CMOS strain sensor on the piezoelectric actuator. 61
3.7 Scheme of the dynamic experimental setup for the CMOS sensor. 61
3.8 Top view (a), front view (b) and side view (c) of the assembly. 62
3.9 Flow diagram of the data extraction methodology for the temperature testing. 63
3.10 Impact of temperature on the current of the two topologies, with no strain applied between 25 and 80°C in 5°C steps. Analytically computed and measured results on the evice not glued yet. 64
3.11 Impact of bonding the device to a steel strip at different temperatures on the current of the β_R-multiplier. Figure above: Currents measured before and after bonding and current computed after bonding. Figure below: difference between the measured currents and the computed currents before and after the bonding of the device. 66
3.12 Impact of bonding the device to a steel strip at different temperatures on the current of the β_+-multiplier. Figure above: Currents measured before and after bonding and current computed after bonding. Figure below: difference between the measured currents and the computed currents before and after the bonding of the device. 66
3.13 Equivalent circuit of the actuator setup without the amplifier used. 68
3.14 Bode diagram of the system frequency response using LTSpice. 68
3.15 Frequency response of the system measured by the CMOS strain sensor. Measurements of the β_R-multiplier in blue and the β_R-multiplier in orange. 69
3.16 Signal at the input of the piezoelectric actuator in green solid line and its simulated signal on the basis of the transfer function in green dashed line. Voltage measured at a 100kΩ resistor through which the output current of the β_R-multiplier in blue passes. 70
3.17 Signal at the input of the piezoelectric actuator in green solid line and its simulated signal on the basis of the transfer function in green dashed line. Voltage measured at a 100kΩ resistor through which the output current of the β_R-multiplier in orange passes. 70

List of Tables

1.1 Strain sensor performances comparison. 22

2.1 Piezoresistivity coefficients for bulk silicium (10^{-11}Pa) at room temperature for the [110] crystallographic direction from [71]. 26
2.2 Main parameters of the *BPY_1000_2.6_U_I_RL* gauge from BMC [39]. . 35
2.3 Longitudinal and transverse piezoresistive coefficients of silicon in different crystallographic directions from [25]. 35
2.4 Main parameters of the *P-882.11* actuator from Physik Instrumente [65]. . 36
2.5 Parameters of the Butterworth Van Dyke model of the *P-882.11* piezoelectric actuator from Physik Instrumente.. 41

3.1 Main parameters of the *P-882.51* actuator from Physik Instrumente [65]. . 62
3.2 Computed, theoritical from [63] and experimental temperature sensitivities of the two studied topologies. 65
3.3 Parameters of setup of the dynamic analysis of the CMOS strain sensor and the Butterworth Van Dyke equivalent topology of the *P-882.51* piezoelectric actuator from Physik Instrumente. 68

Nomenclature

List of abbreviations

ADM	Absolute difference method
CMOS	Complementary metal oxide semi-conductor
DOF	Degree of freedom
FBG	Fiber Bragg grating
FRF	Frequency response function
FRFSCM	Frequency response function shape curvature method
IEEE	Institute of Electrical and Electronics Engineers
MSCM	Mode shape curvature method
SDOF	Single degree of freedom
SHM	Structural health monitoring
TCR	Temperature coefficient of resistivity
VDD	Vibration-based damage detection
WELCOME	Wallonia ELectronics & COmmunications MEasurements

List of symbols

α	Electro-mechanical coupling factor
α_H	Hooges's factor
α_{th}	Coefficient of thermal expansion
ϵ	Absolute permittivity
Λ	Grating period

λ_B	Bragg resonance wavelength
ν	Poisson's ratio
ω	Angular frequency
ϕ	Phase
$\phi_{i,j}$	Modal displacement
Π	Tensor of piezoresistive coefficients
π	Piezorestive coefficient
ρ	Resistivity
σ	Stress
σ_e	Electrical conductivity
ε	Strain
ζ	Damping ratio
A	Area
a	Acceleration
C	Capacitance
c	Stiffness
D	Electric displacement
d	Damping coefficient
d	Piezoelectric coefficient
E	Electric field
E	Energy
E	Young modulus
F	Force
F	Input excitation
f	Frequency
H	Transfer function
h	Distance

I	Electrical current
i	Electrical current
J	Current density
K	Gauge factor
k	Stiffness constant
k_b	Boltzmann constant
L	Length
m	Mass
N	Number of carriers or concentration of doping atoms
n_{eff}	Effective refractive index
p_{ij}	Pockel's coefficient of the stress-optic tensor
Q	Quality factor
q	Electrical charge
R	Resistance
s	Elastic compliance
T	Temperature
t	Time
V	Voltage
v	Velocity
W	Width
x	Displacement
Y	Admittance matrix

Introduction

Structural Health Monitoring (SHM) is a critical tool for maintaining the safety and integrity of structures, particularly in fields such as civil engineering and aerospace. Given the potentially devastating consequences of structural failure, it is imperative to detect even the smallest defects as early as possible. Numerous advanced technologies are being developed for structural monitoring, among which this work focuses on a sensor exploiting the piezoresistive properties of complementary metal-oxide-semiconductor (CMOS) transistors to detect deformation. This sensor is particularly notable for its compact size, low power consumption, and high sensitivity.

The first chapter provides an overview of structural health monitoring techniques and the various types of sensors used in this field. Special attention is given to dynamic structural analysis, introducing the fundamental principles that govern sensor operation and offering a comparative analysis of their performances. This context sets the stage for the technical investigations that follow.

The second chapter presents the development of an initial model for the dynamic characterization of strain sensors which is based on the piezoresistive properties of silicon. It includes a detailed study of a silicon strain gauge with a gauge factor of 150, combined with a piezoelectric actuator to simulate mechanical deformations. The actuator's behavior is reduced to a simplified electrical model, which is then simulated using LTSpice and experimentally validated in the Wallonia ELectronics & COmmunications MEasurements (WELCOME) laboratories at UCLouvain. The experimental setup and methodologies studied in this chapter are intended to determine the accuracy and reliability of the model developed, and also lay the foundations for the dynamic analysis and characterisation that will be used in the third chapter.

The final chapter is dedicated to an in-depth analysis and dynamic characterization of the CMOS strain sensor. Building on the validated model from the previous chapter, this study employs an essentially identical setup to investigate two slightly different topologies of the sensor, both developed and patented by UCLouvain. These topologies are based on self-biased current reference circuits employing a β-multiplier configuration, which enables the sensor to achieve a gauge factor exceeding 300, along with a high power supply rejection ratio. The chapter includes a vibration analysis covering a frequency range from a few hertz to tens of kilohertz. In addition, the sensor's thermal behavior and differential response before and after bonding are characterized. These thermal static

analyses are conducted using I-V measurements from a low-signal probe station, providing a comprehensive understanding of the sensor's temperature dependencies and its overall performance for temperatures up to 80°C.

Chapter 1

State of the art

The CMOS strain sensor used in this work has the advantage of low power consumption, is very compact and very sensitive. However, it is much more expensive than a conventional metal or semiconductor strain gauge, which is already widely used in the structural health monitoring field [1]. Consequently, the sensor must be employed in a context where its advantages over other sensors can compensate for its cost.

Composite materials are defined as a combination of different materials forming a heterogeneous structure. The utilisation of these materials allows the enhancement of performance, including weight, strength, and durability, as well as other characteristics. This is achieved through the exploitation of the synergistic effects between the constituent materials [2]. Composite materials are increasingly used in the construction of aerospace structures, as conventional metallic materials are gradually being replaced [3].

The monitoring of aerospace composites is subject to more rigorous controls on the condition of structures than other fields [4]. The monitoring of composite materials is a challenging process due to the heterogeneous nature of their composition and the fact that damage to these structures may be less perceptible than damage to a conventional homogeneous structure, given their enhanced strength.

Furthermore, sensing mechanisms can be integrated into the manufacturing process of composite materials. The CMOS strain sensor, due to its small size, low power consumption and design, can be efficiently implemented within a wireless digital system that could provide real-time assessments of composite structures [5]. This would facilitate the early detection of damage, thereby reducing costs and preventing potential catastrophic failures. For these reasons, the CMOS strain sensor could be a suitable option for monitoring composite materials in the aerospace industry, for instance.

The objective of this initial chapter is to present a series of applications in which dynamic measurements of strain are employed, and to introduce two methods in which these measurements are used for the purpose of SHM. The methods presented are mainly used in damage detection and localisation. An overview of damage localisation methods is

presented. This is followed by a review of the various existing strain sensor technology used for damage localisation. Finally the objectives of this work are presented.

1.1 Dynamic strain analysis in structural health monitoring for damage detection and localization

1.1.1 Overview

Structural health monitoring is the practice of monitoring the operation of an infrastructure to ensure its integrity and proper functioning. It is a critical process for extending the lifespan of a structure, increasing its safety and efficiency through advanced maintenance monitoring. Furthermore, real-time detection of damage enabled by advanced SHM techniques prevents deterioration in the health of the structure. SHM is a fundamental aspect of civil engineering, employed in the monitoring of diverse structures such as bridges, turbines, and aviation infrastructure.

Structural health monitoring is a crucial process for detecting damage within an infrastructure that could potentially alter its properties. The health of the structure is assessed using a network of sensors that are strategically installed and positioned. The data collected is then processed and analysed in different ways, depending on the method used, and a report can be generated based on the results obtained. In summary, an SHM system can be conceptualised as shown in Figure 1.1.

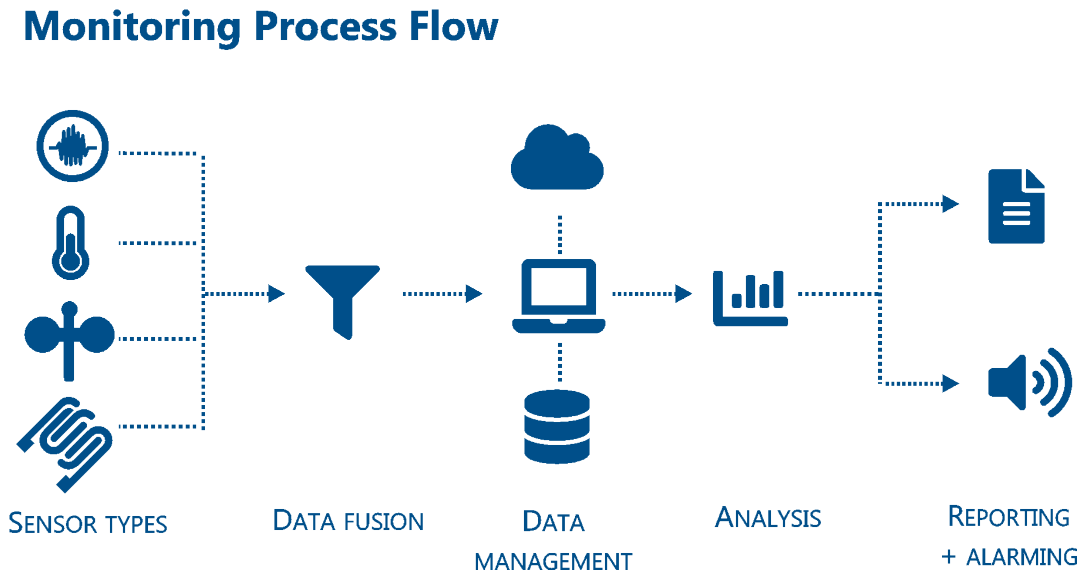

Figure 1.1: Structural health monitoring system process flow from [6].

This section is dedicated to the analysis of process flow and the algorithms used for damage detection and localisation. Damage detection methods can be classified into two principal categories [7]:

- Localised techniques for the identification of damage in discrete areas of the structure. These offer a high degree of accuracy in the assessment of damage, but have limited scope for coverage. The techniques include radiography, infrared thermography, ultrasonic testing, and so forth.
- Global methods facilitate the monitoring of an entire structure; however, they can result in the creation of more restrictive and complex systems. Global methods can be classified into two main categories: static-based and vibration-based methods.

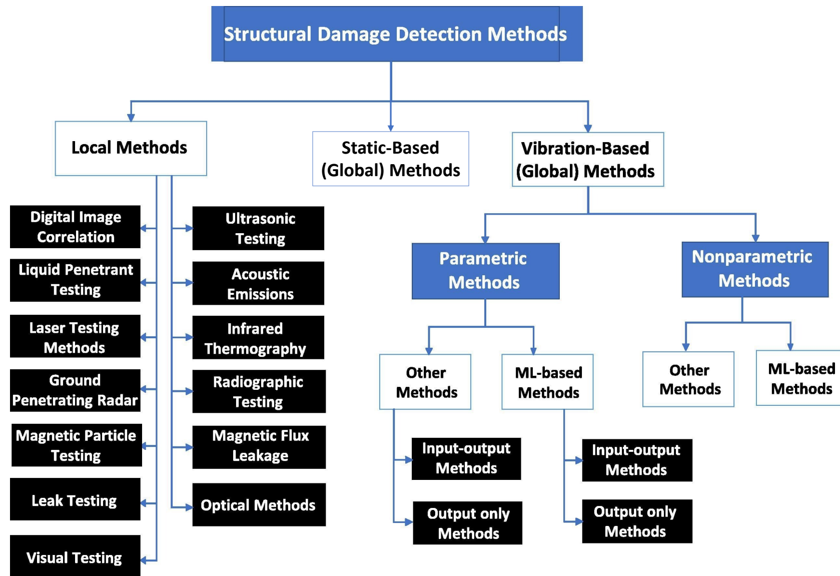

Figure 1.2: Classification of structural damage detection methods [7].

Vibration-based damage detection (VDD) methods are the most widespread in the field of SHM [7] and will be presented in this section. The objective of these methodologies is to ascertain and localise damage within a structure by identifying the dynamic parameters. The dynamic parameters correspond to the physical properties of the structure, such as modal frequencies, mode shapes, stiffness, and so forth. The fundamental principle of these methods is to compare the dynamic parameters of a structure undergoing testing with those of a known undamaged structure to apply an algorithm to detect damage and, if necessary, to locate it. Figure 1.3 provides a schematic illustration of such a system.

The initial work conducted in the field of structural dynamics entailed an investigation into the utilisation of a combination of natural frequency measurements and finite elements, which emerged in the late 1970s [8]. Further studies were conducted on vibration modes at the end of the 1980s, and finally, the analysis of the frequency response function was completed at the end of the 1990s. Advances in damage detection and location over the last few decades have consisted in developing methods based on the analysis of the dynamic parameters of structures extracted using frequency response function, natural frequencies or modes of vibration analysis, for example.

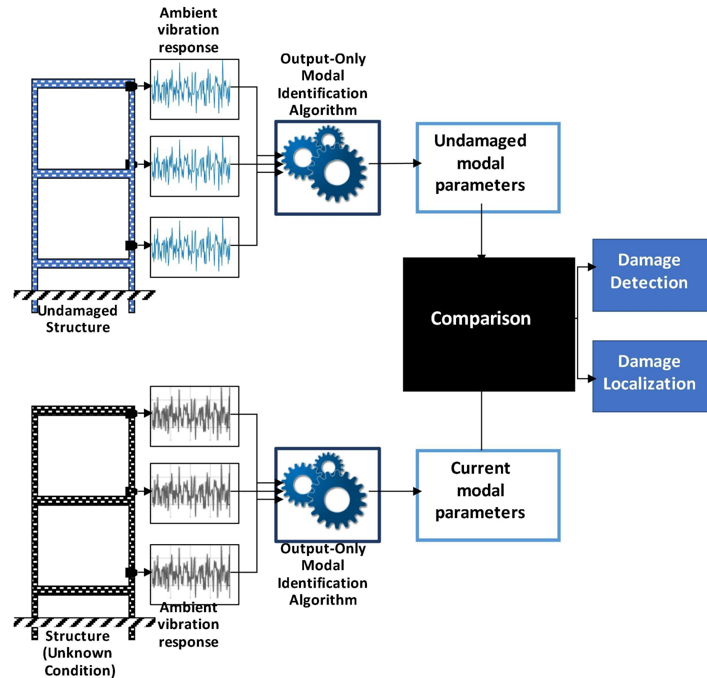

Figure 1.3: A schematic of a parametric vibration-based damage detection methods [7].

Two simple methods are presented in this work:

- The mode shape curvature method (MSCM) is a relatively straightforward technique that can be easily implemented, but it does require a high level of minimal damage to be detected due to measurement noise [9].

- The frequency response function shape curvature method (FRFSCM) provides a complete analysis of the dynamic parameters of a structure without the necessity of identifying the modal frequencies [10]. However, its effectiveness is highly dependent on the range of frequencies analysed, and a large network of sensors may sometimes be required to achieve good damage detection accuracy [11]. And it should be noted that artificial intelligence is also strongly implemented and developed to assist these types of methods in SHM [12].

1.1.2 Frequency response function

The frequency response function (FRF) is a measure of the response of a dynamic system to a given input excitation as a function of the frequency [13]. This function is employed to ascertain and identify resonant frequencies, shape modes, damping, and other characteristics of structures in SHM. It corresponds to the response $X(\omega)$ of a system following an excitation $F(\omega)$ normalised by the value of this excitation. Its mathematical definition is as follows [13]:

$$H(\omega) = \frac{X(\omega)}{F(\omega)} \tag{1.1}$$

In the context of a single-degree-of-freedom (SDOF) system, the response can be conceptualised as the relative displacement x of a system's proof mass of mass m, which depends on a set of dynamic parameters such as a spring with a stiffness constant k and a damper with a damping coefficient d. This relative displacement is divided by the input excitation, which is defined as the force F applied to the system.

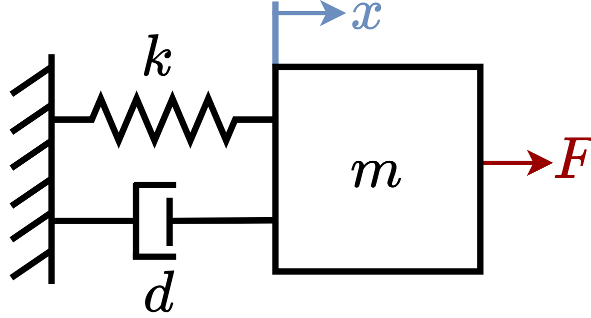

Figure 1.4: Single-degree-of-freedom mass-spring-damper system.

For such a system, the equation of motion is [14]:

$$m\frac{\partial^2 x(t)}{\partial t^2} + d\frac{\partial x(t)}{\partial t} + kx(t) = F \tag{1.2}$$

$$\frac{\partial^2 x(t)}{\partial t^2} + \frac{d}{m}\frac{\partial x(t)}{\partial t} + \frac{k}{m}x(t) = \frac{F}{m} \tag{1.3}$$

And defining the system's natural frequency ω_0 and damping ratio ζ:

$$\omega_0 = \sqrt{\frac{k}{m}} \qquad \zeta = \frac{d}{2m\omega_0} \tag{1.4}$$

Taking the Fourier transform of the equation 1.3, the frequency response function is given by:

$$\frac{X(\omega)}{F(\omega)} = \frac{1}{k}\left(\frac{\omega_0^2}{\omega_0^2 - \omega^2 + j(2\zeta\omega\omega_0)}\right) \tag{1.5}$$

In terms of amplitude and phase, equation 1.5 is expressed as follows:

$$\left|\frac{X(\omega)}{F(\omega)}\right| = \frac{1}{k}\left(\frac{\omega_0^2}{\sqrt{(\omega_0^2 - \omega^2)^2 + (2\zeta\omega\omega_0)^2}}\right) \qquad \phi = \arctan\left[\frac{2\zeta\omega\omega_0}{\omega_0^2 - \omega^2}\right] \tag{1.6}$$

The utility of the FRF is founded upon the equations presented above. Any given structure can be modelled by a DOF system, with its own dynamic parameters, including resonance

frequencies, stiffness, damping, and so forth. Under certain assumptions, a DOF system can be reduced to an SDOF system. Per example in some cases, this could applicable to the case of a beam in vibration [15].

The FRF can be employed to extract its parameters and conduct a dynamic characterization of the structure. A multitude of methodologies exist, but in the case of the two methods outlined in the following subsections, the objective is to undertake a differential analysis of these dynamic parameters between a structure deemed healthy and a potentially damaged structure to be tested. A variation in the damping factor or a shift in the resonance frequency could serve as an indicator of damage [16], thus enabling the implementation of preventive measures aimed at averting material losses and accidents.

The objective of the excitation is to cover a wide frequency range, thereby enabling a broad frequency response of the structure to be covered. In practice, this can be carried out in two different ways. Firstly, an impulse signal can be applied, which should be as narrow as possible and take the form of a Dirac delta pulse. This can be achieved, for example, by using an instrumented hammer. Secondly, a sinusoidal sweep excitation can be applied using a piezoelectric actuator [11].

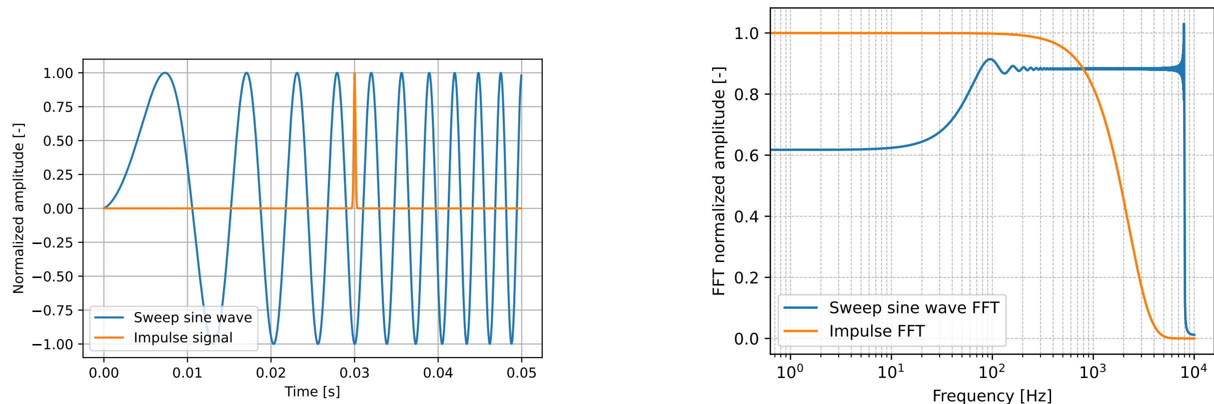

Figure 1.5: Sweep sinusoidal and impulse signals on the left and their Fourier transform on the right.

Once the excitation has been applied to the system, sensors such as accelerometers measure the strains undergone [11], and the FRF can be computed. Different frequency peaks can be used to determine the modes, as illustrated in Figure 1.6.

This method, which is widely used in dynamic testing, enables the dynamic parameters of a structure to be extracted efficiently for monitoring or testing bridge structures [17] for example. The frequency response function is used in SHM damage detection and localization methods because of its effectiveness in analysing the dynamic parameters of a structure. Figure 1.6 is used to determine the natural frequencies of the structure at the point where a resonance peak is found. The width of the peaks gives information about the damping, with a large peak corresponding to high damping and, invariably, a narrow

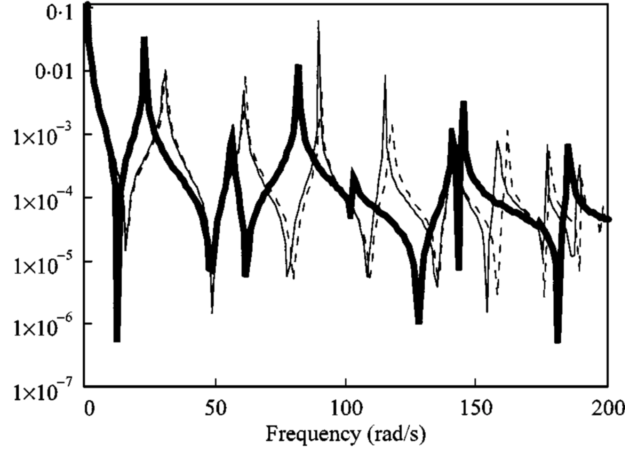

Figure 1.6: Typical FRFs of undamaged (dashed line) and different levels of damages (solid lines) beams from [16].

peak corresponding to low damping. The FRF phase combined with a graph such as the one shown in Figure 1.6 can also be used to determine the mode shapes of the structure.

1.1.3 Mode shape curvature method

This methodology employs the structural shape modes to identify and localise damage. The shape mode of a structure describes the relative displacement of the entire structure at a well-defined natural frequency. A beam of a specified length and configuration exhibits fixed and known natural frequencies [18] as shown in Figure 1.7. When subjected to an excitation at a frequency corresponding to one of these natural frequencies, the beam will begin to vibrate in a specific way. The benefit of exploiting these characteristics in this SHM method is that, in the event of beam damage, differences will be observed in the beam's behaviour when subjected to these excitations.

It is first necessary to know the frequencies at which these modes appear. Once the frequencies of the vibration modes have been identified, a differential analysis is then carried out between a healthy structure and the structure to be tested.

Let us consider a simple structure from [11], such as a beam of a given length, with a specified number of measurement points j ($j = 13$ in this example), as illustrated in Figure 1.8. The modal displacement, denoted by the variable ϕ_{ij}, is defined as the displacement relative to measurement point j at a certain modal frequency f_i. This corresponds to the magnitude of the imaginary part of the FRF. The difference in modal shapes between a healthy beam ϕ_{ij} and a damaged beam ϕ_{ij}^d for the ith modal frequency can be determined at each measurement point j:

$$\Delta\phi_{ij} = \phi_{ij} - \phi_{ij}^d \tag{1.7}$$

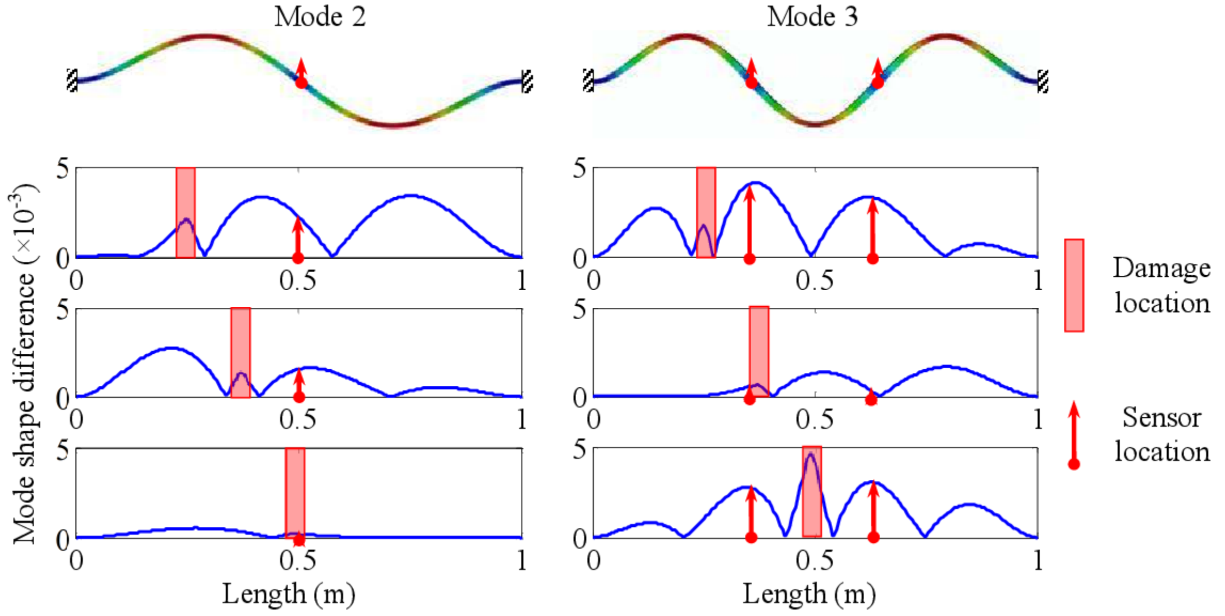

Figure 1.7: Two mode shapes representation (modes 2 and 3) and an example of mode shape difference usage under three damage locations on three structures from [19].

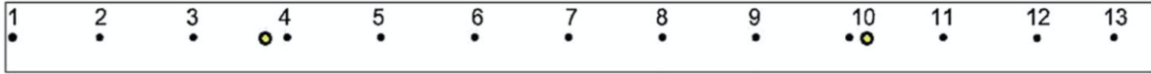

Figure 1.8: Beam analysed from [11] with sensor locations from 1 to 13 and damage locations highlighted by yellow dots.

The ith mode shape curvature corresponds to the second derivative of these values [11]:

$$\phi_{ij}^{''} = \frac{\partial^2 \phi_{ij}}{\partial x^2} \approx \frac{\phi_{i,j-1} - 2\phi_{ij} + \phi_{i,j+1}}{h^2} \tag{1.8}$$

With h the distance between the measurement point $j-1$ and $j+1$. The absolute difference method is introduced and is therefore defined as the absolute value of the difference between the mode shape curvature of the damaged beam and the healthy beam:

$$\Delta\phi_{ij}^{''} = |\phi_{ij}^{''} - \phi_{ij}^{''d}| \tag{1.9}$$

Measurement point j where higher values of absolute difference $\Delta\phi_{ij}^{''}$ are found correspond to the damage location. Figure 1.9 shows the numerical and experimental results obtained by [11] for two different damage scenarios.

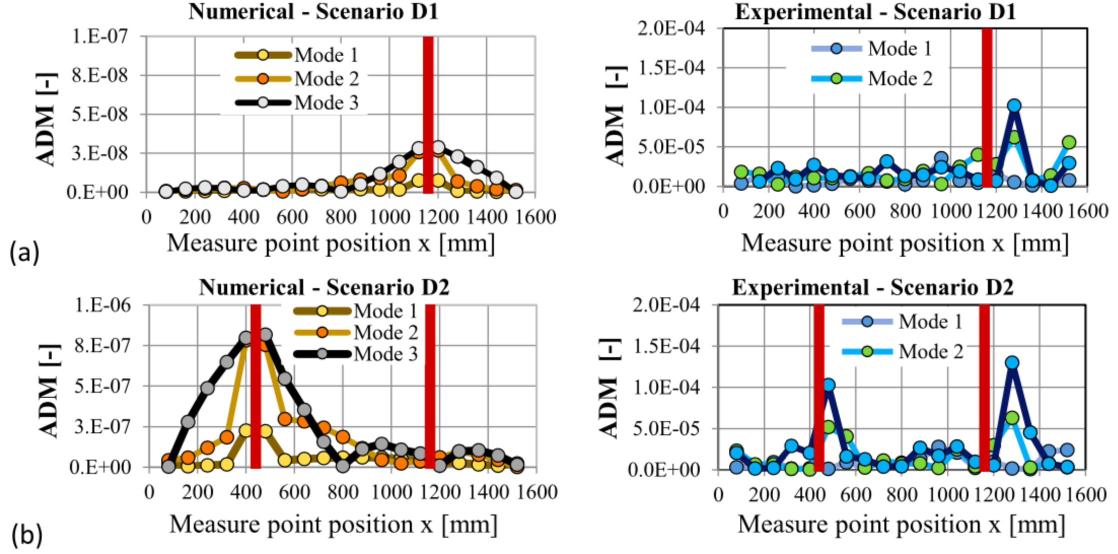

Figure 1.9: Numerical and experimental values of the absolute difference method (ADM) indicator for the first three modes in the damage scenarios D1 (a) and D2 (b). Vertical red lines indicate damage locations [10].

The case study above employs a one-dimensional demonstration of the shape curvature method. This method can also be applied to two-dimensional structure analysis. This enables the detection and localisation of damage in more complex structures, but also necessitates a more sophisticated implementation, requiring, in particular, the application of more complex algorithms to locate damage and being more sensitive to measurement noise [20, 21].

1.1.4 Frequency response function shape curvature method

Similar to the previous method, the FRF shape curvature method [10] is based on the assumption that the damage is located where the change in a mode shape function is greatest. However, in this method, the assumption is extended to a complete frequency range. The curvature of the FRF is still determined by a central difference approximation, resulting in the following equation:

$$H''_{ij}(\omega) = \frac{\partial^2 H_{ij}(\omega)}{\partial \omega^2} \approx \frac{H_{i-1,j}(\omega) - 2H_{ij}(\omega) + H_{i+1,j}(\omega)}{h^2} \tag{1.10}$$

In this case, the function $H(\omega)$ represents the frequency response function over a specified range of angular frequencies, ω. The value h corresponds to the distance between two measurement points, with i and j denoting the locations where the excitation for the measurement is applied. The absolute difference between the FRFs of a healthy beam and a damaged beam is computed by summing multiple measurements at different frequencies [10].

$$\Delta H''_{ij} = \sum_{\omega_k} |H''_{ij}(\omega_k) - H''^{d}_{ij}(\omega_k)| \tag{1.11}$$

Finally, if several forces are tested at different points, the results are added together:

$$FRF_SC_i = \sum_j \Delta H''_{ij} \tag{1.12}$$

It should be noted that these methods may necessitate the implementation of more rigorous post-processing algorithms to achieve the desired results. It is important to recognise that the results may be subject to measurement errors, which have the potential to distort them. One possible approach to consider is to determine the number of occurrences where the difference between the FRF of the damaged and healthy beams is at its maximum. This could help to counteract the aforementioned issues.

In this study case, [10] simulates the case of a beam equipped with eleven measurement points, a damage at point 7 and tests three different force points F3, F7 and F9. The result is shown in figure 1.10.

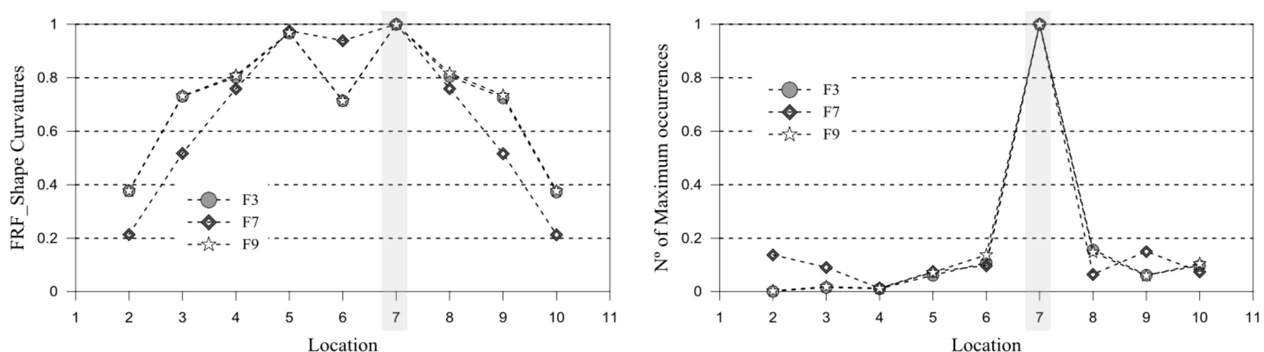

Figure 1.10: Simulation results obtained using FRFSCM on the left and number of maximum occurrences on the right from [10].

1.2 Overview of dynamic strain monitoring sensors.

1.2.1 Accelerometers

Accelerometers are a widespread technology employed in the domain of vibration-based damage detection. The operation of an accelerometer can be conceptualised as a mass-spring-damper system. When the system moves a specific distance $x(t)$, the proof mass of mass m will move a different distance $x_m(t)$ with a certain delay due to inertia phenomena, which are modelled by the spring with a stiffness constant k or the damper with a damping coefficient d, as illustrated in Figure 1.11.

The fundamental principle of accelerometers is to quantify the force applied to the structure they are monitoring. When the structure undergoes deformation, the system will also deform, and the accelerometer will determine the force applied as a function of the displacement of the system's mass. The working principle of accelerometers remains

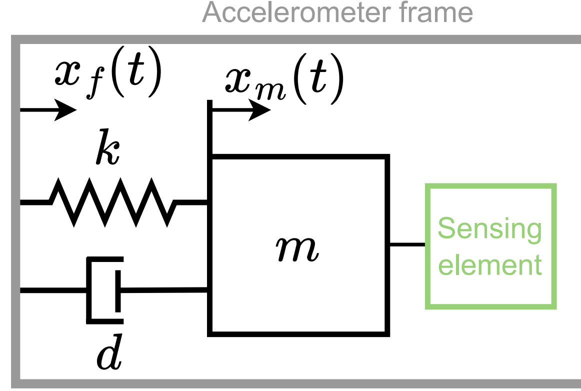

Figure 1.11: Schematic representation of the structure of an accelerometer.

identical; the only difference is in the sensing element that converts this displacement of the mass into useful information for defining the state of the system.

Using the proof mass displacement $x_m(t)$ and the accelerometer frame displacement $x_f(t)$, the relative displacement of the mass is computed:

$$x(t) = x_f(t) - x_m(t) \tag{1.13}$$

And the equation of motion of the structure is given by:

$$m\frac{\partial^2 x(t)}{\partial t^2} + d\frac{\partial x(t)}{\partial t} + kx(t) = f(t) = m\frac{\partial^2 x_f(t)}{\partial t^2} \tag{1.14}$$

With the external force applied $f(t)$ and the frame acceleration $a(t) = \frac{\partial^2 x_f(t)}{\partial t^2}$. By applying Laplace transform, the transfer function of the relative movement is expressed as:

$$\frac{X(s)}{F(s)} = \frac{1}{s^2 m + sd + k} = \frac{1}{m}\left(\frac{a(s)}{s^2 + \frac{\omega_0}{Q}s + \omega_0^2}\right) \tag{1.15}$$

With the natural frequency $\omega_0 = \sqrt{\frac{k}{m}}$ and the quality factor $Q = \frac{\omega_0 m}{d}$ to simplify the equation. The accelerometer already has mechanical limitations as the frequency response of this relative displacement of such a system has a resonant frequency.
Figure 1.12 shows three regions:

- At low frequency $\omega << \omega_0$ and under quasi-static conditions:

$$\frac{X(s)}{F(s)} \approx \frac{1}{m\omega_0^2} = \frac{1}{k} \tag{1.16}$$

  At low frequencies, the displacement only depends of the stiffness k which is a constant.

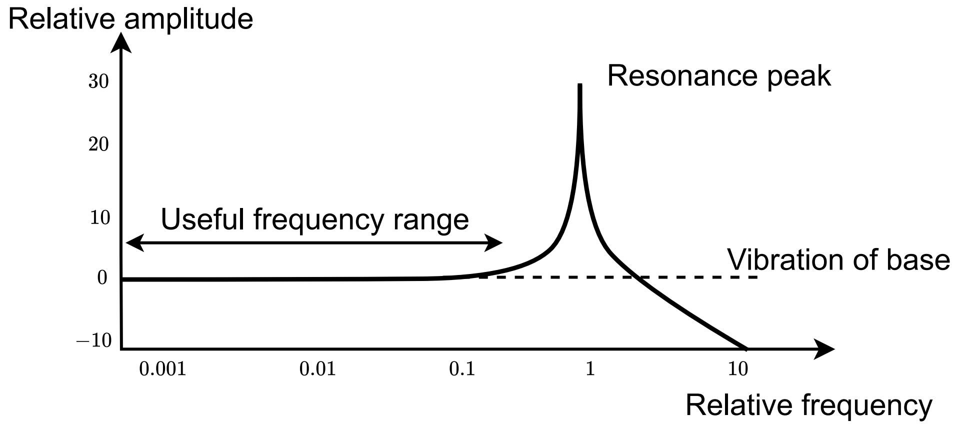

Figure 1.12: Accelerometer relative displacement frequency response reproduced from [22].

- When $\omega \approx \omega_0$:

$$\left|\frac{X(s)}{F(s)}\right| = \frac{1}{m\sqrt{\left(\frac{\omega_0^2}{Q}\right)^2}} = \frac{Q}{m\omega_0^2} = \frac{Q}{k} \tag{1.17}$$

  Around the resonant frequency, the transfer function depends on the quality factor, which is also linked to the damping factor via the equation:

$$\zeta = \frac{1}{2Q} = \frac{d}{2m\omega_0} \tag{1.18}$$

  This means that the width of the resonance peak is affected by this parameter.

- When $\omega >> \omega_0$:

$$\left|\frac{X(s)}{F(s)}\right| = \frac{1}{m\omega^2} \tag{1.19}$$

  The transfer function decreases with frequency.

The functional frequency range of the accelerometers is therefore below the resonant frequency ω_0, as illustrated in Figure 1.12. In addition to the operational and mechanical constraints previously outlined, the sensing element introduces further limitations. This section provides an analysis of the various types of sensors (piezoresistive, capacitive and piezoelectric) and their distinctive working principles, along with the constraints associated with each.

Piezoresistive sensing

This type of sensor exploits the piezoresistive nature of these materials, i.e. their capacity to alter their electrical resistivity when subjected to compression or stretching forces. Piezoresistive sensors exhibit high sensitivity, making them well-suited for applications requiring the detection of small strains [23]. This type of sensor demonstrates acceptable

frequency performance but is often more temperature-dependent than others [24]. The resistance of a material can be expressed as:

$$R = \rho \frac{L}{A} \tag{1.20}$$

Where ρ is the electrical resistivity, L is the length and A is the cross sectional area of the material. When subjected to small deformations, the change in the resistance can be expressed by [25]:

$$\frac{\Delta R}{R} \approx \frac{\Delta \rho}{\rho} + \frac{\Delta L}{L} - \frac{\Delta A}{A} \tag{1.21}$$

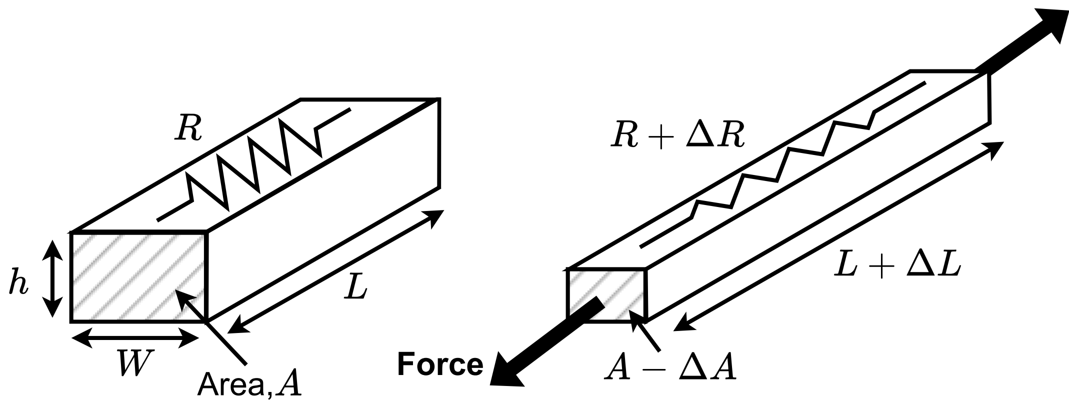

Figure 1.13: Illustration of the dimensional change in a conductor with an applied force reproduced from [26].

In the equation 1.21, all the denominators correspond to the nominal value, i.e. the value at rest before the strain is applied. Each of these three terms can be interpreted as:

- $\frac{\Delta \rho}{\rho}$, the change in electrical resistivity,
- $\frac{\Delta L}{L}$, the change in the relative length of the material which by definition corresponds to the strain ε,
- $\frac{\Delta A}{A}$, the change in the area of the material.

The gauge factor K is a unitless parameter used to determine the sensitivity of a strain sensor. It is defined as the ratio between the relative variation in resistance and the stress [25]:

$$K = \frac{\frac{\Delta R}{R}}{\varepsilon} = (1 + 2\nu) + \frac{1}{\varepsilon} \frac{\Delta \rho}{\rho} \tag{1.22}$$

Where ν, the Poisson's ratio, links the deformations of the area of the material with the perpendicular deformations. This expression is simplified in the case of certain materials

for which the variation in electrical resistivity can be neglected. As in the case of metallic materials, the expression is simplified to:

$$K \approx 1 + 2\nu \tag{1.23}$$

Given that the Poisson's ratio for these materials is between 0.25 and 0.5 [27], the maximum achievable gauge factor for metallic materials is approximately $K \approx 2$.

For more advanced materials, such as semiconductors, the variation in resistivity will have a greater impact, so if $\frac{1}{\varepsilon}\frac{\Delta\rho}{\rho} >> 1 + 2\nu$ the gauge factor for these materials is simplified to:

$$K \approx \frac{1}{\varepsilon}\frac{\Delta\rho}{\rho} \tag{1.24}$$

The change in resistivity is mainly due to material changes. The effect of strain on the resistivity of a material can be computed using the piezoresistivity coefficient π, which is defined as the change in resistivity per unit stress:

$$\pi = \frac{\frac{\Delta\rho}{\rho}}{E\varepsilon} = \frac{\frac{\Delta\rho}{\rho}}{E\frac{\Delta L}{L}} \tag{1.25}$$

With Young's modulus E, $\varepsilon = \frac{\Delta L}{L}$ is the strain corresponding to the change in length divided by the nominal length. A more detailed analysis of these coefficients is given in chapter 2 for silicon materials.

Piezoresistive accelerometers use piezoresistors, such as simple strain gauges, as their fundamental component. The innovative design of this type of sensor allows the effects described above to be exploited by integrating piezoresistors into the structure. The mass is connected to the system frame by flexural components on which the piezoresistors are placed [28]. When the system is subjected to a force, the frame will move and the mass will follow by inertia, but with a certain delay. Stresses will be applied to the flexural components and the piezoresistors will measure the induced stresses. Figure 1.14 illustrates this structure.

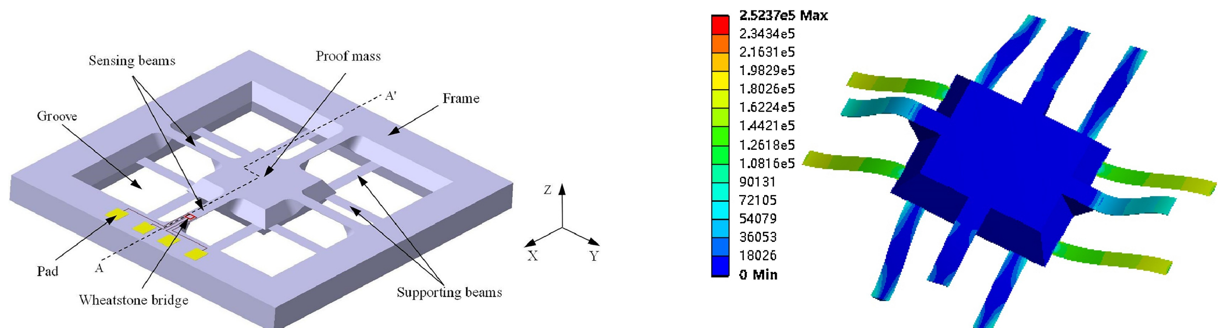

Figure 1.14: Three-dimensional schematic of a piezoresistive accelerometer on the left and the same system under stress on the right using finite element analysis from [28].

The integration of piezoresistors into Wheatstone bridges allows for the displacement linked to the vibrating structure to be monitored [29]. The variation in resistance of the piezoresistive elements, as previously mentioned, can be converted into a voltage by the bridge, which can then be used for the purpose of monitoring the strain applied to the system.

Capacitive sensing

A capacitive accelerometer functions in a manner similar to a piezoresistive accelerometer, with the exception that, rather than measuring a change in resistivity within a piezoresistor, it measures a variation in capacitance across capacitors.

A comb-type capacitive accelerometer such as the one represented in figure 1.15 is generally composed of an array of electrodes fixed to the accelerometer frame [30]. The proof mass is also connected to the frame but via suspension beams which allow it to move relative to the frame. In this frame of reference, the electrode array is fixed while the proof mass array is in motion.

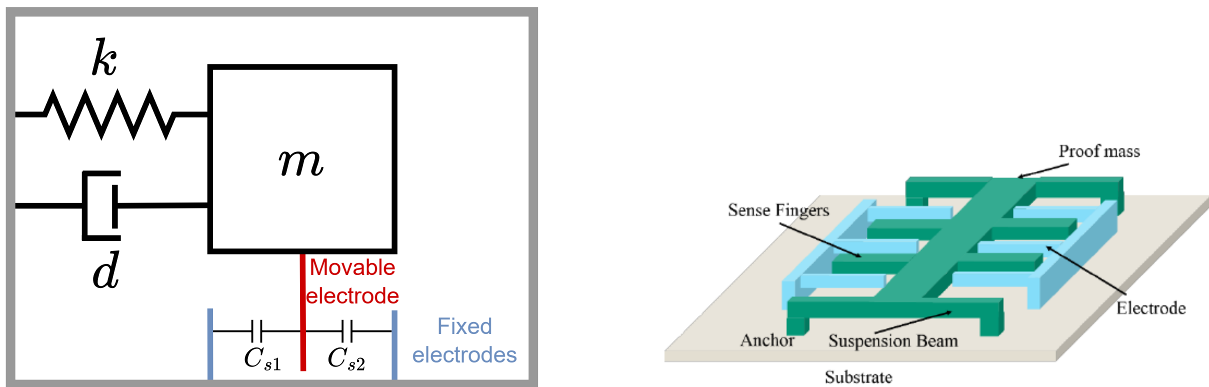

Figure 1.15: Accelerometer structure with capacitive sensing reproduced from [31] on the left and an exemple of a capacitive accelerometer with lateral sensing technique from [30] on the right.

When the system is in motion, the mass will move a certain relative distance x define in equation 1.13. The mobile electrode fixed to the mass will move towards one of the two fixed electrodes and away from the other. The value of a capacitor is defined as:

$$C = \epsilon \frac{A}{h} \tag{1.26}$$

With ϵ the permittivity of the dielectric, A the area of the capacitor plates and h the distance between these plates. Taking h to be the distance between the fixed electrodes and the movable electrode when the system is at rest. Assuming that the capacitors have the same area and the same dielectric material, the value of the capacitance can be expressed as a function of the relative distance of the mass x.

$$C_{s1}(x) = \epsilon \frac{A}{h+x} \qquad C_{s2}(x) = \epsilon \frac{A}{h-x} \tag{1.27}$$

The variation in capacity for a sense finger is given by:

$$\Delta C = C_{s2} - C_{s1} = \frac{\epsilon A}{h+x} - \frac{\epsilon A}{h+x} = C\left(\frac{1}{1-\frac{x}{h}} - \frac{1}{1+\frac{x}{h}}\right) \tag{1.28}$$

If $x << h$, the sensitivity of a capacitive accelerometer is therefore defined in [32, 30] by the ratio:

$$\frac{\Delta C}{C} = \frac{1}{1-\frac{x}{h}} - \frac{1}{1+\frac{x}{h}} \approx 1 + \frac{x}{h} - \left(1 - \frac{x}{h}\right) = \frac{2x}{h} \tag{1.29}$$

In steady state operation ($\omega << \omega_0$), the equation 1.14 is redefined and the relative displacement of the mass expressed as:

$$kx = m\frac{\partial^2 x_f(t)}{\partial t^2} \longrightarrow x = \frac{m}{k}\frac{\partial^2 x_f(t)}{\partial t^2} \tag{1.30}$$

The variation in capacitance is linked to the acceleration that the system undergoes by the equation:

$$\frac{\Delta C}{C} \approx \frac{2m}{kh}\frac{\partial^2 x_f(t)}{\partial t^2} \tag{1.31}$$

Piezoelectric sensing

Piezoelectric sensors are able to generate an electric field when subjected to mechanical deformation. Conversely, piezoelectric actuators can generate mechanical deformations when an electric field is applied to them. According to the IEEE Standard [33], the linear constitutive equations for piezoelectric material in stress-charge form are given by: Préciser accronymes IEEE

$$\begin{bmatrix} \boldsymbol{\sigma} \\ \mathbf{D} \end{bmatrix} = \begin{bmatrix} -\mathbf{d}^{\sigma} & \mathbf{s}^{\mathbf{E}} \\ \mathbf{d} & \boldsymbol{\epsilon}^{\sigma} \end{bmatrix} \begin{bmatrix} \boldsymbol{\varepsilon} \\ \mathbf{E} \end{bmatrix} \tag{1.32}$$

With strain $\boldsymbol{\varepsilon}$, compliance $\mathbf{s}$, piezoelectric coefficients $\mathbf{d}$, electric displacement $\mathbf{D}$, electric permittivity $\boldsymbol{\epsilon}^{\boldsymbol{\sigma}}$ and electric field $\mathbf{E}$. The superscript $\boldsymbol{\sigma}$ indicates a constant stress and the $\mathbf{E}$ a constant electric field. The majority of this type of sensor is made up of a piezoelectric material surrounded by two electrodes [25], which makes it possible to simplify the matrix equation 1.32 according to the two configurations shown in figure 1.16.

Considering the case of the longitudinal configuration with vertical direction 3, the matrix equation 1.32 is simplified to:

$$D_3 = d_{33}\varepsilon_3 + \epsilon E_3 \tag{1.33}$$

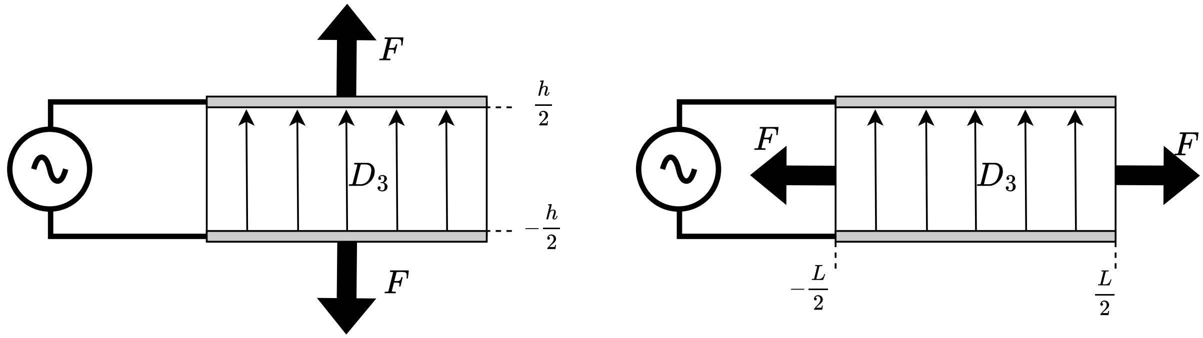

Figure 1.16: Longitudinal (left) and transverse (right) configurations of piezoelectric sensor from [25].

Strain and electrical displacements in other directions are neglected. The current within the transducer is given by:

$$i(t) = \frac{dq}{dt} = A\frac{dD_3(t)}{dt} \tag{1.34}$$

Where A is the area of the electrode. This expression can be simplified to:

$$i = Ad_{33}\frac{d\varepsilon_3}{dt} + A\epsilon\frac{dE_3}{dt} = Ad_{33}\frac{d\varepsilon_3}{dt} + C\frac{dV}{dt} \tag{1.35}$$

By simplifying that $E_3(t) = \frac{V(t)}{h}$ with V(t) the applied voltage, the capacitance of the transducer $C = \frac{A\epsilon}{h}$ can be computed. In practice, the current generated by the piezoelectric transducer must be followed by a circuit to process and exploit it. [34] proposes the circuit shown in figure 1.17. The current from the piezoelectric transducer passes through a transimpedance amplifier, a low-pass filter, a gain stage and finally is digitised through an ADC in this case.

Piezoelectric strain sensors are designed exclusively for the measurement of dynamic charges and are not suitable for use in the static regime. This is due to the fact that they only generate electrical charges when deformations are variable [35].

1.2.2 Fiber Bragg grating sensor

Fiber Bragg grating (FBG) is an optical sensor that is employed to measure a range of physical quantities, including strain within a structure or temperature [36]. The operational principle of the FBG sensor is based on the detection of a variation in the wavelength of the light emitted through the fiber once it has passed through the sensor. This process is illustrated in Figure 1.18.

In an FBG sensor, the fibre is exposed to an interference pattern of UV light, which induces periodic local changes in refractive index represented by the blue areas in Figure

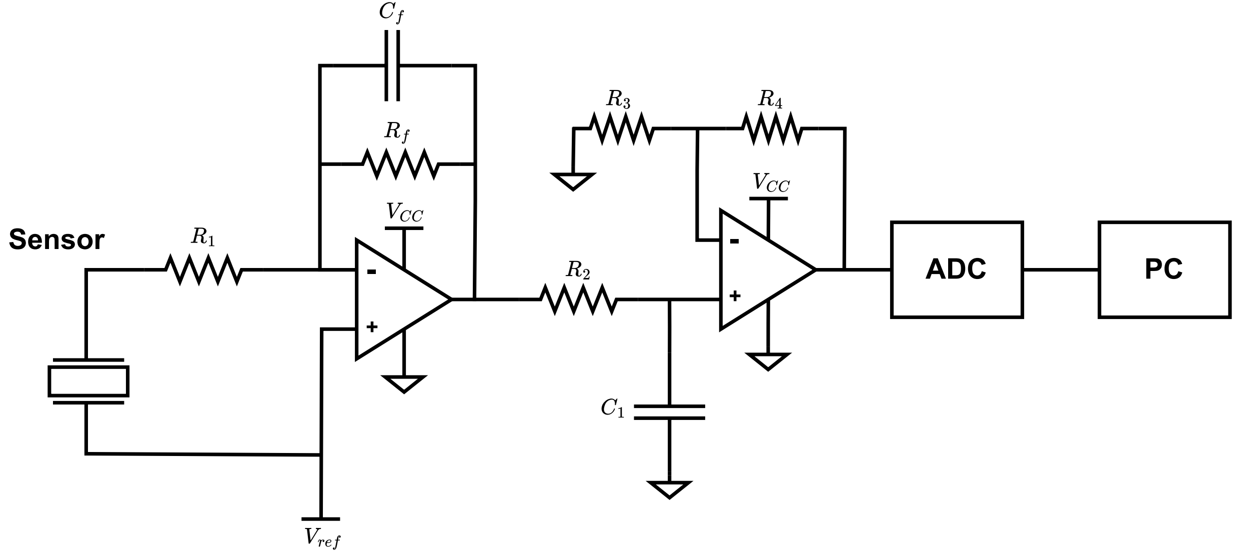

Figure 1.17: Schematic of signal conditioning circuit for piezoelectric sensor reproduced from [34].

1.18. Depending on the effective refractive index and the distance between these areas of refractive index variation, a certain wavelength of the incident light will be reflected. The Bragg resonance wavelength λ_B is the specific wavelength of the light reflected by the Bragg grating in the optical fibre [38] and is expressed as:

$$\lambda_B = 2n_{eff}\Lambda \tag{1.36}$$

With n_{eff} the effective refractive index and Λ the grating period, i.e. the distance between the zones of modified refractive index. Once deformed under a certain stress, the effective refractive index and the grating period will vary. According to the equation 1.36, the Bragg wavelength will also vary and reflect another part of the light spectrum. This allows for the analysis of the strain undergone by the sensor. Further details on equations can be found in [38]. The variation in Bragg wavelength is expressed as follows:

$$\Delta\lambda_B = 2\Lambda\Delta n_{eff} + 2n_{eff}\Delta\Lambda \tag{1.37}$$

The dependence of the effective refractive index on stress is defined as [38]:

$$\Delta n_{eff} = -\frac{n_{eff}^3}{2}\Delta\left(\frac{1}{n_{eff}^2}\right) \tag{1.38}$$

$$\Delta\left(\frac{1}{n_{eff}^2}\right) = [p_{12} - \nu(p_{11} + p_{12})]\varepsilon \tag{1.39}$$

Where p_{ij} are the Pockel's coefficient of the stress-optic tensor in i, j directions and ν the Poisson's ratio of the fiber. The variation of the grating period can be obtained:

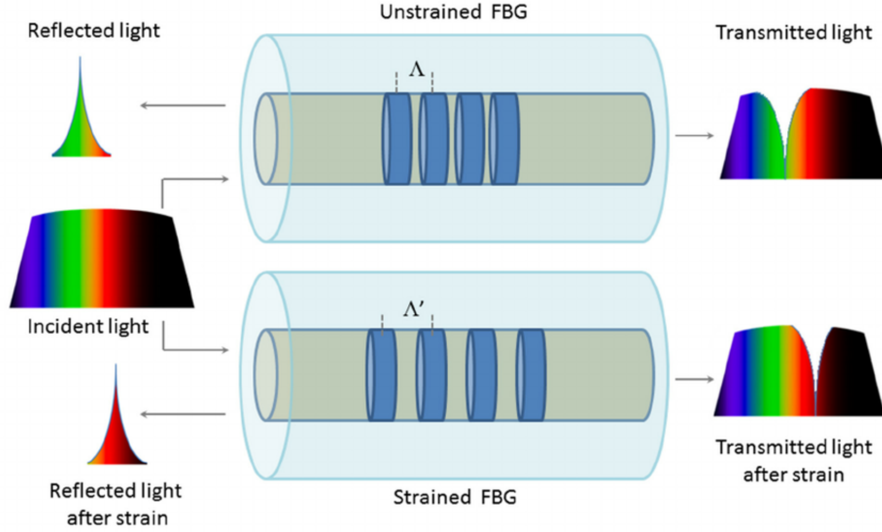

Figure 1.18: Schematic of the working principle of Fiber Bragg grating sensors, and its response to strain from [37].

$$\varepsilon = \frac{\Delta\Lambda}{\Lambda} \longrightarrow \Delta\Lambda = \varepsilon\Lambda \tag{1.40}$$

By injecting the equation 1.38 and 1.40 into the expression 1.37, the variation of the bragg wavelength as a function of stress is defined by:

$$\Delta\lambda_B = 2n_{eff}\Lambda\left(1 - \left(\frac{n_{eff}^2}{2}\right)[p_{12} - \nu(p_{11} + p_{12})]\right)\varepsilon \tag{1.41}$$

As mentioned above, the Bragg grating is also sensitive to temperature. The effective refractive index and the grating period depend on it:

$$\Delta n_{eff} = \frac{\partial n_{eff}}{\partial T}\Delta T - \frac{n_{eff}^3}{2}[p_{11} + 2p_{12}]\alpha_{th}\Delta T \tag{1.42}$$

$$\Delta\Lambda = \Lambda\alpha_{th}\Delta T \tag{1.43}$$

With α_{th} the coefficient of thermal expansion of the fibre. The expression 1.41 can be completed with the temperature dependence of the Bragg wavelength:

$$\begin{aligned}\lambda_B = 2n_{eff}\Lambda\Bigg[&\left(1 - \left(\frac{n_{eff}^2}{2}\right)[p_{12} - \nu(p_{11} + p_{12})]\right)\varepsilon \\ &+ \left(\alpha_{th} + \frac{\left(\frac{dn_{eff}}{dT}\right)}{n_{eff}} - \frac{n_{eff}^2}{2}[p_{11} + 2p_{12}]\alpha_{th}\right)\Delta T\Bigg]\end{aligned} \tag{1.44}$$

1.2.3 Sensor comparison

Sensor type	Sensitivity	Range	Bandwidth	References
Piezoresistive	1.4-150 $\frac{\text{m}\Omega}{\mu\varepsilon}$	$\pm 30000\mu\varepsilon$	10-100 kHz	[39, 40, 41, 42, 43]
Capacitive	0.265-1.8 $\frac{\text{fF}}{\mu\varepsilon}$	$\pm 1000\mu\varepsilon$	0.26-1 kHz	[44, 45, 46, 47, 48, 49, 50]
Piezoelectric	0.18-50 $\frac{\text{mV}}{\mu\varepsilon}$	$\pm 800\mu\varepsilon$	0.5Hz to 100kHz	[51, 52, 53, 54, 55, 56]
FBG	0.627-6.2 $\frac{\text{pm}}{\mu\varepsilon}$	$\pm 7000\mu\varepsilon$	1-1.88 kHz	[57, 58, 59, 60, 61, 62]

Table 1.1: Strain sensor performances comparison.

Piezoresistive sensors are less expensive than other types of sensors but have lower resolution. Despite this, they are widely used because of their low cost and robustness. Metal piezoresistive sensors can reach maximum deformations of up to 30000-50000 $\mu\varepsilon$, whereas semiconductors can reach 5000 $\mu\varepsilon$ but with much better resolution. As with the piezoelectric sensor, the power consumption will typically be influenced by the electronic interfaces employed for signal processing.

Capacitive strain sensors exhibit low power consumption, high sensitivity and a high response speed. However, they are susceptible to environmental and external field influences and are quickly limited in the deformations they can undergo due to their design. This specific sensor is less commonly encountered in practice, despite its low cost, principally due to the complexity of its design and the requirements of an appropriate detection circuit.

Piezoelectric sensors are employed in dynamic applications, as their structural and operational characteristics make it impossible to measure stable deformations over an extended period of time. The deformations generate a charge in the crystal of the piezoelectric material, which is susceptible to dissipation if it is not continually renewed. While they possess high sensitivity, piezoelectric strain transducers are more expensive than piezoresistive strain gauges. The intrinsic properties of piezoelectric transducers enable them to function without a power supply, as they are self-powered. However, the transducer must be accompanied by an electronic interface to make use of the generated charges, which will consume power.

Optical sensors, such FBG sensors, are able to accurately measure deformation and temperature variations. They are not affected by electromagnetic variations and can withstand environments that electronic sensors cannot. However, they are also highly susceptible to

damage, and packaging methods have been developed to protect them.

1.3 Objectives of this work

The following chapters of this work focus on the study of sensors that make use of the piezoresistive effects of silicon. The objective of the Chapter 2 is to develop an experimental setup for simulating and analysing the operation of these sensors in dynamic regimes. The setup includes a piezoelectric actuator for simulating the vibration of a system and a strain sensor. An initial study of these components was conducted to develop a model for characterising their operation. The setup is then configured and the system response is measured using two different sensors:

- A conventional strain gauge with a gauge factor of 150.
- A CMOS strain sensor with a low power consumption that has exhibited gauge factors over of 300 in previous works [63, 64].

In addition to the dynamic analysis, experimental noise estimates are analysed for the strain gauge case. A study was conducted to investigate the behaviour of the sensor as a function of temperature. This was achieved by first analytically calculating the impact of temperature on the sensor's operation, and then validating the results through experimental testing.

Chapter 2

Vibration and dynamic strain analysis of semiconductor strain gauge

The aim of this chapter is to develop and validate a reference test bench for the dynamic analysis of strain sensors, which will be used as a basis for characterizing the CMOS strain sensor in Chapter 3. This stage involves a commercial strain gauge from BMC Sensor [39] and a piezoelectric actuator from PI Ceramic [65] to generate controlled vibrations. By analyzing the dynamic strains and vibrations using the strain gauge, the aim is to establish a reliable model that can be extended to the CMOS sensor evaluation.

The first two sections explain the working principle of the silicon gauge and the piezoelectric actuator. A model is developed to represent the electrical and mechanical behaviour of the actuator. The third section describes the different elements that compose the setup. The final section integrates the experimental setup into the actuator model to predict the frequency response of the complete system, which is measured using the silicon gauge. Measurements of the frequency response of the sensor are discussed, and an estimate of the effect of noise on the measurements is shown.

2.1 Silicon strain gauge fundamentals

2.1.1 Piezoresistive effect in silicium

The resistivity of a material depends on the internal arrangement of its atoms and the intrinsic atomic properties, as well as the dynamics of the movement of charge carriers. Stress that alters these parameters results in a change in the resistivity of the material [66].

The formulation of the effect is derived from the expression that links the current density **J** and the electric field **E** by the matrix equation:

$$\mathbf{J} = \boldsymbol{\sigma_e} \cdot \mathbf{E} \tag{2.1}$$

$$\mathbf{E} = \boldsymbol{\rho} \cdot \mathbf{J} \tag{2.2}$$

Where $\boldsymbol{\sigma_e}$ represents electrical conductivity and $\boldsymbol{\rho}$ its inverse, electrical resistivity. Expressed in matrix form, the equation 2.2 becomes:

$$\begin{bmatrix} E_1 \\ E_2 \\ E_3 \end{bmatrix} = \begin{bmatrix} \rho_{11} & \rho_{12} & \rho_{13} \\ \rho_{21} & \rho_{22} & \rho_{23} \\ \rho_{31} & \rho_{32} & \rho_{33} \end{bmatrix} \begin{bmatrix} J_1 \\ J_2 \\ J_3 \end{bmatrix} \tag{2.3}$$

It can be demonstrated that in the case of a single crystal material with cubic symmetry, such as silicon [26], the terms from equation 2.3 can be simplified to yield: $\rho_{11} = \rho_{22} = \rho_{33} = \rho$. The application of mechanical stress or strain to the device will result in a variation in resistivity, which can be calculated using the resistivity tensor.

$$\begin{bmatrix} E_1 \\ E_2 \\ E_3 \end{bmatrix} = \begin{bmatrix} \rho + \Delta\rho_{11} & \Delta\rho_{12} & \Delta\rho_{13} \\ \Delta\rho_{21} & \rho + \Delta\rho_{22} & \Delta\rho_{23} \\ \Delta\rho_{31} & \Delta\rho_{32} & \rho + \Delta\rho_{33} \end{bmatrix} \begin{bmatrix} J_1 \\ J_2 \\ J_3 \end{bmatrix} \tag{2.4}$$

The resistivity value without mechanical load is represented by ρ, while the variations in resistivity due to piezoresistive effects are represented by $\Delta\rho_{i,j}$. The first chapter provided an introduction to piezoresistive sensing. By repeating the equation 1.25, it is possible to link the variation in resistivity to the stress knowing that the stress tensor $\boldsymbol{\sigma}$ is linked to the strain tensor $\boldsymbol{\varepsilon}$ via Young's modulus E in a case of elastic deformation by the formula [67]:

$$\boldsymbol{\sigma} = E\boldsymbol{\varepsilon} \tag{2.5}$$

The relative variation in resistivity is linked to stress by:

$$\frac{\boldsymbol{\Delta\rho}}{\boldsymbol{\rho}} = \mathbf{\Pi} E\boldsymbol{\varepsilon} = \mathbf{\Pi}\boldsymbol{\sigma} \tag{2.6}$$

With $\mathbf{\Pi}$ corresponding to the tensor of the piezoresistive coefficients. This tensor is initially of rank 4. The diamond atomic structure of silicon belongs to the hexoctahedral (O_h) crystal class, which is highly symmetrical [68]. This allows the tensor to be simplified significantly in the case of silicon. The tensor of the piezoresistive coefficients of silicon is reduced to three independent terms, and the matrix form of the equation referenced as equation 2.6 is written as follows:

$$\frac{1}{\rho} \begin{bmatrix} \Delta\rho_{11} \\ \Delta\rho_{22} \\ \Delta\rho_{33} \\ \Delta\rho_{12} \\ \Delta\rho_{13} \\ \Delta\rho_{23} \end{bmatrix} = \begin{bmatrix} \pi_{11} & \pi_{12} & \pi_{12} & 0 & 0 & 0 \\ \pi_{12} & \pi_{11} & \pi_{12} & 0 & 0 & 0 \\ \pi_{12} & \pi_{12} & \pi_{11} & 0 & 0 & 0 \\ 0 & 0 & 0 & \pi_{44} & 0 & 0 \\ 0 & 0 & 0 & 0 & \pi_{44} & 0 \\ 0 & 0 & 0 & 0 & 0 & \pi_{44} \end{bmatrix} \begin{bmatrix} \sigma_1 \\ \sigma_2 \\ \sigma_3 \\ \sigma_4 \\ \sigma_5 \\ \sigma_6 \end{bmatrix} \tag{2.7}$$

With the $\boldsymbol{\Delta\rho}$ and $\boldsymbol{\sigma}$ tensors expressed using Voigt's notation [69]. The matrix system is oriented along the cubic crystal axes, and thus requires the application of a transformation according to an arbitrary coordinate system. The useful area of the silicon device is typically oriented along a particular direction [70]. This allows for the expression of the relative variation in resistivity according to a longitudinal piezoresistive coefficient transverse to the direction of the device:

$$\frac{\Delta R}{R} = \pi_l \sigma_l + \pi_t \sigma_t \tag{2.8}$$

With the indices l and t corresponding to the longitudinal and transverse respectively in a specific crystallographic direction. After development [70], for example, these coefficients are expressed with regards to those of the cubic crystal axes system in the [110] crystallographic direction per example:

$$\pi_l = \frac{\pi_{11} + \pi_{12} + \pi_{44}}{2} \qquad \pi_t = \frac{\pi_{11} + \pi_{12} - \pi_{44}}{2} \tag{2.9}$$

The values of the piezoresistive coefficients for the case of low doped silicon in the [110] crystallographic direction are provided in the table 2.1.

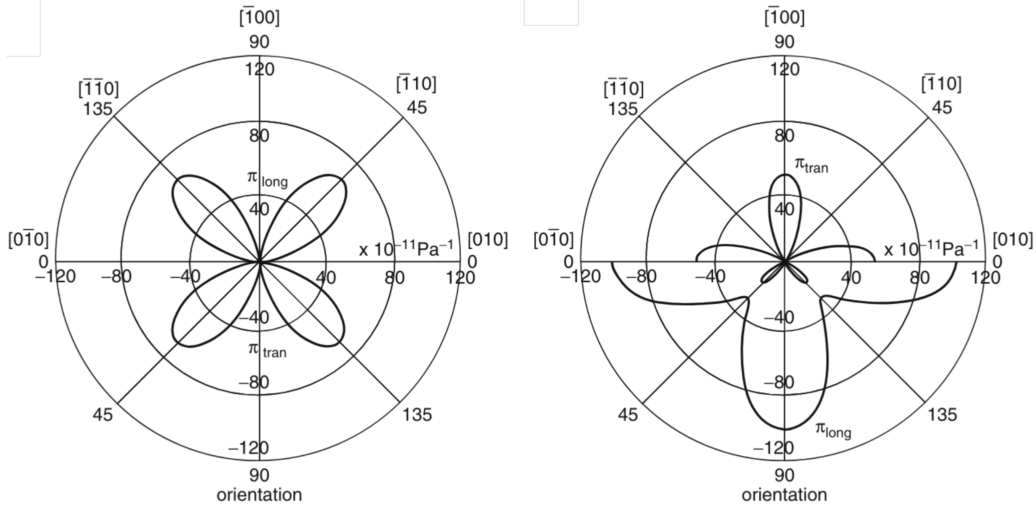

Figure 2.1: Longitudinal π_l and transverse π_t piezoresistive coefficients for an P-type silicon on the left and an N-type silicon on the right at room temperature in (001) silicium wafer [23].

Direction	π_{11}	π_{12}	π_{44}	π_l	π_t
P-type Si	-102.2	53.7	-13.6	-31.6	-17.6
N-type Si	6.6	-1.1	138.1	71.8	-66.3

Table 2.1: Piezoresistivity coefficients for bulk silicium (10^{-11}Pa) at room temperature for the [110] crystallographic direction from [71].

2.1.2 Non-idealities in strain gauge

The main disadvantage of using a semiconductor piezoresistive sensor is the introduction of noise through the resistor. Semiconductor components are subject to three main sources of noise [25]:

- Thermal noise
- Shot noise
- Flicker noise

Thermal noise

Thermal noise, also known as Johnson-Nyquist noise, is a common phenomenon in electronic devices. It is generated by the thermal agitation of charge carriers and can affect the performance of piezoresistive sensors by reducing the sensitivity [25]. Thermal noise is characterized as white noise, meaning that its spectral density is constant and independent of frequency. The noise voltage generator can be defined as follows:

$$\overline{v_n^2} = 4k_BTR \tag{2.10}$$

In this expression, the quantity k_B represents Boltzmann's constant, T denotes the temperature in Kelvin, and R is the value of the resistance.

Shot noise

In semiconductor gauges such as the one analysed in this section, shot noise can be defined as the random diffusion of carriers across a potential barrier at a metal-semiconductor interface. The noise current spectral density is defined by [25]:

$$\overline{i_n} = \sqrt{2q_eI} \tag{2.11}$$

It depends on the charge of an electron q_e and the current through the potential barrier. Across a resistor, the equivalent voltage noise is:

$$\overline{v_n} = \sqrt{2q_eI}R \tag{2.12}$$

This noise occurs when poor contacts are found between different interfaces on a component and depends on the current flowing through it.

Flicker noise - $1/f$ noise

In electrical components, flicker noise is caused by the random trapping and release of electrical carriers. It is frequency dependent, Flicker noise across a resistor can be expressed by experimental Hooges formula [25]:

$$\overline{v} = \sqrt{\frac{\alpha_H}{fN}}V \tag{2.13}$$

Where α_H is the Hooges's factor, N is the total number of carriers in the resistor, V is the voltage across it and f is the frequency. The Hooges factor depends on the process and the component material.

The intensity of the noise in question decreases as the frequency increases. In general, the noise will be dominant up to a certain frequency, denoted as f_c, which is the corner frequency. This is the frequency at which thermal noise or shot noise becomes dominant in relation to flicker noise. Figure 2.2 illustrates a typical curve for noise sources in a piezoresistor.

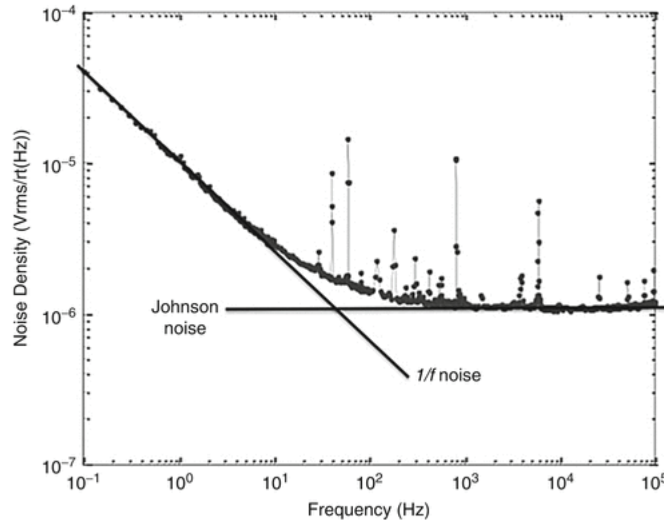

Figure 2.2: Typical noise density curve of a piezoresistor from [72].

2.2 Piezoelectric actuator model

An introduction to the piezoelectric effect and the constitutive equations were provided in order to present the piezoelectric sensor in section 1.2.1. These equations remain applicable in the context of the actuator. A piezoelectric actuator, as opposed to a piezoelectric sensor, is employed to transform electrical energy into mechanical energy. The objective of this section is to develop a representative model of the actuator for the purpose of analysing its dynamic behaviour. The following equations and models are presented and developed in [73]. The dynamic regime equations of a piezoelectric are expressed as:

$$\begin{aligned} m\frac{\partial^2 x}{\partial t^2} + d\frac{\partial x}{\partial t} + cx = F + \alpha V \\ \frac{1}{C_{elec}}[q - \alpha x] + R\left[\frac{\partial q}{\partial t} - \alpha\frac{\partial x}{\partial t}\right] = V \end{aligned} \tag{2.14}$$

With the force F, the mechanical stiffness c of the system, the mechanical displacement x, electro-mechanical coupling factor α, the applied electric voltage V , the electrical charge

q, the electrical capacitance C_{elec} and the resistance R which represents dielectric losses. We have taken into account the dynamical effects, i.e. the acceleration term $m\frac{\partial^2 x}{\partial t^2}$ which represents the inertia of the system, the structural damping $d\frac{\partial x}{\partial t}$ and the dielectric losses.

Mechanical representation

The figure 2.3 shows a mechanical representation of equation 2.14 from [73].

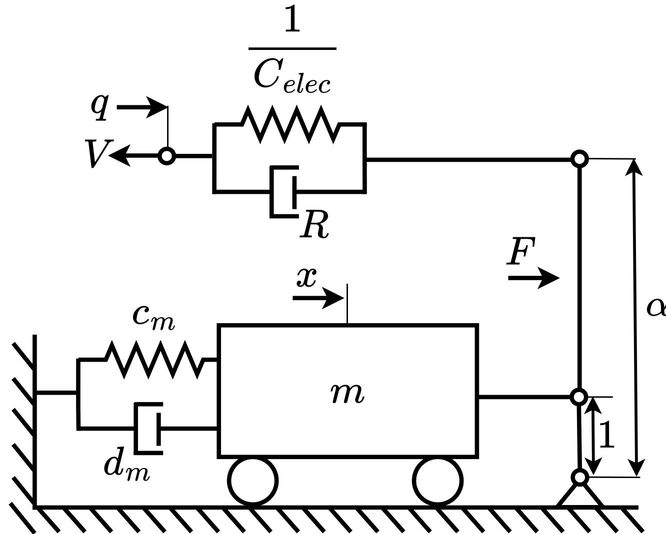

Figure 2.3: Mechanical representation of a piezoelectric actuator reproduced from [73].

This is a single degree of freedom model, which is applicable only to piezoelectric systems with a maximum of one vibration mode [73]. The mechanical representation considers the displacement x in only one direction. This analogy is considered valid for the piezoelectric actuator used in the experimental setup described in section 2.3, since it is assumed that the actuator can displace in only one direction.

Figure 2.3 depicts the mechanical components of the equation 2.14, which can be represented as a mass-spring-damper system. The modal mass represented by m, the modal stiffness represented by c_m, and the modal damping represented by d_m, are the key parameters of the mechanical behaviour within this system. The electrical capacitive behaviour of the piezoelectric material is represented by the shunted capacitance, C_{elec}, and the resistor, R. A lever is used to represent the electro-mechanical coupling. A multi-degree of freedom model could have been represented by the addition of mass-spring-damper systems [73].

Electrical representation

The figure 2.4 below shows an electrical representation of equation 2.14 from [73].
The integration of mechanical parts into the electrical representation is achieved through the introduction of coupled inductances for the electro-mechanical coupling, an inductance

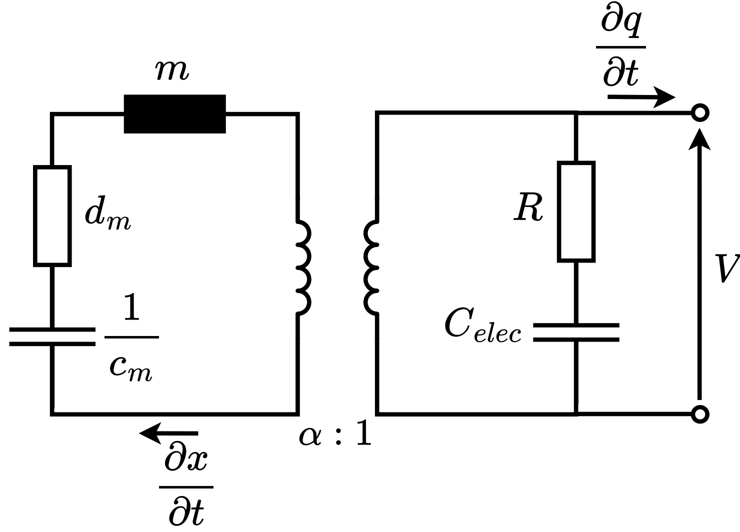

Figure 2.4: Electrical representation of a Piezoelectric actuator reproduced from [73].

for the modal mass, an impedance for the modal damping and a capacitor for the modal stiffness.

2.2.1 Modelisation of the piezoelectric actuator

On the basis of the two representations 2.3 and 2.4, it is possible to determine the well-known Butterworth Van Dyke model established in 1925 [74] which describes the electromechanical operation of the actuator. By expressing the current and velocity of the simplified electrical model of the actuator in figure 2.4 as:

$$I = \frac{\partial q}{\partial t} \qquad v = \frac{\partial x}{\partial t} \tag{2.15}$$

The dynamic behaviour of the system can be fully characterized using the matrix equation [73]:

$$\begin{pmatrix} I \\ v \end{pmatrix} = \begin{pmatrix} Y_{11} & Y_{12} \\ Y_{21} & Y_{22} \end{pmatrix} = \begin{pmatrix} V \\ F \end{pmatrix} \tag{2.16}$$

The admittance matrix of the system is constituted by four terms, the first of which, Y_{11}, represents the short-circuit impedance of the system. The term Y_{22} represents the short-circuit mechanical output impedance of the system. And the terms Y_{12} and Y_{21} respectively describe the electro-mechanical conversion and are identical. The mathematical expressions are defined on the basis of the matrix equation 2.16 and the electrical representation 2.4 from [73], as follows:

$$Y_{11} = \left.\frac{j\omega Q}{V}\right|_{F=0} = \frac{\alpha^2}{j\omega m + d_m + c_m/(j\omega)} + \frac{1}{R + 1/(j\omega C_{elec})} \tag{2.17}$$

$$Y_{12} = Y_{21} = \frac{j\omega x}{V} = \frac{\alpha}{j\omega m + d_m + c_m/(j\omega)} \tag{2.18}$$

$$Y_{22} = \left.\frac{j\omega Q}{F}\right|_{V=0} = \frac{1}{j\omega m + d_m + c_m/(j\omega)} \tag{2.19}$$

The objective of this section is to reduce the actuator operation to a simple electrical equivalent. Given that the system is excited with a specific voltage amplitude of V and that it is mechanically unloaded, with $F = 0$, it is possible to convert the mechanical component of Figure 2.4 in the electrical domain. This allows us to arrive at the Butterworth Van Dyke topology from Figure 2.5 [73].

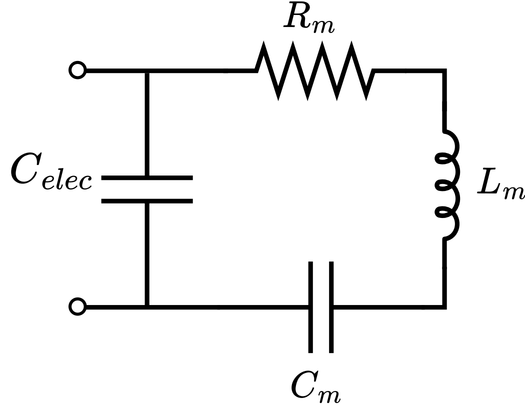

Figure 2.5: Butterworth Van Dyke (BVD) model of the piezoelectric actuator.

In practice, the dielectric losses are low and R is neglected [73]. The mechanical part composed of m, d_m and $\frac{1}{c_m}$ has been converted in the electrical part into L_m, R_m and C_m respectively and are defined according to the following expressions:

$$L_m = \frac{m_1}{\alpha^2} \qquad R_m = \frac{d_m}{\alpha^2} \qquad C_m = \frac{\alpha^2}{c_m} \tag{2.20}$$

The first term of the system's matrix admittance can be rewritten by identification:

$$Y_{11} = j\omega \left(C_{elec} + \frac{C_m}{1 + \omega C_m (jR_m - \omega L_m)} \right) \tag{2.21}$$

The presented topology will be used to model the behaviour of the actuator in the rest of this work.

2.2.2 Mechanical noise in actuator

A first overview of the characteristics of noise with a focus on thermal noise in electrical systems was provided with regard to the silicon gauge. It is also important to note

that mechanical systems are subject to noise issues too. The equipartition theorem of thermodynamics states that the average thermal energy for each degree [25] of freedom is:

$$E_{th} = \frac{1}{2}k_B T \tag{2.22}$$

Once more with the Botzmann constant k_B and the temperature T. In this context, the degree of freedom can be defined as the way in which the system is capable of storing energy independently of the other variables. By applying this theorem to the specific case of the piezoelectric actuator presented above, and by using its single-degree-of-freedom representation, which is valid for the specific device used in this chapter, it is possible to determine the thermal noise associated with the mechanical system [25]. The equation of motion of an SDOF system with a noise generator force representing the added mechanical noise can be used to calculate the thermal noise:

$$m\frac{\partial^2 x(t)}{\partial t^2} + d\frac{\partial x(t)}{\partial t} + kx(t) = f(t) = F_n \tag{2.23}$$

[25] shows that the mean square velocity developed by the noise generator F_n is expressed:

$$\frac{\overline{\partial x_n}^2}{\partial t} = \frac{\overline{F_n^2}}{d^2 + (\omega m - k/\omega)^2} \tag{2.24}$$

With noise velocity $\frac{\partial x_n(t)}{\partial t}$. By the equipartition theorem of thermodynamics, the kinetic energy stored in the system is:

$$E_k = \int_0^\infty \frac{1}{2}m\frac{\overline{\partial x_n}^2}{\partial t}\, df = \frac{1}{2}k_B T \tag{2.25}$$

This gives the expression noise force generator:

$$\overline{F_n^2} = 4k_B T d \tag{2.26}$$

This mechanical noise source will be translated into the electrical. The resistor from RLC mechanical branch of the BVD model was employed by Van Dyke to model the mechanical losses [74]. The mechanical noise source in the model used thus corresponds to the following:

$$\overline{v_n^2} = 4k_B T R_m \tag{2.27}$$

2.3 Experimental methodology

The experiments and measurements in this work were all carried out in the WELCOME laboratories at UCLouvain. This section describes the setup used during these experiments and some of the specific procedures put in place to ensure that they ran properly.

2.3.1 Setup

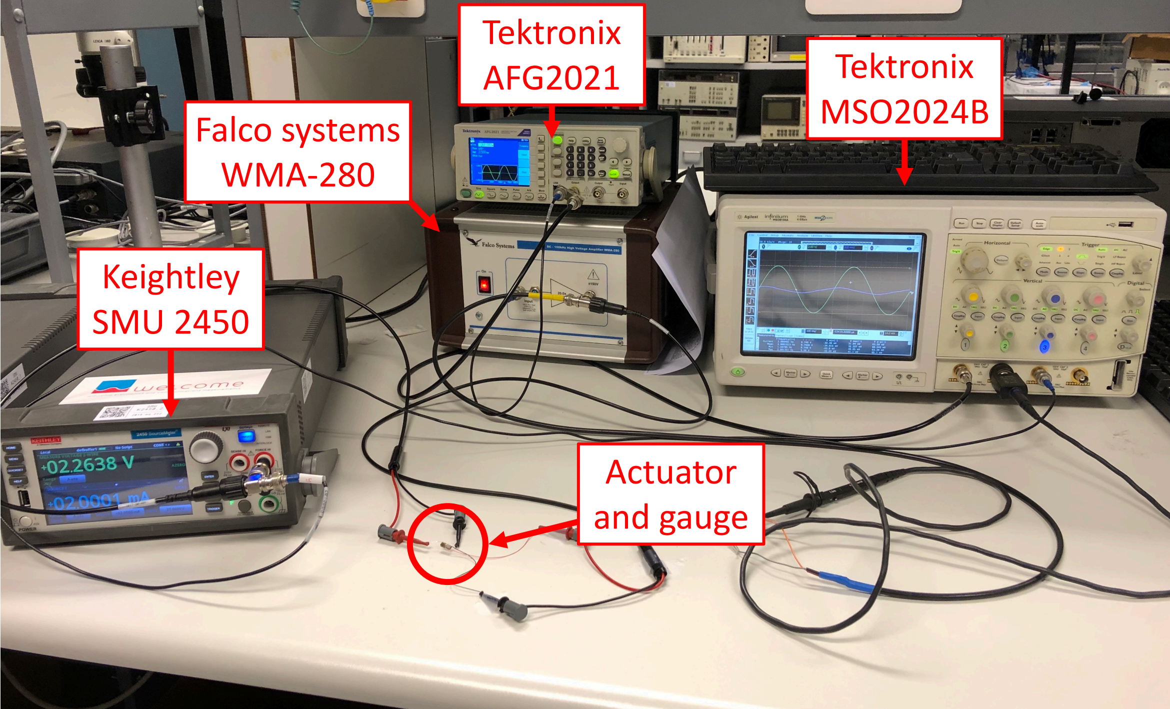

Figure 2.6: Setup for dynamic characterization of the silicon gauge strain sensor.

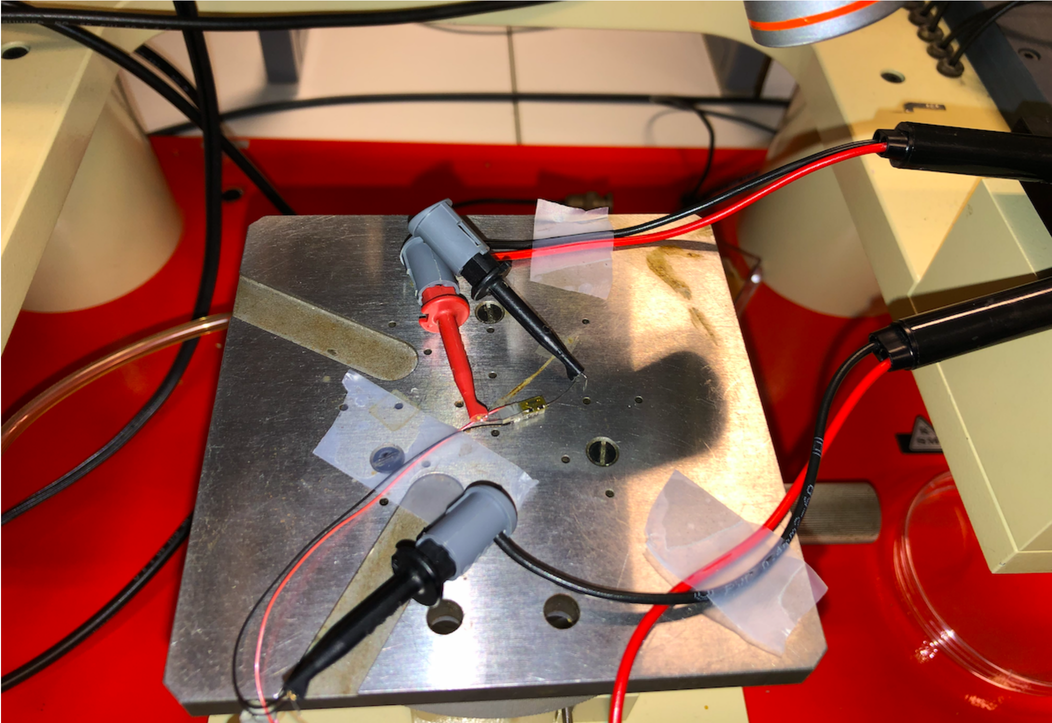

Figure 2.7: Silicon gauge on actuator setup.

The complete setup needed to characterize and study the silicon gauge under dynamic strain is shown in Figures 2.6 and 2.7. This setup required four devices:

- Tektronix AFG2021: Arbitrary Function Generator used to supply the actuator. Only sinusoidal signals were generated. It has an amplitude range up to 10V and can generate sinusoidal waves between 1μHz and 20MHz with an output impedance of 50Ω.
- Falco Systems WMA-280 amplifier: This amplifier is used to extend the voltage range of the generator up to 20 times and therefore the strain range applied to the silicon gauge. This allows us to reach the piezoelectric actuator limit and to highly reduce the output impedance of the generator to 0.1Ω. However, the amplifier has a bandwidth of 100kHz.
- Keightley SMU 2450: Source Meter Unit used to accurately inject current into the gauge.
- Tektronix MSO2024B: Oscilloscope used to measure the output of the generator, the amplifier and the voltage variation of the silicon gauge.

Figure 2.8 shows the setup and its connections.

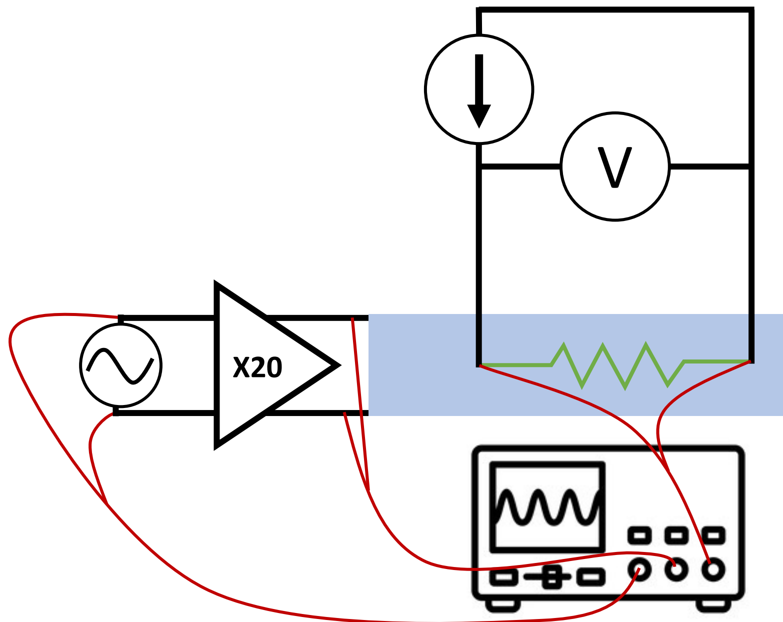

Figure 2.8: Scheme of the connections for the silicon gauge experimental setup.

2.3.2 Semiconductor strain gauge

The semiconductor strain gauge used in this work is a silicon gauge produced by BCM sensor [75]. The exact model is the *BPY_1000_2.6_U_I_RL*, its main parameters are listed in Table 2.2 and its layout represented in Figure 2.9.

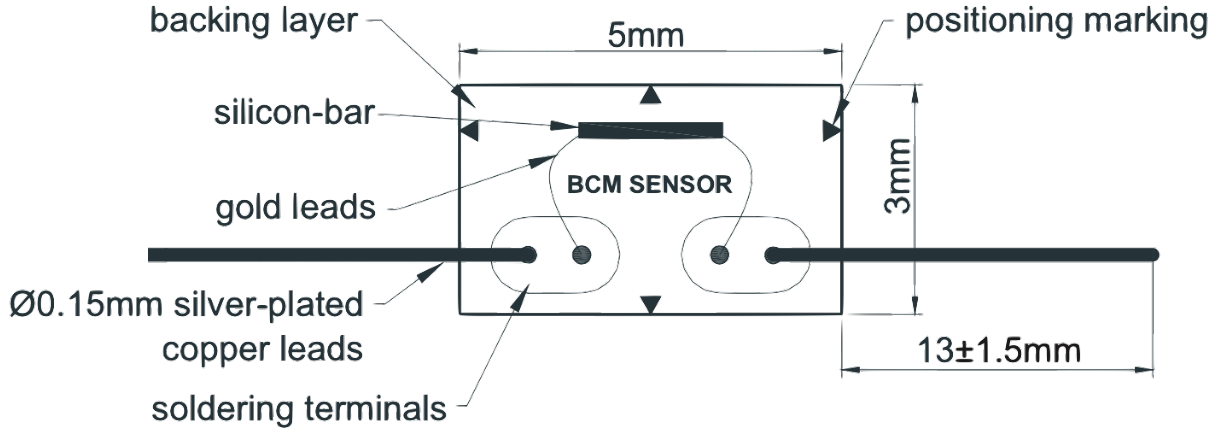

Figure 2.9: Dimensions of B-series of gauge length of 2.6mm from BMC sensor [39].

Parameters	Specifications
Nominal resistance	1[kΩ]± 2%
Gauge factor	150± 10%
Doping type	P-doped
Gauge length	2.6[mm]

Table 2.2: Main parameters of the *BPY_1000_2.6_U_I_RL* gauge from BMC [39].

This strain gauge has a dynamic tensile strain limit of $5000\mu\varepsilon$ which is well above the limits of the piezoelectric actuator used to generate its strains. At the orders of magnitude of strain to which the gauge will be subjected in this work, the datasheet [39] ensures good linearity and the gauge factor is correct for the desired range of measurements.

The longitudinal and transverse piezoresistive coefficients used at the beginning of the chapter in equation 2.9 corresponded to the [110] direction but the BCM sensor gauges are oriented in the [111] direction of the crystallographic axes. The new coefficients for the BMC sensor *BPY_1000_2.6_U_I_RL* gauge extracted from [76] correspond to:

$$\pi_l = \frac{\pi_{11} + \pi_{12} + \pi_{44}}{2} \qquad \pi_t = \frac{\pi_{11} + 5\pi_{12} - \pi_{44}}{6} \tag{2.28}$$

Table 2.3 shows the piezoresistive coefficients for all crystallographic main directions of lightly doped silicon [25]:

	n-type			p-type		
	[100]	[110]	[111]	[100]	[110]	[111]
π_l $[10^{-11}\text{Pa}^{-1}]$	-102.2	-31.2	-7.5	6.6	71.8	93.5
π_t $[10^{-11}\text{Pa}^{-1}]$	53.4	-17.6	6.1	-1.1	-66.3	44.6

Table 2.3: Longitudinal and transverse piezoresistive coefficients of silicon in different crystallographic directions from [25].

Using the expression for the gauge factor for semiconductor materials 1.24 and the equation which relates the deformation to the piezoresistive coefficients 1.25, we obtain the following expression:

$$K \approx E(\pi_l + \pi_t) \tag{2.29}$$

The longitudinal component of the gauge is aligned along the crystallographic axis [111]. Neglecting deformations in the transverse direction, taking Young's modulus $E = 188\text{GPa}$ [77] and $\pi_l = 93.5 \times 10^{-11}\text{Pa}^{-1}$ in the [111] direction, the theoretical gauge factor is:

$$K \approx 175.78 \tag{2.30}$$

2.3.3 Piezoelectric actuator

Physik Instrumente Ceramic is a manufacturer of piezo systems and developed the piezoelectric actuators used during this work. Two different models were used: *P-882.11* and *P-882.51* from the PICMA Stack Multilayer Piezo Actuators product family. A photo and a technical drawing of the actuators are shown in Figure 2.10 and the main parameters of the first model in Table 2.4.

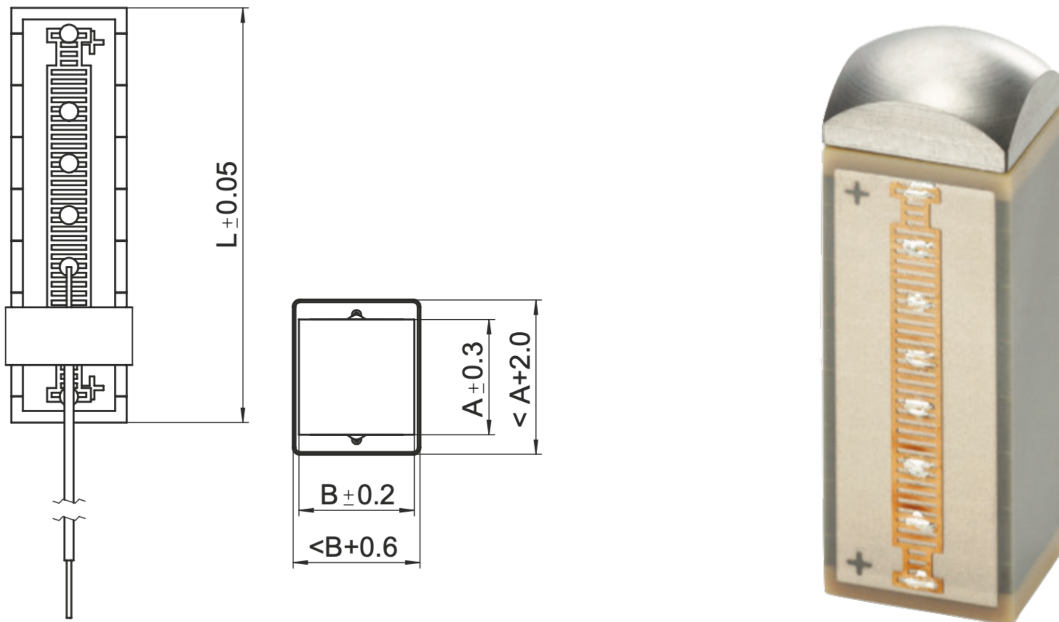

Figure 2.10: Technical draws and picture of the actuators from [65].

Model	Dimensions AxBxL [mm]	Nominal displacement [μm]	Electrical capacitance [μF]	Resonant frequency [kHz]
P-882.11	3x2x9	6.5 ±20%	0.15 ±20%	135 ±20%

Table 2.4: Main parameters of the *P-882.11* actuator from Physik Instrumente [65].

In this chapter, only the *P-882.11* model was used for the analysis of dynamic deformations with the silicon gauge. The second model was used exclusively in the next chapter. It can be seen from the figure 2.10 that these stack actuators have their electrodes placed on opposite side surfaces and the datasheet [65] indicates that they move in the direction of their length L. According to [25], simplifications can be made to the constitutive equations 1.32 presented in the previous chapter:

$$\sigma_1 = E\varepsilon_1 - d_{31}E_3 \tag{2.31}$$

Considering direction 1 that of the length and therefore of the displacement of the actuator and direction 3 that of the electric field. In the case where the actuator is free to deform, the stress becomes zero $\sigma = 0$ and the expression 2.31 as a function of the strain becomes:

$$\varepsilon_1 = \frac{d_{31}}{E}E_3 = \frac{d_{31}}{EA}V \tag{2.32}$$

With the electric field expressed as $E_3 = \frac{V}{A}$ the voltage applied V across the two electrodes of area A. Substituting $\varepsilon = \frac{\Delta L}{L}$, the change in length of the actuator is:

$$\Delta L = \frac{d_{31}L}{EA}V \tag{2.33}$$

The parameters of the BVD model can be determined experimentally on the basis of the impedance of the piezoelectric actuator [78, 79]. Based on the parameters in the table 2.4, the resonance frequency indicated by the manufacturer can be used to establish an initial equation that links the capacitance and inductance of the mechanical branch of the model.:

$$f_r = \frac{1}{2\pi\sqrt{L_m C_m}} \tag{2.34}$$

In accordance with the typical literature values [78, 80, 81, 82], a value was assigned to one of the two unknowns in equation 2.34, resulting in the parameter values of $L_m =$ 0.02mH and C_m = 69nF. As this has no impact on the resonant frequency, the resistance of the mechanical branch was set to R_m=1Ω, which is also consistent with the literature. As the electrical capacitance is also given by the manufacturer, $C_{elec} = 0.15\mu$F, the four final parameters of the BVD model for this particular actuator model are established.

2.4 Measurements and results

2.4.1 Extraction methodology

In order to conduct a dynamic analysis, it is necessary to determine the frequency response of the system. This is achieved by measuring the electrical response of the gauge when the actuator is supplied with a specific voltage. Initially, the aim was to compute the measured strain based on the expression of the gauge factor, which is defined as:

$$\varepsilon_{out}(t) = \frac{\frac{\Delta V(t)}{V_0}}{K} \tag{2.35}$$

Where V_0 is the voltage in the gauge at rest for 5mA injected into the gauge (which is the value recommended by the datasheet [39]) by the source meter. K is the theoretical gauge factor of 150 provided by the datasheet and $\Delta V(t)$ is used to denote the variation of the voltage in the gauge with respect to its voltage at rest. The voltage in the gauge when it is subjected to deformation and a current is injected into it can be expressed as follows:

$$V_{gauge}(t) = V_0 + \Delta V(t) \tag{2.36}$$

The value of the V_0 component is obtained when the system is at rest, and the value of the $\Delta V(t)$ component is that which is measured in order to compute the frequency response of the gauge when it is subjected to dynamic strains. This deformation ε_{out} is compared to the strain generated by the actuator denoted by ε_{in}:

$$\varepsilon_{in}(t) = \frac{V_{in,actuator}(t)}{V_{max,actuator}} \varepsilon_{max,actuator} \tag{2.37}$$

With $\varepsilon_{max,actuator}$ the maximum strain and $V_{max,actuator}$ the maximum voltage range provided by the actuator datasheet [65], respectively 722.22$\mu\varepsilon$ and 100V. And $V_{in,actuator}(t)$ the voltage at the actuator input.

The frequency response of the system is computed as the ratio between the amplitude of the strain measured at the strain gauge and the amplitude of the strain generated at the input by the actuator across the entire frequency range.

$$H(f) = \frac{\varepsilon_{out}(f)}{\varepsilon_{in}(f)} \tag{2.38}$$

It should be noted, however, that the results presented here are dependent on a number of factors. These include uncertainties regarding the values presented in the datasheets, the impact of the glue on the amplitude of the gauge response, and the potential non-linear deformation of the actuator. This work focuses exclusively on the frequency response of the silicon gauge when subjected to dynamic deformations. It is recommended that these topics be addressed in the continuity of this work.

An automated code was compiled directly via a computer connected to the equipment in order to control the signal delivered by the generator and to manage the signals acquired. This enabled the raw data to be extracted and post-processed. Three nodes were measured:

- Wave generator output
- Amplifier output
- Voltage variations across the silicon gauge

The Figure 2.12 shows the flow diagram of the measurement procedure. Figure 2.11 shows an example of the raw data recorded using the equipment mentioned in the explanation of the setup and the automated code.

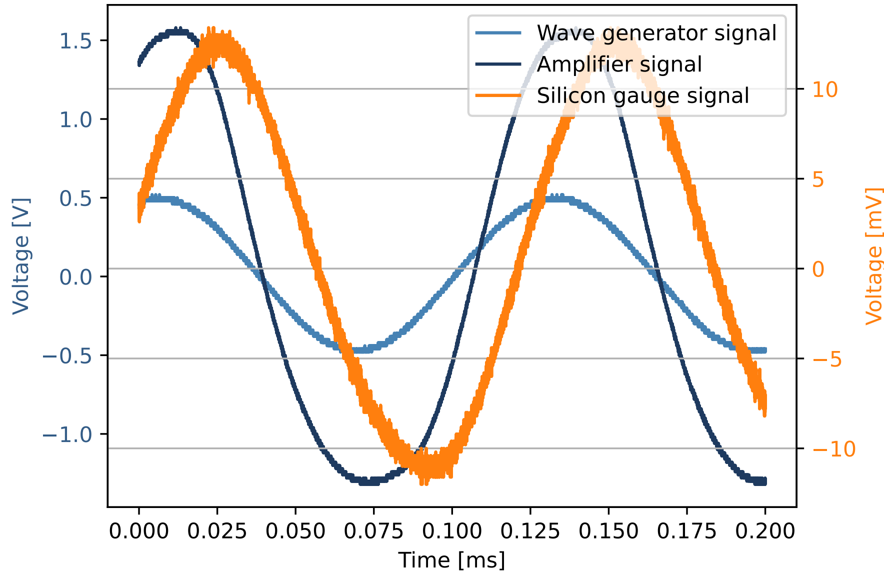

Figure 2.11: Measurement example composed of the generator output in blue and the amplifier output in dark blue with the values displayed on the left y-axis. And the output voltage of the gauge in orange displayed on the right y-axis.

In the example of the signals measured in Figure 2.11, the instruction sent to the sine wave generator was a signal of 0.5V amplitude and 7.9kHz. The output of the amplifier, which used as the input to the piezoelectric actuator indicated by the variable $V_{in,actuator}(t)$, multiplied the output of the sine wave generator by a factor of 20. A x10 probe has been used to ensure that the amplitude of the signal at the output of the amplifier does not exceed the measurable limit of the oscilloscope in case of electronic resonance. The measured signal is therefore divided by a factor of 10 compared with its real value. The signal expected to be measured at the output is 10V in amplitude. Figure 2.19 illustrates the inductive effect observed at this frequency in the setup employed, which generates a 5V overshoot in the voltage. Finally, the orange curve represents the variation voltage $\Delta V(t)$ measured at the strain gauge.

The raw data can be employed to obtain further information, including details on the phase shift between the measured signal from the gauge and the signals at the output of the wave generator and amplifier, the evolution of noise in different measurements as a function of frequency, and the frequency response of the sensor analysed over the full range. The results are presented and discussed in the final section of this chapter.

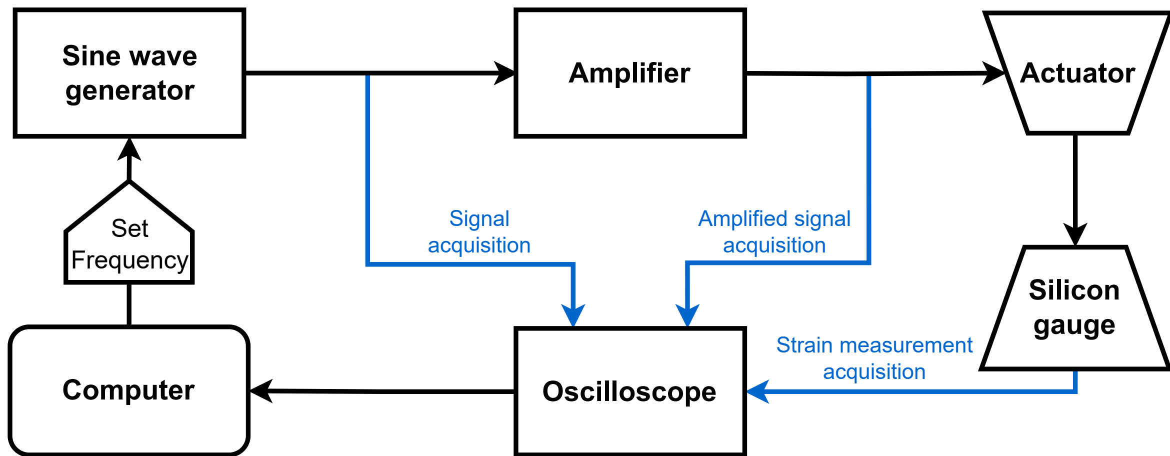

Figure 2.12: Flow diagram of the data extraction methodology.

2.4.2 Experimental model

The mechanical and electrical operation of a piezoelectric actuator has been presented in section 2.2 of this chapter. An electrical model based on both mechanical analogies and electrical equations was presented and simplified to a Butterworth Van Dyke topology. The circuit supplying the actuator can be integrated with the BVD dipole to obtain the circuit shown in Figure 2.13, which will define the overall setup behaviour in both electrical and mechanical terms.

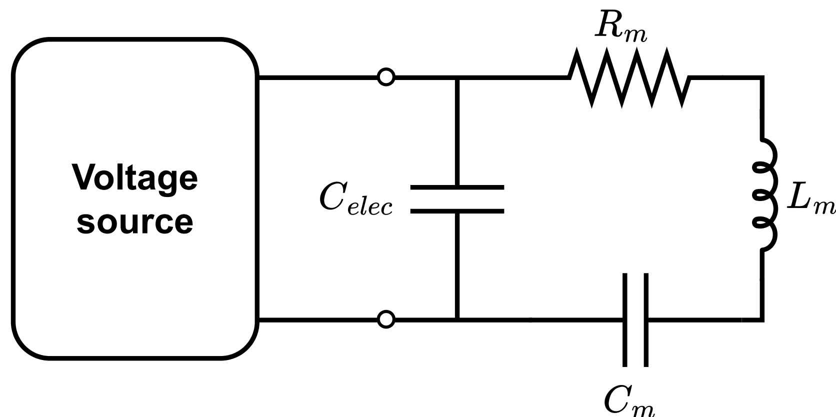

Figure 2.13: Equivalent Circuit of the actuator setup.

The results presented in this section are based on two different experimental setups. The initial configuration does not involve the utilisation of the amplifier. The output of the wave generator is connected directly to the input of the piezoelectric actuator. The second setup is identical to the simplified scheme in Figure 2.8. In this case, the voltage source is the output of the amplifier.

The piezoelectric actuator parameters C_{elec}, R_m, L_m and C_m have already been developed in section 2.2 and computed in section 2.3.3. For ease of use, these parameters are listed in the table 2.5.

Components	C_{elec}	R_m	L_m	C_m
Value	0.15[μF]	1[Ω]	0.02[mH]	69[nF]

Table 2.5: Parameters of the Butterworth Van Dyke model of the *P-882.11* piezoelectric actuator from Physik Instrumente..

Considering the output voltage as the input of the actuator $V_{in,actuator}$ and the input as the voltage source V_{in}, the transfer function of the experimental equivalent circuit model of figure 2.13 can be computed in three steps. The impedance of the RLC branch is expressed as:

$$Z_m = R_m + j\omega(L_m - \frac{1}{C_m}) \tag{2.39}$$

Taking into account the capacitance C_{elec} in parallel, the equivalent impedance of the actuator is:

$$Z_{actuator} = \left(\frac{1}{Z_m} + j\omega C_{elec}\right)^{-1} \tag{2.40}$$

The voltage $V_{in,actuator}$ corresponds to the voltage at the terminals of this voltage divider:

$$V_{in,actuator} = V_{in}\frac{Z_{actuator}}{R_{out} + Z_{actuator}} = V_{in}\frac{\left(\frac{1}{Z_m} + j\omega C_{elec}\right)^{-1}}{R_{out} + \left(\frac{1}{Z_m} + j\omega C_{elec}\right)^{-1}} \tag{2.41}$$

where R_{out} is the output impedance of the voltage source. The frequency response of the equivalent circuit will depend on the resonance of the RLC circuit linked to the mechanical branch of the piezoelectric actuator. The datasheet 2.4 indicates a resonant frequency of 135kHz$\pm$ 20% and using the parameters determined for the equivalent BVD model of the actuator, the resonance frequency of this RLC circuit is given by:

$$f_r = \frac{1}{2\pi\sqrt{L_m C_m}} = 135.481\text{kHz} \tag{2.42}$$

The frequency response will also depend on the equivalent circuit of the voltage source. The two different setups are presented individually below.

First setup without the amplifier

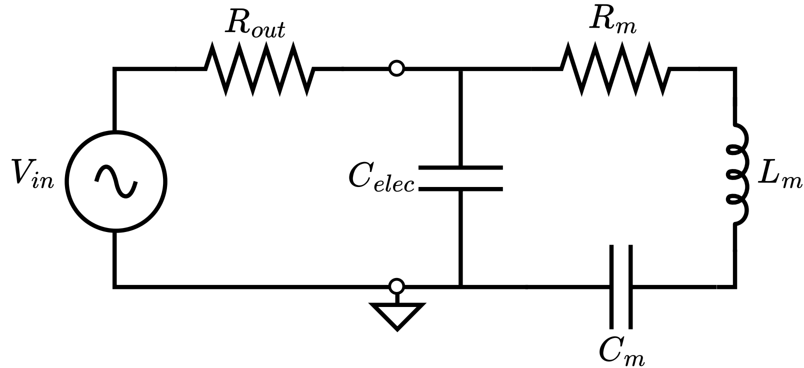

Figure 2.14: Equivalent circuit of the actuator setup without the amplifier used.

The RC circuit formed by R_{out} and C_{elec} will act as a low-pass filter and will operate at a different frequency from the RLC circuit. The arbitrary function generator has an output impedance $R_{out} = 50\Omega$, the electrical capacitance of the piezoelectric actuator is $C_{elec} = 0.15\mu\text{F}$ which gives an electrical cut-off frequency:

$$f_{cut_off} = \frac{1}{2\pi R_{out} C_{elec}} = 21.22\text{kHz} \tag{2.43}$$

The Bode diagram of this equivalent circuit for this setup is shown in Figure 2.16 is represented using LTspice. The frequency response of this configuration is therefore composed of a low-pass filter with a cut-off frequency at a lower frequency, followed by a resonance at approximately 135 kHz. In the region above the cut-off frequency, the results obtained in practice become increasingly random, due to the very small size of the signals.

Second setup with the amplifier

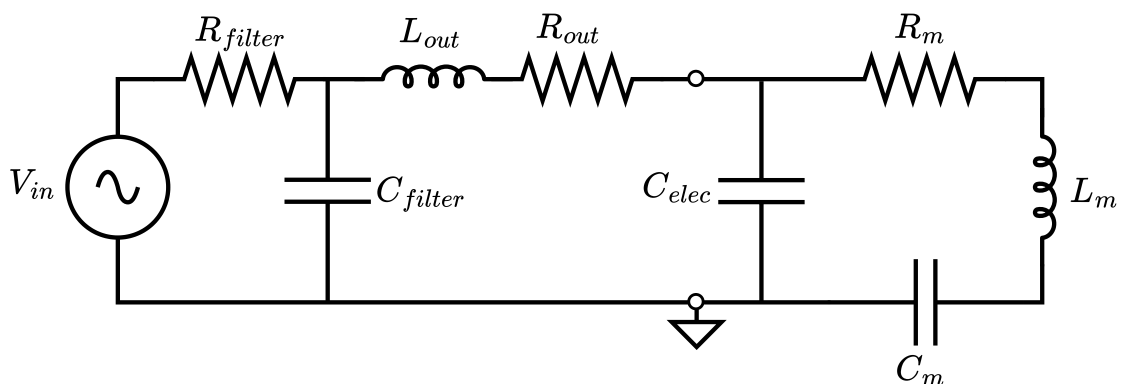

Figure 2.15: Equivalent Circuit of the actuator setup with the amplifier.

First of all, in this model, the resistor R_{filter} and the capacitor C_{filter} were added in order to simulate the 100kHz bandwidth of the amplifier. Experimental tests revealed

an electronic resonance at around 12kHz following the introduction of the amplifier into the setup. The very low output resistance $R_{out} = 0.1\Omega$ allows the cut-off frequency of the R_{out}-C_{elec} part to be shifted to $f_{cut_off} = 10.6$MHz and is therefore not even perceived in future results.

The underdamped electronic resonance peak, with a slope of -40dB/dec which follows the pole can be observed in Figure 2.16. The resonance caused by the actuator at approximately 135kHz is still present, but its amplitude is significantly weaker than that of the first setup.

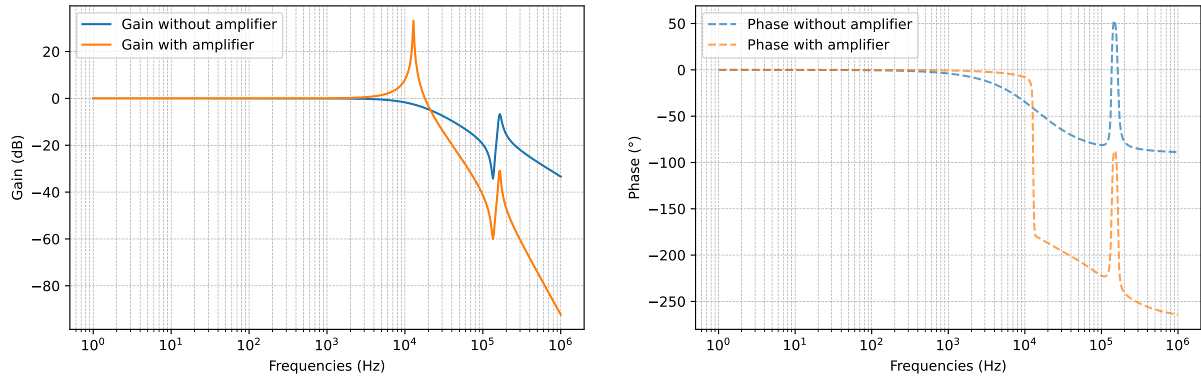

Figure 2.16: Gain Bode diagrams on the left and phase Bode diagrams on the right for the two setup presented.

Setup considerations

Now that the experimental model has been defined, a number of considerations need to be made specifically for the analysis of the silicon gauge under dynamic deformation.

It is first necessary to recall the objectives of this chapter. The main objective is to establish a valid experimental setup for the dynamic analysis of the silicon gauge, which will be reused for the CMOS sensor studied in the next chapter. The following section will present models developed to characterize the frequency response of the silicon gauge under dynamic deformations caused by the piezoelectric actuator. Figure 2.17 illustrates the block diagram of the system analysed in this chapter.

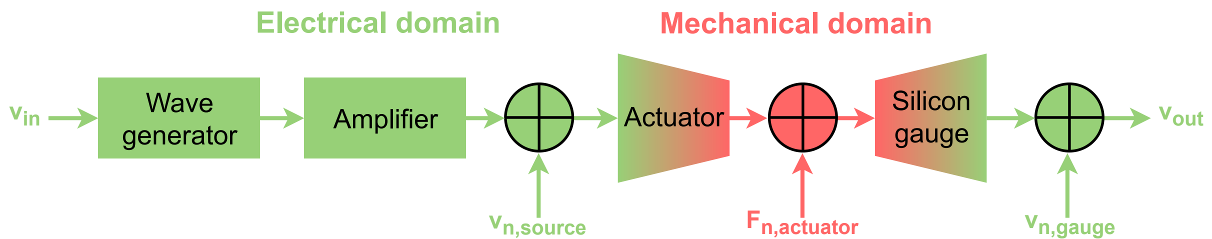

Figure 2.17: System block diagram.

It can be assumed that the silicon gauge has a constant bandwidth throughout the frequency range analysed, and therefore will not affect the frequency response of the system. However, it is possible that the response amplitude may be attenuated due to the influence of different noise sources, as previously discussed in this chapter. The shape of the frequency response is influenced exclusively by the voltage supply and the piezoelectric actuator.

The BVD model is used to characterize the operation of the piezoelectric actuator. The aim of this equivalent model is to transcribe the mechanical behaviour of this device into the electrical domain. The models from Figures 2.14 and 2.15 also include the impact of the voltage supply on the rest of the circuit, including the amplifier bandwidth and the generator output resistance, for example and the electrical frequency response. This means that the simulated Bode diagrams for the equivalent circuits of these setups in Figure 2.16 already take into account the mechanical response of the actuator in addition to the electrical behaviour of the setup.

It is essential to distinguish between the mechanical and electrical frequency responses of the system. The Bode diagrams, which have been simulated above, take account of these two effects together. However, the electrical measurement made at the actuator input will obviously not take account of its mechanical behaviour, whereas the model does. The low-pass filter generates a cut-off frequency based on the R-C circuit with the output resistance of the voltage source and the electrical capacitance of the actuator. The mechanical behaviour of the actuator could alter this response, resulting in the generation of a shift on the frequency pole.

2.4.3 Results

This section summarises all the results of the dynamic analysis of the experimental models presented previously. First of all, two different models have been established according to two different set-ups, and the initial results enable them to be validated. An analysis of the frequency response will be carried out using the method described in section 2.4.1 and on the basis of their Bode diagrams. Experimental noise estimates are then analysed.

Amplifier impact on input voltage

The addition of the amplifier from the first setup 2.14 to the second setup 2.15 introduced a voltage overshoot at the input of the piezoelectric actuator only around 12kHz as shown in Figure 2.19. This overshoot is linked to the appearance of a resonance. Two possibilities have been considered:

- Either this resonance is caused by an inductive effect already present in the actuator with the setup without amplifier but has just been masked by its cut-off frequency of 21.22kHz.
- Or the amplifier has added an inductive effect, which in this case is perceptible because the cut-off frequency of this setup is set at 100kHz.

This hypothesis was verified using an extension to the second setup shown in Figure 2.18.

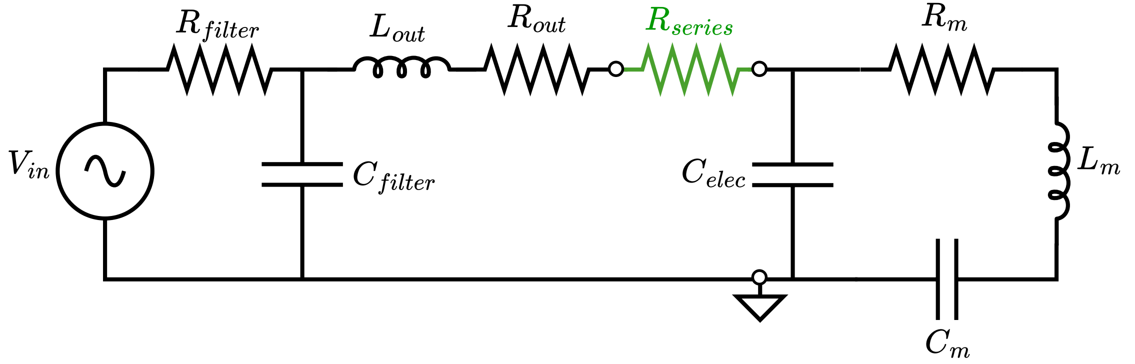

Figure 2.18: Equivalent circuit of the setup with amplifier and a series resistor connected to the amplifier output.

A series resistor with a value of $R_{series} = 47\Omega$ has been connected in series with the amplifier output. Assuming that electronic resonance has been induced by the piezoelectric actuator, placing this resistor reduces the cut-off frequency of the RC circuit formed by the amplifier's output resistor R_{out} and the actuator's electrical capacitance C_{elec}. If the first assumption mentioned above is correct, the voltage at the actuator input should be identical over the frequency band of 10kHz between the setup without amplifier and the setup in figure 2.18 since a pole has been added to the frequency in this second case:

$$f_{cut_off} = \frac{1}{2\pi(R_{out} + R_{series})C_{elec}} \approx 22.53\text{kHz} \tag{2.44}$$

Experimental measurements of the input voltage as a function of generator frequency for the three different cases (setup without amplifier, with amplifier, with amplifier and resistor in series) are shown in Figure 2.19.

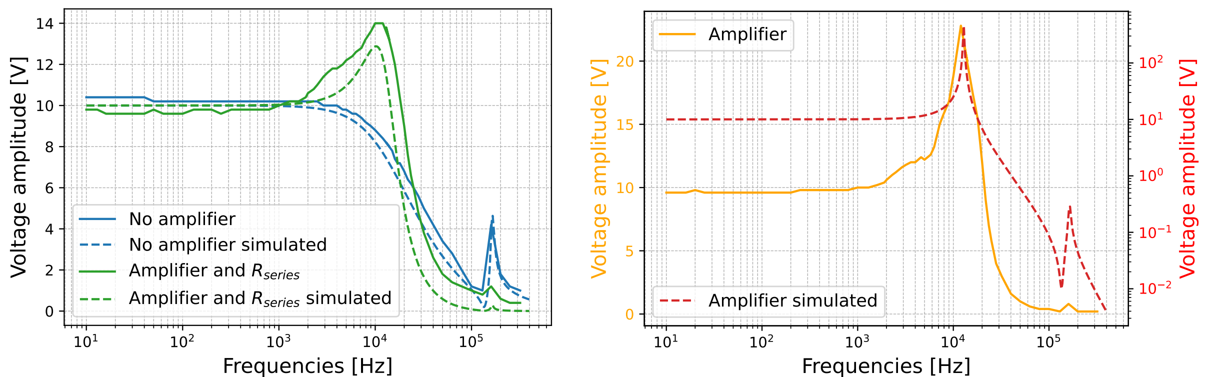

Figure 2.19

We can therefore see that the electrical resonance peak appears even if a pole of the same frequency has been deliberately added in the second setup in order to match that of the

first setup. The first hypothesis is invalidated and the second is confirmed. The amplifier's user manual mentioned a potential overshoot of the output voltage if a capacitive load is connected to its output. These initial results validate the addition of the L_{out} inductance in the second setup presented.

Frequency response analysis

Figure 2.21 shows the frequency response in amplitude for the two initial setups as well as the one in Figure 2.18. This work does not focus on their values for the reasons mentioned in the previous section, but rather on the shape of these curves. These frequency responses are functions of:

$$H(f) \propto \frac{\varepsilon_{out}(f)}{\varepsilon_{in}(f)} \tag{2.45}$$

With ε_{in} and ε_{out} defined in equations 2.37 and 2.35 respectively. These values were extracted by post-processing over the entire frequency range from 10Hz to 300kHz. The amplitude of the output voltage of the generator is fixed at 10V which gives the voltage amplitude at the actuator input in Figure 2.19.

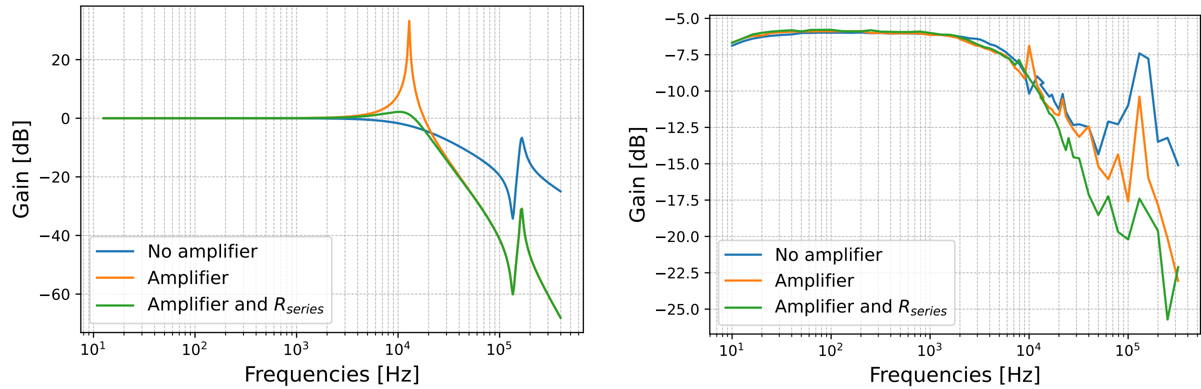

Figure 2.20: Frequency response of the system for three different configurations simulated on the left and measured on the right.

The nominal resistance of the silicon gauge is 1kΩ. Knowing the operating parameters of the actuator and the voltage at its input, the deformations it will theoretically undergo:

$$\varepsilon_{estimated} = \frac{V_{in}}{V_{max,actuator}} \varepsilon_{max,actuator} = \frac{10}{100} \cdot \frac{6.5 \times 10^{-6}}{9 \times 10^{-3}} = 72.22\mu\varepsilon \tag{2.46}$$

The gauge factor of the theoretical gauge is used to calculate the variation in theoretical resistivity of the gauge:

$$\Delta R = K \varepsilon_{estimated} R = 150 \cdot 72.22 \times 10^{-6} \cdot 1000 = 10.83\Omega \tag{2.47}$$

The source meter injects a current of $I_{inj} = 5$mA in order to measure this variation in resistivity in voltage for the oscilloscope. The voltage measured across the gauge is:

$$V_{gauge}(t) = R_{nom}I_{inj} + \Delta R(t)I_{inj} = 5 + 0.054\sin(\omega t) \tag{2.48}$$

The measured voltage thus corresponds to a direct current (DC) voltage dependent on the nominal resistance value of the silicon gauge, plus an alternating current (AC) component representing the variation in resistivity of the gauge at a much smaller amplitude. In order to analyse the lower amplitude frequency response, it was necessary to impose AC decoupling when probing the voltage across the gauge. This eliminated the DC component, allowing the AC component to be accurately measured. This is why the frequency range under consideration commences at 10Hz. The AC component was influenced by AC decoupling when the generated signal was of low frequency. Figure 2.20 illustrates that the amplitude value diminishes as the frequency approaches 10Hz, which can be attributed to the aforementioned AC decoupling of the measurement.

The graph also illustrates a plateau where the frequency response is stable from several kHz in all three cases. Thereafter, the three slopes exhibit a decrease, and it can be observed that the two setups using the amplifier decrease more significantly than the one without the amplifier. This is a consequence of the electrical resonance effect introduced when the amplifier was added which causes a decrease of -40dB/dec from this frequency compared to a decrease of -20dB/dec for the first setup from its cut-off frequency.

Finally, the resonance peak of the piezoelectric actuator at 135kHz is identified in all three cases. Beyond that, the signals observed are of a low amplitude and the results become random.

Signals phase

Figure 2.21 illustrate the phase differences between the signal emitted by the generator and the signal measured by the gauge. This was completed efficiently through the utilisation of post-processing techniques. The Fourier transform of the measured signal at the output of the gauge and the signal at the output of the generator or amplifier was calculated. The frequency at which the amplitude of the transforms is at its maximum was then extracted. The phase of the signal associated with this frequency for each of the two signals is compared across the entire frequency range over which measurements were taken. Figures 2.21 illustrate the Bode phase plot for the two setups presented in section 2.4.2.

The illustration on the left depicts the phase shift of a low-pass filter with a cut-off frequency of approximately 15kHz. As previously stated, the mechanical parameters of the BVD model may potentially influence the position of this pole in the frequency response of the overall system. In practice, the actuator datasheet provides an uncertainty of 20% on the value of the electrical capacitance. This uncertainty could theoretically reduce the pole to the value:

$$f_{cut_off_uncertainty} = \frac{1}{2\pi R_{out}(0.15 \times 1.2)10^{-6}} = 17.88\text{kHz} \tag{2.49}$$

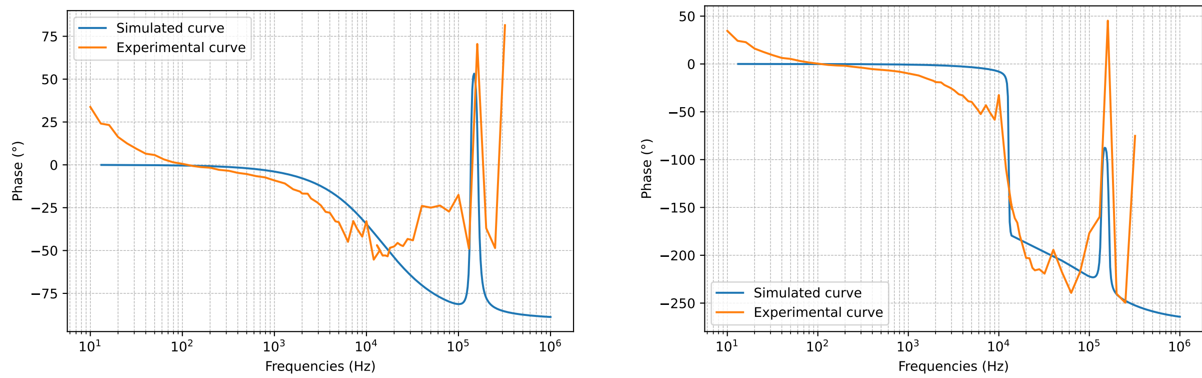

Figure 2.21: The Bode phase plot of the setup for the case where the amplifier is not included on the left, and for the case where the amplifier is included on the right.

As illustrated in the figure on the right, the resonance introduced by the amplifier is once again evident. The abrupt 180° phase shift at approximately 12 kHz is indicative of resonance in an underdamped RLC circuit. In the context of a series RLC circuit, the damping factor is defined as:

$$\zeta = \frac{R}{2}\sqrt{\frac{C}{L}} \tag{2.50}$$

In the case of the right figure, $R = R_{out} = 0.1\Omega$. Figure 2.22 depicts the Bode phase diagram for the identical configuration with the inclusion of a series resistor $R_{series} = 47\Omega$ connected in series to the amplifier's output. The damping factor is multiplied by a factor of 500. As illustrated in Figure 2.19, the response remains underdamped, although the resonance peak is attenuated.

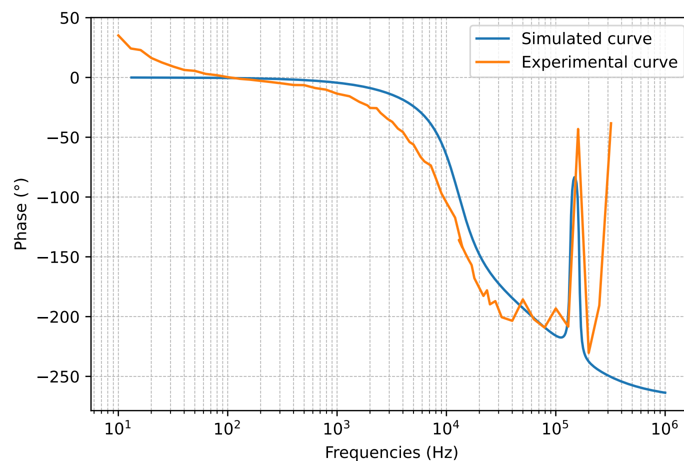

Figure 2.22: The Bode phase plot of the setup with the amplifier and the series resistor.

The three Bode phase plots demonstrate that the phase responses of the models established for the three setups coincide with the experimental results. This indicates that the

Butterworth Van Dyke model is an effective approach for simulating the mechanical and electrical operation of the piezoelectric actuator in terms of the phase of the signals.

Noise

This section provides a brief overview of the influence of noise on the measured signal. All the results presented so far have been computed on the basis of data that has been attenuated to a lower level of noise. An initial averaging was performed by the oscilloscope during the measurement process, and post-processing was employed to further attenuate any residual noise in the signal. In order to obtain the results included in this noise analysis, the averaging performed by the oscilloscope was removed, thus producing a raw version of the measured signal.

A curve fitting procedure was conducted on the signal measured at the output of the gauge with the objective of separating the useful signal from the noisy experimental signal. Curve fitting was performed using the curve_fit function from the SciPy API on Python. The curve_fit function uses non-linear least squares to fit a function to the input data. Once the useful signal has been extracted, it is subtracted from the measured signal in order to isolate the noise, as illustrated in Figure 2.23.

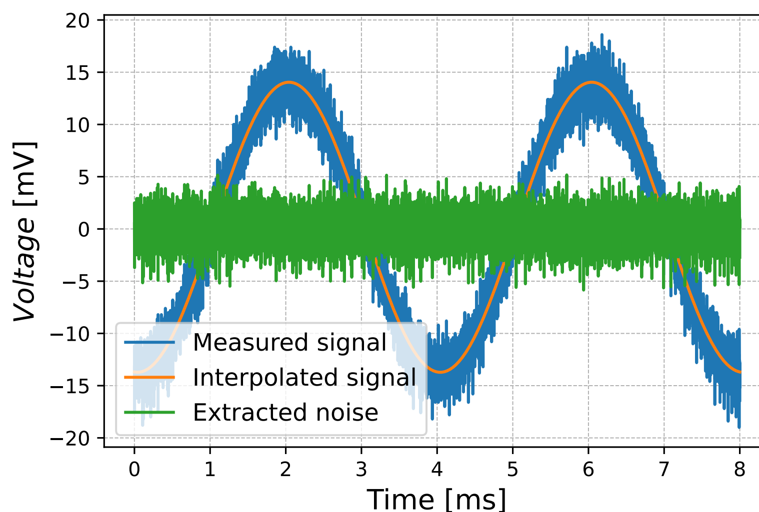

Figure 2.23: Silicon gauge measurement noise extraction.

Once the useful signal component and the noise component had been extracted separately, the signal-to-noise ratio (SNR) was computed according to the following formula:

$$SNR_{dB} = 10\log_{10}\left(\frac{P_{signal}}{P_{noise}}\right) \tag{2.51}$$

The power of the useful signal P_{signal} and the power of the noise signal P_{noise} are determined by:

$$P_{signal} = \frac{1}{N}\sum_{i=0}^{N-1} V_{signal}[i]^2 \qquad P_{noise} = \frac{1}{N}\sum_{i=0}^{N-1} V_{noise}[i]^2 \tag{2.52}$$

With N the number of samples of the measured signals. The computations were performed over the entire measured frequency range with the amplifier configuration. Figure 2.24 depicts the results for SNR and noise power.

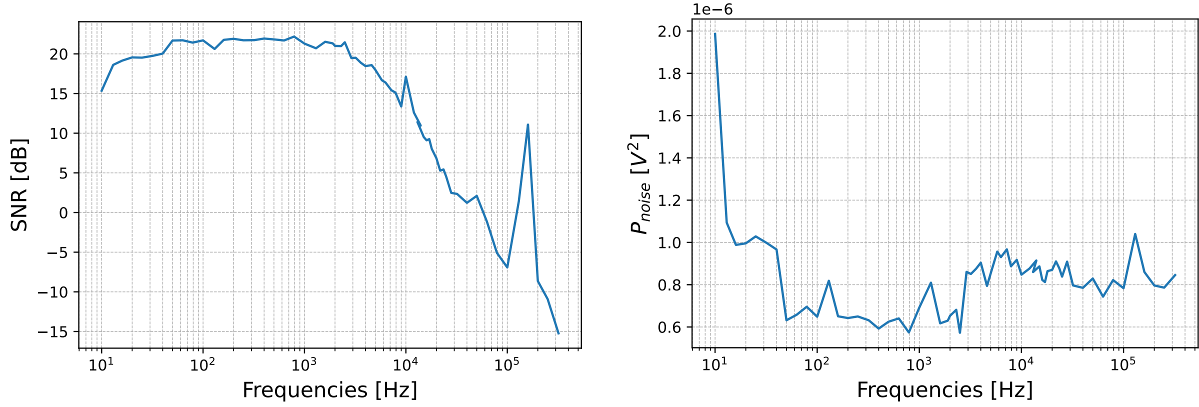

Figure 2.24: Signal-to-noise ratio on the left and experimentally estimated noise power on the right as a function of the frequency.

The signal-to-noise ratio demonstrates a slight increase at low frequencies before reaching a plateau. Then, there is a gradual decline from 3 kHz, accompanied by the reappearance of the resonance peak of the piezoelectric actuator at 135 kHz. The noise power is significant and declines precipitously at low frequencies, remaining at a stable value throughout the remainder of the bandwidth.

The SNR curve exhibits a typical pattern, with flicker noise initially decreasing and then dominating until the corner frequency, after which thermal noise from the voltage source and silicon gauge, and mechanical noise from the piezoelectric actuator, become the dominant sources.

2.4.4 Conclusion

The objective of this chapter was to develop and validate a theoretical model of the piezoelectric actuator and silicon strain gauge to predict their behavior in a dynamic regime. This goal was successfully achieved by modeling the actuator with a simplified Butterworth Van Dyke topology and integrating it with the experimental setup. The silicon strain gauge was then used to measure the system's frequency response, effectively validating the predicted model.

Two configurations were tested:

- The initial setup connected the signal generator directly to the actuator with an output resistance of 50Ω, forming a low-pass filter with a cutoff frequency of approximately 22 kHz due to the electrical capacitance of 0.15μF of the actuator.
- The second setup used an amplifier with an output resistance of 0.1Ω, which shifted the RC circuit's pole to a higher frequency well beyond the frequency range analysed, but also introduced unexpected inductive effects, reducing the effective bandwidth. To model this, an output inductance, represented by L_{out}, was added to the amplifier setup model.

Comparing the models and experimental results, the frequency response exhibited stability up to approximately 3-4 kHz, after which they were impacted and decreased for the reasons outlined above. There is a consistent phase alignment between the predicted and measured signals, demonstrating the robustness of the model used. Additionally, a noise analysis was conducted, providing estimates of the experimental noise.

This chapter successfully established a dynamic test bench for strain sensor characterization, focusing on the system's frequency response shape and phase. Future work could extend this study by comparing dynamic deformation amplitudes with known static performance. The techniques presented here were used to analyse the CMOS strain sensor in the next chapter.

Chapter 3

Characterization and dynamic strain analysis of the CMOS strain sensor

The objective of this chapter is to characterize a CMOS strain sensor and analyse its dynamic behaviour. The sensor, developed at the Université Catholique de Louvain, employs a self-bias current reference circuit inspired by the Widlar current source topology, resulting in the formation of a β-mutiplier reference circuit. Two distinct topologies are examined and detailed in [63, 64]. One employs a full transistor configuration, while the other substitutes a transistor with a polysilicon resistor. The sensor relies on the piezoresistive properties of silicon and a specific arrangement of transistors to make its current dependent to applied stress.

The aim is to analyze the sensor when subjected to dynamic vibrations and deformations. The CMOS strain sensor and its topologies are presented in the initial section, covering practical operation, equations, and non-idealities. The impact of temperature and dopant concentration on sensor sensitivity is investigated. Building on the model established in Chapter 2 for the dynamic analysis of the strain gauge, adjustments are made, and an adapted setup for the CMOS strain sensor is presented in the second part of this chapter. Additionally, the static setup used to characterize the sensor's behavior under temperature variations is described. The methodology for each of these analyses and the results are discussed in the final section.

3.1 Theoretical specifications of the CMOS strain sensor

The two implementations employed in this thesis are illustrated in Figure 3.1. This section introduces the sensor, which is presented in [63].

The sensor is made up of three parts:

- PMOS transistors M3 and M4, which impose the same current in both branches of

the circuit when no strain or stress is applied.

- Transistors M5 to M8 form a cascode to strongly reduce the sensor's dependence on the voltage supply. These transistors have no impact on the behaviour of the circuit when subjected to stress or strain.
- NMOS transistors M1 and M2 with the passive component R in one topology and replaced by an active load M9 in the other. This part of the circuit imposes a quadratic relationship in both branches.

Further implementations of this sensor aimed at improving sensitivity and reducing temperature dependence are included in [63]. A full detailed analysis of the operation, a noise study, discussions on the impact of different parameters, integration into test circuits and more are included in the thesis [64].

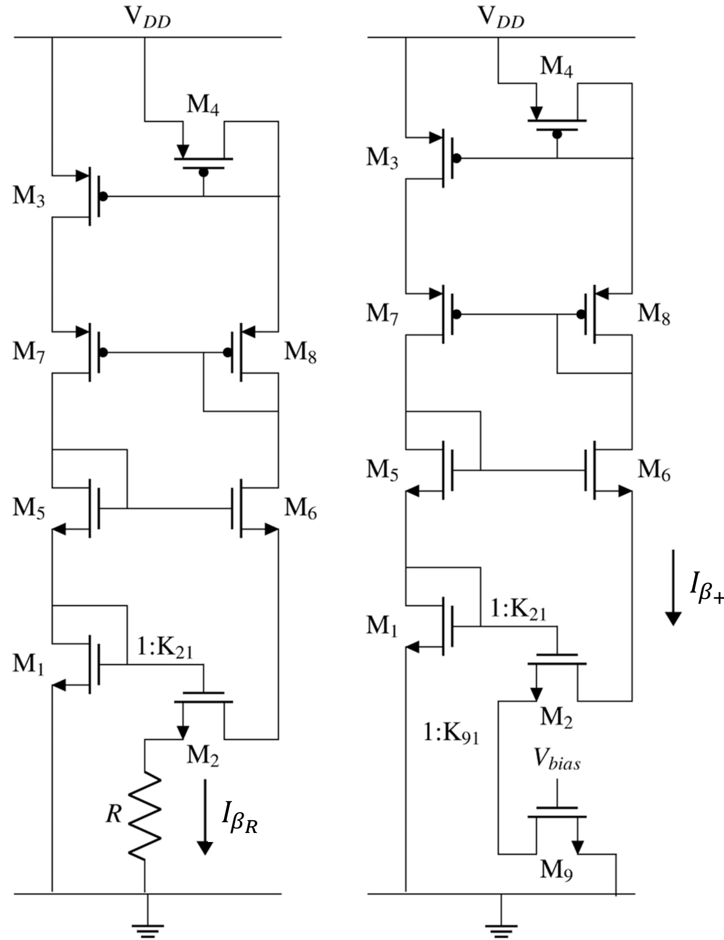

Figure 3.1: β-multiplier reference circuits. β_R topology with polysilicon resistor R on the left and full-transistor implementations β_+ topology on the right. The reference currents are, respectively, written I_{β_R} and I_{β_+} [63].

3.1.1 Impact of strain on transistor operation

Strain affects the resistivity of the semiconductor material. In the case of transistors, the carrier mobility is subject to variations. For infinitesimal displacements, these variations are defined by [63]:

$$-\frac{d\mu_i}{\mu_i} = \pi_{i,l}\sigma_l + \pi_{i,t}\sigma_t \tag{3.1}$$

where μ_i is the mobility for carriers "i" which is denoted "n" for electrons and "p" for holes. π_l and π_t are the longitudinal and transverse piezoresistive coefficients respectively and σ_l and σ_t are the longitudinal and transverse stress components respectively. By solving this equation gives the dependence of mobility on stress:

$$\mu_i = \mu_i^0\, e^{-(\pi_{i,l}\sigma_l + \pi_{i,t}\sigma_t)} \tag{3.2}$$

With μ_i^0 is the mobility in the relaxed case. The expression for the drain-source current in an NMOS transistor taking into account the piezoresistive effects on mobility and Early effect becomes:

$$I_{DS}(\sigma) = \mu_n(\sigma)\, C_{ox}\, \frac{W}{L}\, \frac{(V_{GS} - V^{th})^2}{2}\, (1 + \frac{V_{DS}}{V_{EA}}) \tag{3.3}$$

where C_{ox} refers to the oxide capacitance, $\frac{W}{L}$ the ratio of width to length of the transistor, V_{GS} the gate-source voltage, V^{th} the threshold voltage, V_{DS} the drain-source voltage and V_{EA} the Early voltage. To simplify developments, the transconductance factor [63] is introduced and defined as:

$$\beta_i(\sigma) = \mu_i(\sigma)\, C_{ox}\, \frac{W}{L} \tag{3.4}$$

In the rest of this work, uniaxial stress and strain is considered. The operation of the piezoelectric actuator used in the setup described in section 2.3.3 validates this assumption about its displacement. The value of the piezoresistive coefficients in silicon depends on their direction as shown in the table 2.1. By orienting the channel of the sensitive transistors of one branch in the longitudinal direction of the strain and those of the other branch in the perpendicular direction, the sensor's sensitivity to deformation can be enhanced, thereby increasing its gauge factor [64]. The subsequent equations will provide further evidence to support this assertion. In the following sections, the numbered subscripts are used to correspond to the related transistor.

3.1.2 Current equations for β_R topology

In absence of strain

If PMOS transistors M3 and M4 have identical dimensions, operate in saturation, and neglecting the Early effect and threshold voltage mismatch, then in the absence of stress, their currents are equivalent:

$$\mu_{p,3}^0 = \mu_{p,4}^0 \tag{3.5}$$

$$I_{DS,3}(\sigma = 0) = I_{DS,4}(\sigma = 0) \tag{3.6}$$

This system of equations can be established for both topologies:

$$\begin{cases} V_{SG,3} = V_{SG,4} \\ I_{DS,3} = I_{DS,4} \\ I_{DS,1} = I_{DS,3} \\ I_{DS,2} = I_{DS,4} \end{cases} \tag{3.7}$$

A Kirchoff's law can be applied to establish these expressions for the NMOS transistors M1 and M2 and the resistor R:

$$V_{GS,1} = R\, I_{DS,2} + V_{GS,2} \tag{3.8}$$

If transistors M1 and M2 are in saturation and the Early effect is neglected, their gate-source voltage is expressed as:

$$V_{GS,j} = V_j^{th} + \sqrt{\frac{2I_{DS,j}}{\beta_{n,j}}} \tag{3.9}$$

The letter "j" is used to indicate a specific transistor. The transconductance factor also depends on the ratio K_{21} between the dimensions of transistors M1 and M2:

$$\left(\frac{W}{L}\right)_1 = K_{21}\left(\frac{W}{L}\right)_2 \longrightarrow \beta_{n,1} = K_{21}\beta_{n,2} \tag{3.10}$$

Neglecting the threshold voltage mismatch between the transistors, the two expressions above can be injected into 3.8 to obtain:

$$\sqrt{\frac{2I_{DS,2}}{K_{21}\beta_{n,2}}} = R\, I_{DS,2} + \sqrt{\frac{2I_{DS,2}}{\beta_{n,2}}} \tag{3.11}$$

After development and simplification, the current in the branches is defined by the following quadratic relationship:

$$I_{DS,2}(\sigma = 0) = I_{\beta_R}(\sigma = 0) = 2\,\frac{(1 - 1\sqrt{K_{21}})^2}{\beta_{n,2}R^2} \tag{3.12}$$

With strain applied

By taking strain into account, the second expression of the system of equations 3.7 must be modified because the mobility of transistors M3 and M4 is no longer equal:

$$I_{DS,3} = I_{DS,4}\frac{\beta_{p,3}(\sigma)}{\beta_{p,4}(\sigma)} \tag{3.13}$$

The transconductance factors have been revised and now differ between M3 and M4. This is due to the fact that the transistors are oriented differently and the stress applied is assumed to be uniaxial. [63] provides the developments and the expression of the branch current of the β_R-multiplier topology 3.11 becomes in the presence of strain:

$$I_{\beta_R}(\sigma) = 2\frac{(e^{(\pi_3-\pi_1-\pi_4)\frac{\sigma}{2}} - e^{-\pi_2\frac{\sigma}{2}}/\sqrt{K_{21}})^2 e^{2\pi_r\sigma}}{R^2\beta_n^0} \tag{3.14}$$

3.1.3 Current equations for β_+ topology

An improvement on the above topology is its equivalent with an NMOS transistor in triode, which replaces the resistor shown in figure 3.1. The current in the branches can therefore be tuned using the gate voltage of this transistor [64]. Kirchoff's law is applied to obtain the relationship between the voltages of transistors M1, M2 and M9.:

$$V_{GS,1} = V_{GS,2} + V_{DS,9} \tag{3.15}$$

After development [63], the current in the branch of the β_+-topology without or with the presence of deformation is:

$$\text{No stress applied: } I_{\beta+}(\sigma = 0) = 2V_{ov}^2\beta_n^0\frac{(1-1/\sqrt{K_{21}})^2}{\Big[(1-1/\sqrt{K_{21}})^2 + 1/K_{91}\Big]^2} \tag{3.16}$$

(3.17)

$$\text{Stress applied: } I_{\beta+}(\sigma) = 2V_{ov}^2\beta_n^0\frac{(e^{(\pi_3-\pi_1-\pi_4)\frac{\sigma}{2}} - e^{\pi_2\frac{\sigma}{2}}/\sqrt{K_{21}})^2}{\Big[(e^{(\pi_3-\pi_1-\pi_4)\frac{\sigma}{2}} - e^{\pi_2\frac{\sigma}{2}}/\sqrt{K_{21}})^2 + e^{\pi_9\sigma}/K_{91}\Big]^2} \tag{3.18}$$

The value of K_{91} corresponds to the ratio between the dimensions of transistors M9 and M1. The overdrive voltage is defined as $V_{ov} = V_{bias} - V^{th}$, where the terms V_{bias} and V^{th} correspond to the gate voltage of transistor M9 and its threshold voltage, respectively.

3.1.4 Temperature and dopant dependencies in CMOS strain sensor

The current equations presented above do not take into account certain non-idealities. The expressions 3.14 and 3.18 for the currents in each topology are revised. The effects of doping and temperature on the various parameters are taken into account. The validity of these new expressions are then assessed experimentally.

Temperature and dopant dependencies of piezoresistive coefficients

The piezoresistive coefficients are subject to variation as a function of temperature T and doping N, as expressed by [83]:

$$\pi(N,T) = \pi(N_0, 300\text{K})\ P(N,T) \tag{3.19}$$

In this expression, the reference piezoresistive coefficient for a low doping level N_0, and a reference temperature of 300K is represented by $\pi(N_0, 300\text{K})$. The function $P(N,T)$ represents a correction factor that takes into account the variations linked to the doping level and the temperature. It is expressed by [84] as follows:

$$P(N,T) = \frac{300}{T} \frac{1}{\left(1 + e^{-\frac{E_f}{k_b T}}\right) \ln\left(1 + e^{-\frac{E_f}{k_b T}}\right)} \tag{3.20}$$

where k_b is the Boltzmann constant and E_f is the Fermi level, which depends on doping of the material:

$$\text{N-doped silicon: } E_f = E_c + k_B T \ln\left(\frac{n}{N_c(T)}\right) \tag{3.21}$$

$$\text{P-doped silicon: } E_f = E_v - k_B T \ln\left(\frac{p}{N_v(T)}\right) \tag{3.22}$$

E_c and E_v represent the energy of the conduction and valence bands respectively. The conduction and valence density of states are $N_c(T) = N_{c,T_0} T^{3/2}$ and $N_v(T) = N_{v,T_0} T^{3/2}$, where the subscript T_0 represents these values at a reference temperature. This work will focus on measurements between 300K and 355K. The concentration of carriers in a semiconductor is known to vary with temperature, and can be divided into three distinct regions [85] as shown in Figure 3.2:

- Freeze out temperature region: the thermal energy is very low. It gradually becomes sufficient to ionise the dopant atoms as the temperature rises and the number of carriers is increasing.
- Extrinsic temperature region: Once all the dopant atoms have been ionised, the number of carriers in the semiconductor material can be approximated by the values given in equation 3.23. This approximation is no longer dependent on temperature until the latter affects the intrinsic properties of the material.

$$n \approx N_D \qquad p \approx N_A \tag{3.23}$$

  The concentration of donor and acceptor dopant atoms is represented by N_D and N_A, respectively, for n-type and p-type doped materials.

- Intrinsic temperature region: The very high thermal energy enables electrons to transfer from the valence band to the conduction band.

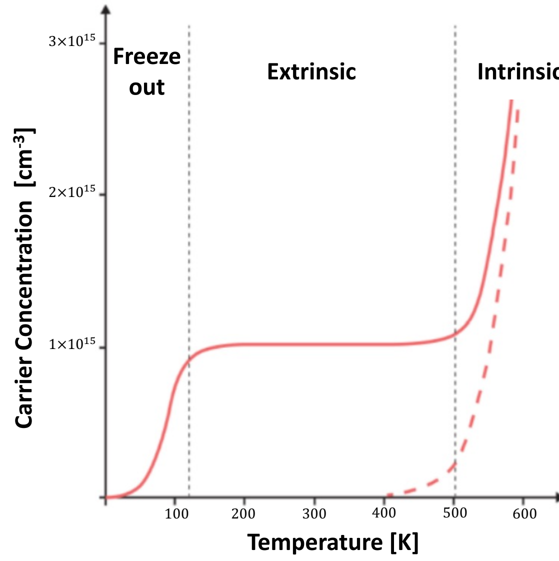

Figure 3.2: Evolution of carrier concentration in a semiconductor as a function of temperature reproduced from [85].

Figure 3.3 illustrates the evolution of the correction factor $P(N,T)$ as a function of doping within the semiconductor, for different temperatures expressed in Celsius.

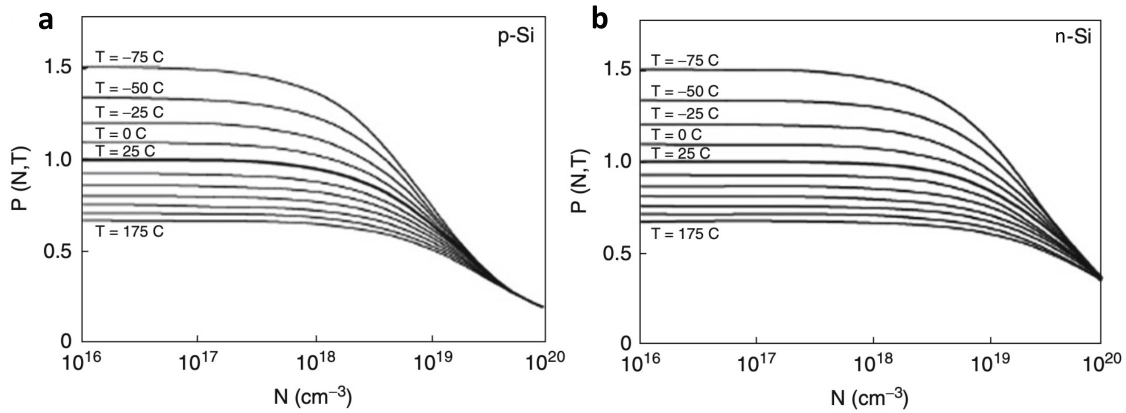

Figure 3.3: Correction factor $P(N,T)$ as a function of doping concentration and temperature for (a) p-type silicon and (b) n-type silicon from [72].

In the present study, the temperatures under consideration range from 300 to 355 K, or from 25 to 80°C. Figure 3.3 illustrates that the correction factor remains relatively constant at these temperatures as a function of doping up to $N_A = 10^{18}\text{cm}^{-3}$ for p-doped silicon, and $N_D = 10^{19}\text{cm}^{-3}$ for n-doped silicon. In the following sections, it is assumed that the doping level of the channel in the CMOS sensor under study is below the aforementioned values. In this case, the correction factor doping term is neglected, and its expression is as follows:

$$P(T) \approx \frac{300}{T} \tag{3.24}$$

Temperature dependencies of mobility, polysilicon resistor and threshold voltage

Considering the dependence of mobility on temperature, given by the relation $\mu \propto T^{\frac{-3}{2}}$ resulting from lattice scattering [86], the transconductance factor is rewritten:

$$\beta_i(\sigma, T) = \beta_{i,T_0}(\sigma)\left(\frac{T}{T_0}\right)^{-3/2} \tag{3.25}$$

With β_{i,T_0} the transconductance factor value at reference temperature T_0. The temperature dependence of simple resistor is derived from the following equation:

$$R(T) = R_{T_0}(1 + \alpha(T - T_0)) \tag{3.26}$$

With R_{T_0} the resistor value at reference temperature T_0 and α the temperature coefficient of the resistor. The variation in threshold voltage with temperature for the β_+-mutliplier has also been taken into account through the expression of the overdrive voltage:

$$V_{ov}^2(T) = (V_{bias} - V^{th}(T))^2 \tag{3.27}$$

$$V^{th}(T) = V_{T_0}^{th} + \frac{\partial V^{th}(T)}{\partial T} \tag{3.28}$$

With $V_{T_0}^{th} = V^{th}(T = T_0)$ the threshold voltage at the reference temperature.

Final expression of temperature dependency

The equations of current for the two topologies, taking into account the impact of temperature on the piezoresistive coefficients, mobility, resistance and threshold voltage, and neglecting the impact of doping, are defined as follows:

$$I_{\beta_R}(T,\sigma) = 2\frac{(e^{(\pi_{3,T_0}-\pi_{1,T_0}-\pi_{4,T_0})\frac{300}{T}\frac{\sigma}{2}} - e^{-\pi_{2,T_0}\frac{300}{T}\frac{\sigma}{2}}/\sqrt{K_{21}})^2 e^{2\pi_{r,T_0}\frac{300\sigma}{T}}}{R(T)^2\beta_{n,T_0}^0}\left(\frac{T}{T_0}\right)^{3/2} \tag{3.29}$$

$$I_{\beta+}(T,\sigma) = 2V_{ov}^2(T)\beta_{n,T_0}^0 \frac{(e^{(\pi_{3,T_0}-\pi_{1,T_0}-\pi_{4,T_0})\frac{300}{T}\frac{\sigma}{2}} - e^{\pi_{2,T_0}\frac{300}{T}\frac{\sigma}{2}}/\sqrt{K_{21}})^2}{\left[(e^{(\pi_{3,T_0}-\pi_{1,T_0}-\pi_{4,T_0})\frac{300}{T}\frac{\sigma}{2}} - e^{\pi_{2,T_0}\frac{300}{T}\frac{\sigma}{2}}/\sqrt{K_{21}})^2 + e^{\pi_{9,T_0}\frac{300\sigma}{T}}/K_{91}\right]^2}\left(\frac{T}{T_0}\right)^{-3/2} \tag{3.30}$$

Where the terms π_{j,T_0} are defined as the piezoresistive coefficient of transistor j at the reference temperature T_0.

3.2 Experimental methodology

3.2.1 Static analysis setup

All static measurements of the CMOS sensor at rest were conducted using the PM8PS probe. This prober is a low-signal probe station with a Probeshield and a thermal chuck, and is used for I-V and C-V measurements. The station is equipped with a module for temperature testing and has been employed for the characterisation of the device up to 80°C.

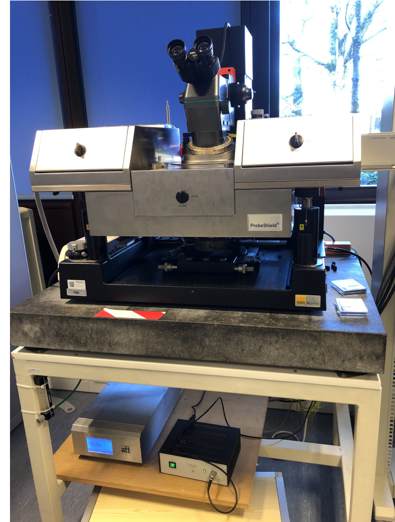

Figure 3.4: PM8PS prober employed for static characterization of the CMOS strain sensor.

3.2.2 Dynamic analysis setup

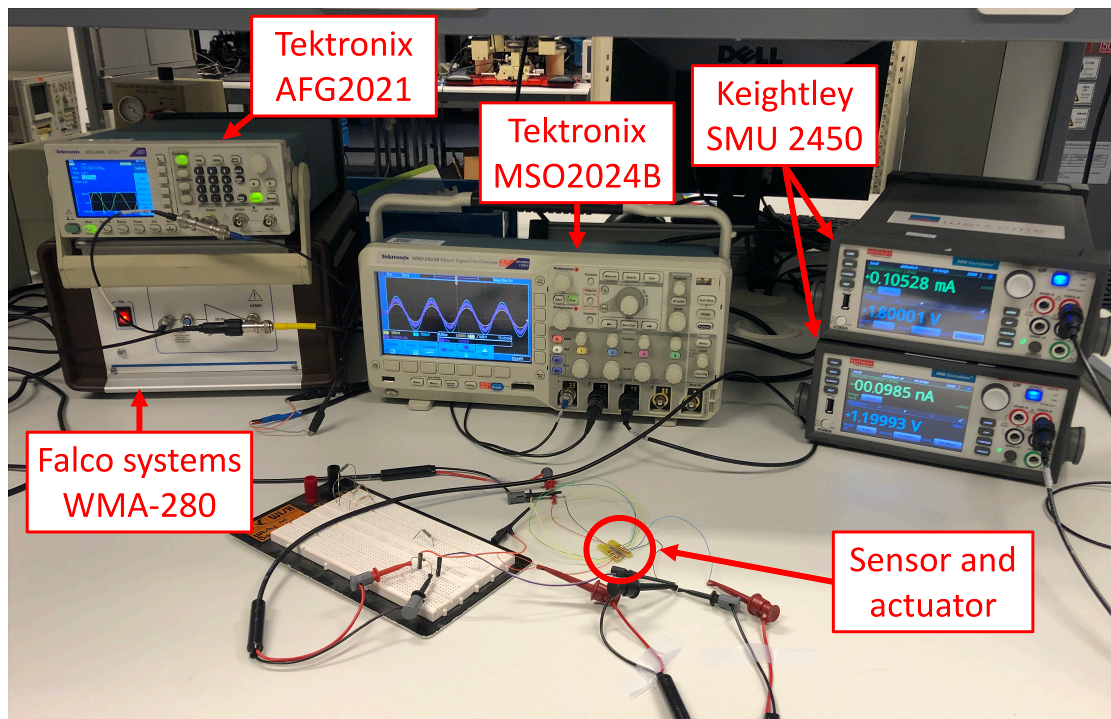

Figure 3.5: Setup for dynamic characterization of the CMOS strain sensor.

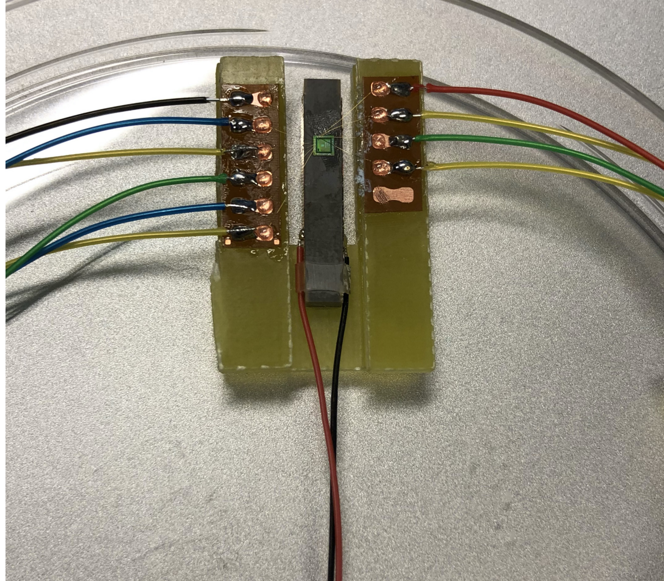

Figure 3.6: Assembly of the CMOS strain sensor on the piezoelectric actuator.

The setup is essentially similar to that employed in Chapter 2 for the dynamic analysis of the silicon gauge. The wave generator and amplifier are employed to supply the piezoelectric actuator. The two source meters are used as DC power supply to generate accurately the V_{DD} voltage of the CMOS circuit and the gate of transistor M9 of the β_+-multiplier see Figure 3.1. The sensor output is connected to a simple resistor so that its voltage drop can be measured on an oscilloscope. Figure 3.7 shows a simplified diagram of the connections in this setup.

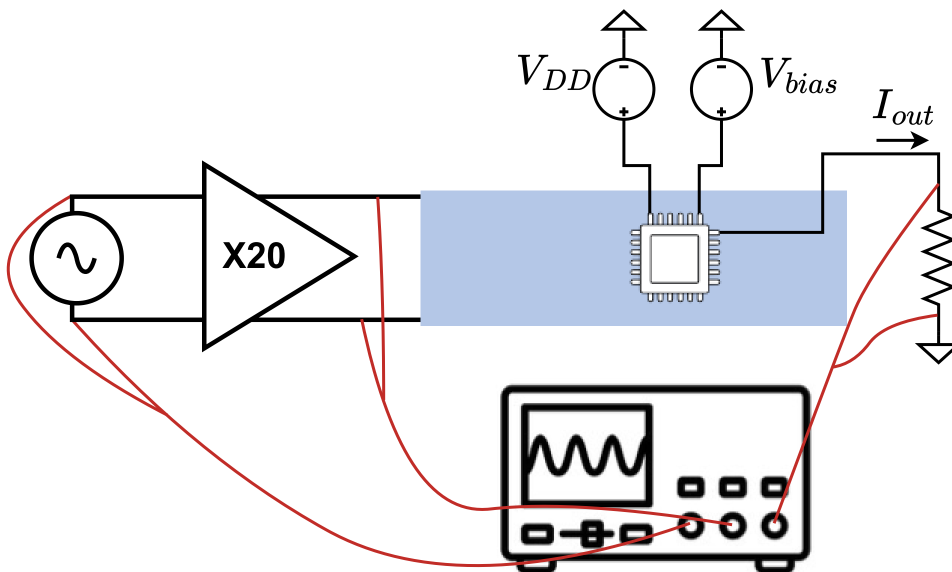

Figure 3.7: Scheme of the dynamic experimental setup for the CMOS sensor.

The piezoelectric actuator model used in this chapter is different from the one used in the previous one. The parameters specific to this model are given in Table 3.1. A slightly larger model has been chosen in order to have enough space for the sensor, which in turn increases the electrical capacitance of the actuator. The choice was made to minimise the value of this capacity in order to avoid reducing the system's bandwidth as much as possible.

Model	Dimensions AxBxL [mm]	Nominal displacement [μm]	Electrical capacitance [μF]	Resonant frequency [kHz]
P-882.51	3x2x18	15 ±10%	0.31 ±20%	70 ±20%

Table 3.1: Main parameters of the *P-882.51* actuator from Physik Instrumente [65].

CMOS sensor assembly

An assembly was carried out to simplify the integration of the sensor into the setup. The schemes of the different parts of the assembly are shown in Figure 3.8.

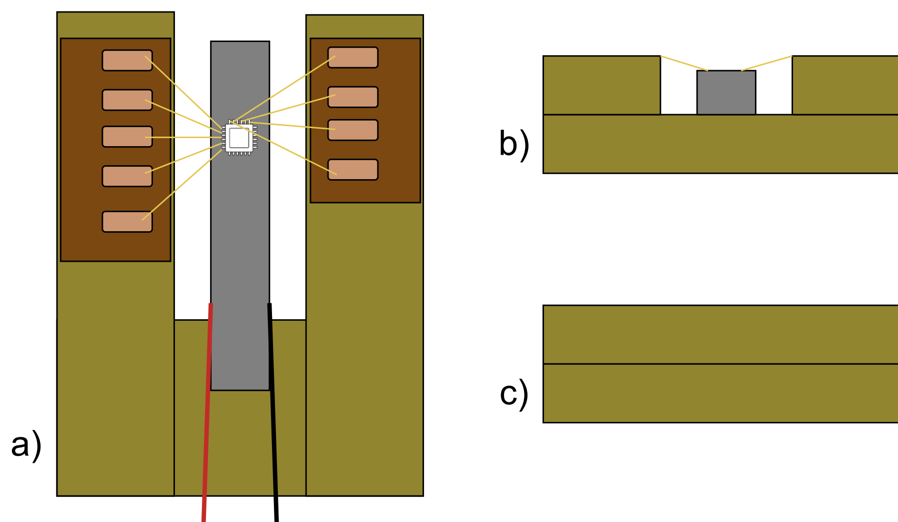

Figure 3.8: Top view (a), front view (b) and side view (c) of the assembly.

As the CMOS strain sensor is fabricated on a silicon die, it required wire bonding between its pads and copper contacts to connect it to the rest of the setup. Gold bond wires were used. Their fragility required a robust and stable anchor point to withstand the deformations the sensor underwent. The piezoelectric actuator is fixed at its base to the centre of a first U-shaped piece. Two pieces have been placed on either branch of this U, so that they can be raised to the height of the sensor pads which is on the piezoelectric actuator. Finally, simple cables were soldered to these copper contacts to connect the device sensor to the setup.

3.3 Measurements and results

3.3.1 Temperature testing and differential analysis with glued device

Extraction methodology

Temperature tests were performed on the device at rest, with no strain applied, both before and after the sensor was bonded to a steel strip. The tests were conducted between 25°C and 80°C in 5°C increments, with a 15-minute interval following the probe's reach of the specified temperature. The descent from 80 to 25°C was also measured. The methodology employed to extract the measurements is illustrated in Figure 3.9.

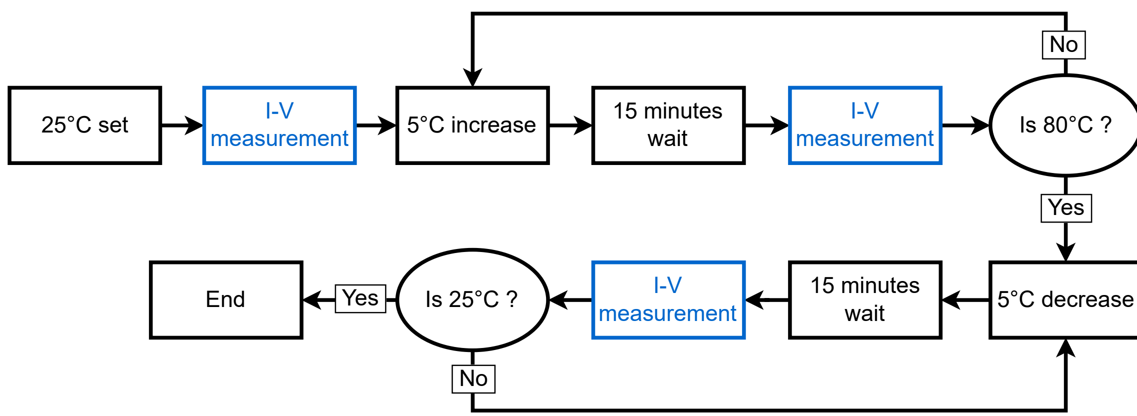

Figure 3.9: Flow diagram of the data extraction methodology for the temperature testing.

Under these conditions, i.e. without applied strain, and taking into account the effects of temperature, the expressions for the currents for the two topologies 3.29 and 3.30 are simplified:

$$I_{\beta_R}(T, \sigma = 0) = 2\frac{(1 - 1/\sqrt{K_{21}})^2}{R(T)^2 \beta^0_{n,T_0}} \left(\frac{T}{T_0}\right)^{3/2} \quad (3.31)$$

$$I_{\beta+}(T, \sigma = 0) = 2V^2_{ov}(T)\beta^0_{n,T_0} \frac{(1 - 1/\sqrt{K_{21}})^2}{\left[(1 - 1/\sqrt{K_{21}})^2 + 1/K_{91}\right]^2} \left(\frac{T}{T_0}\right)^{-3/2} \quad (3.32)$$

Temperature testing results

The results of the temperature tests are presented in Figure 3.10. In the analytical computation of currents, the various parameters that constitute the expressions 3.31 and 3.32 are derived from [63].

The resistor employed in the β_R configuration is made from poly-silicon and exhibits a nominal value of R_{T_0} =10kΩ at reference temperature. In the absence of strain, equation

3.26 is adapted to that given below by [87]:

$$R(T) \approx R_{T_0}(1 + \text{TCR}(T - T_0)) \tag{3.33}$$

The temperature coefficient of resistivity (TCR) describes the variation in resistance with temperature. In the case of a poly-silicon resistor, the value of the TCR is $100\frac{\text{ppm}}{\text{K}}$[87].

For the β_+ topology, the variation in threshold voltage for an NMOS transistor has been determined by [88] to be equal to $-1.27\frac{\text{mV}}{°\text{C}}$.

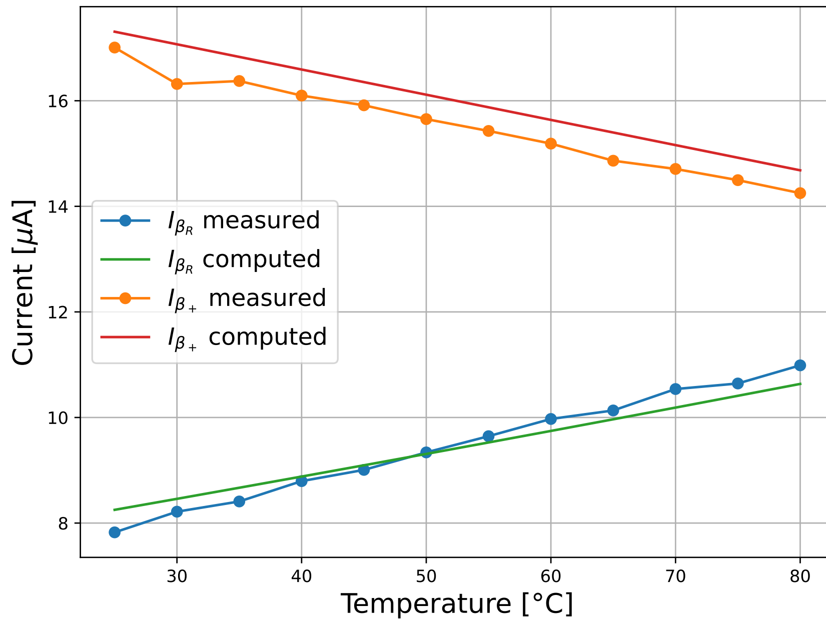

Figure 3.10: Impact of temperature on the current of the two topologies, with no strain applied between 25 and 80°C in 5°C steps. Analytically computed and measured results on the evice not glued yet.

Table 3.2 illustrates the diverse slopes of the current versus temperature curves for each of the topologies depicted in Figure 3.10. In addition, the table incorporates the theoretical sensor sensitivities outlined in [63]. The values estimated on the basis of equations 3.31 and 3.32 both underestimate the temperature sensitivity of the sensor. With regard to the β_R-multiplier, there is a 19% and 26% reduction in sensitivity compared with the theoretical and measured values, respectively. In the case of the β_+-multiplier, the sensitivity is underestimated by approximately 5% in both instances.

This has several possible meanings. Firstly, the device is placed on the chuck of the prober. Both materials have different coefficients of thermal expansion that are likely to leave residual stresses. The expression for the change in resistance with temperature of the polysilicon resistor is an approximation and has a second order term depending on the stress applied to the resistor [87].

Topology	Computed temperature sensitivity $[\frac{\text{nA}}{°\text{C}}]$	Theoritical temperature sensitivity $[\frac{\text{nA}}{°\text{C}}]$	Experimental temperature sensitivity $[\frac{\text{nA}}{°\text{C}}]$
β_R	42.3	52.06	56.97
β_+	-44.64	-47.74	-46.83

Table 3.2: Computed, theoritical from [63] and experimental temperature sensitivities of the two studied topologies.

Impact of bonding the device on sensor calibration

The material to which the sensor is bonded is likely to deform as the temperature rises, to a greater or lesser extent depending on its coefficient of thermal expansion.

In this work, the temperature tests were reproduced on the device once it had been bonded to a steel strip which has a coefficient of thermal expansion of $\alpha_{th,steel} = 12\mu\varepsilon/\text{K}$ [89]. Since silicon has a thermal expansion coefficient of $\alpha_{th,Si} = 2.6\mu\varepsilon/\text{K}$ [90], the deformation experienced by the sensor as a result of the temperature rise depends on the difference between the two expansion coefficients:

$$\alpha_{th,\text{effective}} = \alpha_{th,steel} - \alpha_{th,Si} = 9.4\frac{\mu\varepsilon}{\text{K}} \tag{3.34}$$

Assuming that the device is perfectly bonded and undergoes all the deformation generated by the steel strip, the transistors of the CMOS sensor are subjected to the following stress as a function of temperature:

$$\sigma(T) = E\ \alpha_{th,\text{effective}}\ (T - T_0) = 1.551(T - T_0)\ \text{ MPa} \tag{3.35}$$

With T_0=25°C=298.15K the reference temperature and $E = 165$GPa the Young's modulus of silicon in the [110] crystal direction [91]. The steel expands, a positive stress is considered. Once the device is bonded to a material, the simplified expressions 3.31 and 3.32 are no longer valid. The current-temperature dependencies for the two topologies are computed using the equations 3.29 and 3.30 and by injecting the stress 3.35.

The difference between what is computed and what is measured is quite significant. These differences may be a consequence of the initial assumptions. Firstly, the bond is assumed to be perfect, whereas in practice, depending on the quality of the bond, it can potentially attenuate the deformations imposed by the strip.

Secondly, the current equations and the parameters chosen to compute them assume an uniaxial stress, which is not the case when the steel strip and the sensor expand. Steel is an isotropic material, which means that it expands in all directions when subjected to temperature changes, thereby generating stress in all directions. This phenomenon is not taken into account in the expression of the piezoresistive coefficients.

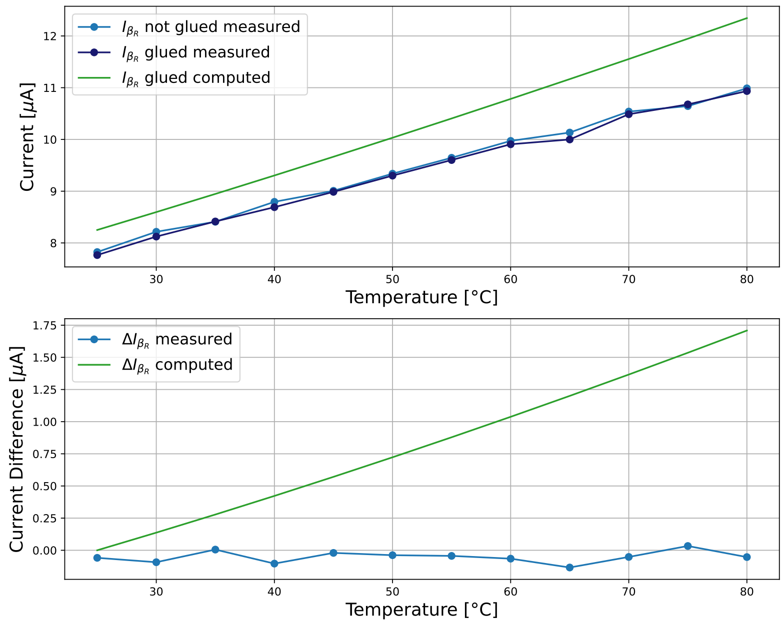

Figure 3.11: Impact of bonding the device to a steel strip at different temperatures on the current of the β_R-multiplier. Figure above: Currents measured before and after bonding and current computed after bonding. Figure below: difference between the measured currents and the computed currents before and after the bonding of the device.

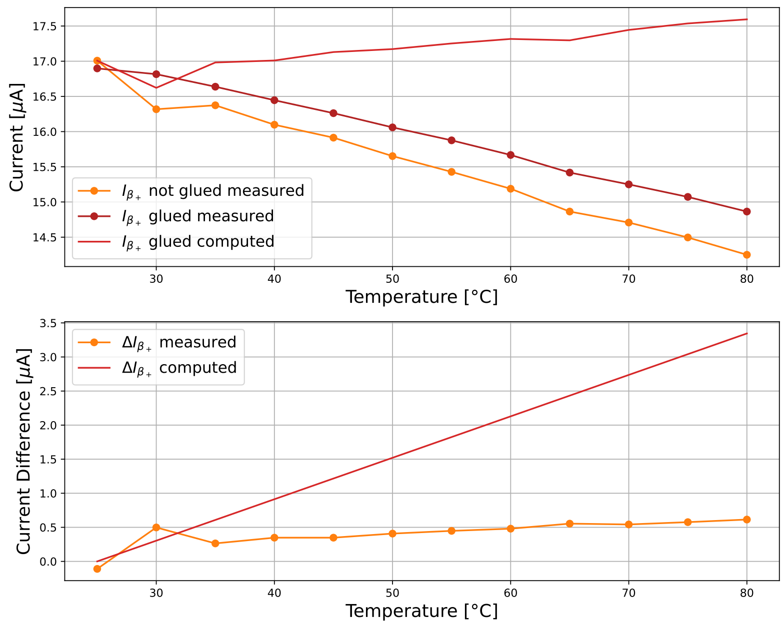

Figure 3.12: Impact of bonding the device to a steel strip at different temperatures on the current of the β_+-multiplier. Figure above: Currents measured before and after bonding and current computed after bonding. Figure below: difference between the measured currents and the computed currents before and after the bonding of the device.

3.3.2 UMC180 sensor under dynamic strain characterization

Extraction methodology

The principle remains the same as for the analysis of the silicon gage in the previous chapter. The frequency response of the system is determined by comparing the deformations estimated from the CMOS sensor current measurements and the deformations generated by the piezoelectric on the basis of its parameters.

$$H(f) = \frac{\varepsilon_{out}(f)}{\varepsilon_{in}(f)} \tag{3.36}$$

The strains generated by the piezoelectric are once again computed using Equation 2.37 shown below for ease of use:

$$\varepsilon_{in}(t) = \frac{V_{in,piezo}(t)}{V_{max,actuator}} \varepsilon_{max,actuator} \tag{3.37}$$

The piezoelectric actuator in this chapter is a different model to the one used with the silicon gauge. According to the datasheet, $V_{max,actuator}$ and $\varepsilon_{max,actuator}$ are 100V and 833.33$\mu\varepsilon$ respectively. The deformation measured by the CMOS sensor at the output is determined using the expression:

$$\varepsilon_{out}(t) = \frac{\frac{\Delta I(t)}{I_0}}{K} \tag{3.38}$$

Where K is the theoretical gauge factor taken from [63] for the two topologies: 324 for the β_R-multiplier and 415 for the β_+-multiplier. $\Delta I(t)$ is the variation of the transducer current with respect to the current at rest I_0. The current extracted from the transducer can be seen as the sum of a higher value DC component and a lower value AC component dependent on the applied stress, which in turn is dependent on the voltage applied to the piezoelectric actuator.

The code used to automate the measurements and the extraction method in Figure 2.12 from the previous chapter have been reused here.

Experimental model

For the reader's convenience, the model established for the initial setup in chapter 2, which is employed in the dynamic analysis of the CMOS strain sensor, is illustrated in Figure 3.13. In order to obtain the BVD model parameters for this configuration, the methodology described in section 2.3.3 is applied to the new actuator model, resulting in the parameters presented in Table 3.3.

The resonant frequency related to the mechanical branch for this model of piezoelectric actuator is therefore equal to:

$$f_{cut_off} = \frac{1}{2\pi\sqrt{C_m L_m}} = 70\text{kHz} \tag{3.39}$$

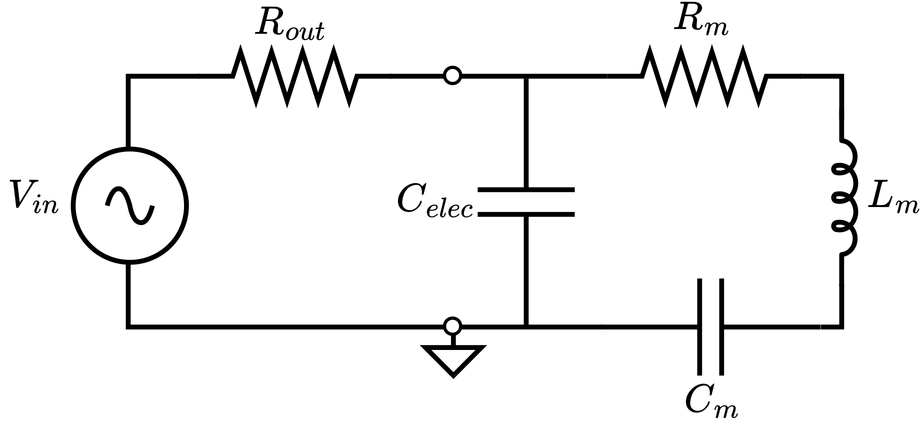

Figure 3.13: Equivalent circuit of the actuator setup without the amplifier used.

Components	C_{elec}	R_m	L_m	C_m	R_{out}
Value	0.31[μF]	1[Ω]	56[μH]	92.3[nF]	50[Ω]

Table 3.3: Parameters of setup of the dynamic analysis of the CMOS strain sensor and the Butterworth Van Dyke equivalent topology of the *P-882.51* piezoelectric actuator from Physik Instrumente.

The cut-off frequency of the low pass filter formed by R_{out} and C_{elec} is set to:

$$f_{cut_off} = \frac{1}{2\pi R_{out} C_{elec}} = 10.268\text{kHz} \tag{3.40}$$

Figure 3.14 depicts the theoretical response of the complete system in relation to the established model.

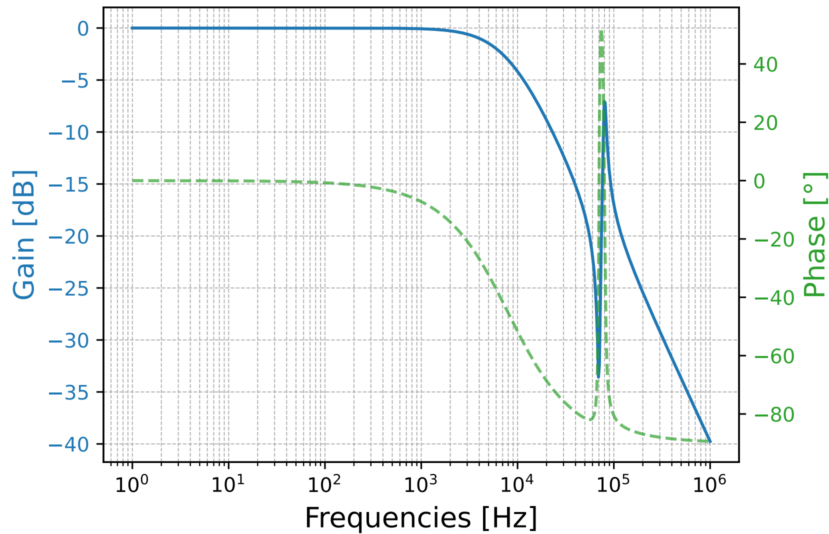

Figure 3.14: Bode diagram of the system frequency response using LTSpice.

Dynamic analysis results

The results of the dynamic analysis of the system, as measured by the CMOS strain sensor, are presented in Figure 3.15.

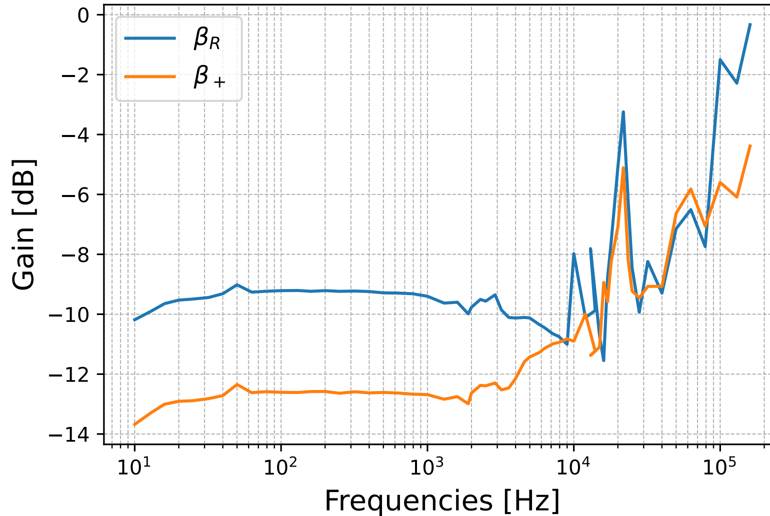

Figure 3.15: Frequency response of the system measured by the CMOS strain sensor. Measurements of the β_R-multiplier in blue and the β_R-multiplier in orange.

The results demonstrate a stable plateau in frequency response up to approximately 2–3 kHz. A first resonant peak in the β_R-multiplier occurs at 10 kHz, followed by another peak in both topologies at 21 kHz. From this point, the results become increasingly random due to the low-pass filter generated by the actuator's electrical capacitance combined with the signal generator's output resistance, which significantly reduces the amplitude of the signals. However, a peak can be identified at 70 kHz, corresponding to the mechanical resonance of the actuator.

A comparison of the results presented in Figure 3.15 with the Bode diagram of the system generated by LTSpice from 3.14 reveals the presence of two peaks at 10 kHz and 21 kHz, which are not expected. To investigate this more closely, Figures 3.16 and 3.17 illustrate the signal at the input of the piezoelectric actuator and the voltage measured across a 100kΩ resistor through which the output currents of the transducer were measured.

Figures 3.16 and 3.17 illustrate that the resonance peaks at 10 kHz for the β_R-multiplier and the peak at 21 kHz for the two topologies in the transfer function are generated by a peak present only in the measurements of the sensor outputs. As the input voltage of the piezoelectric actuator follows the curve predicted by the established model, it can be concluded that this is not a case of electronic resonance in the power supply setup as may have been the case in certain configurations in the chapter 2. Two different assumptions can be made:

- Either this is an unexpected mechanical resonance in the behaviour of the actuator.

Given that this phenomenon did not occur during the strain gauge's dynamic testing and considering the reliability of PI ceramic products, this hypothesis is less probable.

- Or it is possible that these are electrical resonance peaks that manifest during the operation of the CMOS sensor at the moment of the measurements. However, to confirm this potential justification for the observed behaviour, it would be necessary to conduct an in-depth theoretical study of the behaviour in the dynamic regime and test the sensor on several measurement sets.

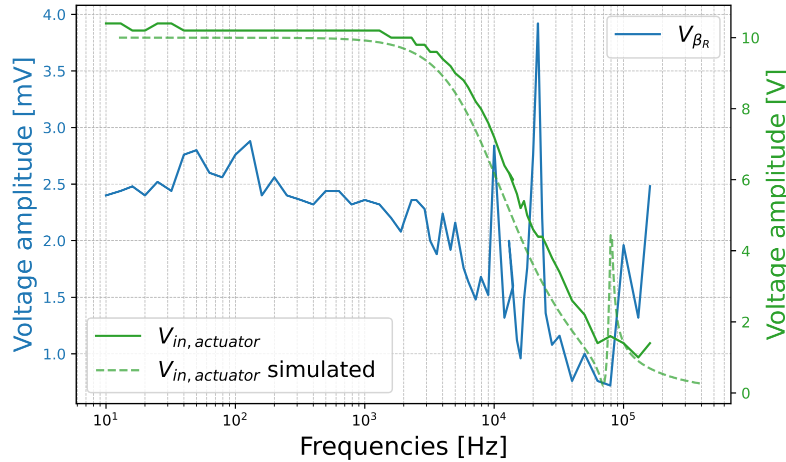

Figure 3.16: Signal at the input of the piezoelectric actuator in green solid line and its simulated signal on the basis of the transfer function in green dashed line. Voltage measured at a 100kΩ resistor through which the output current of the β_R-multiplier in blue passes.

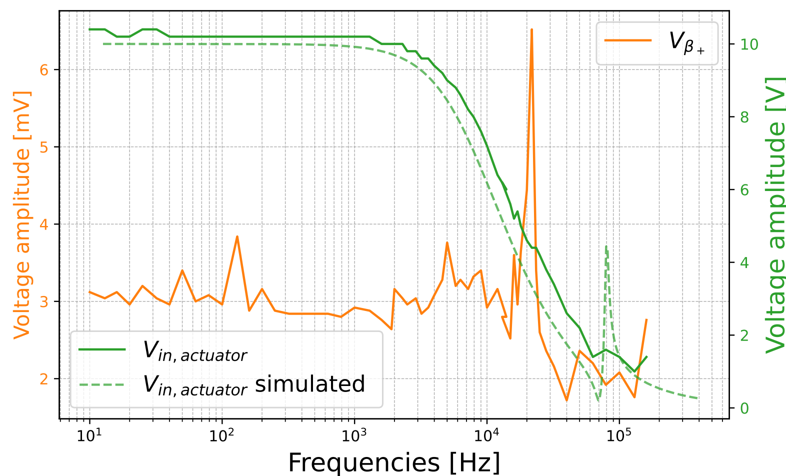

Figure 3.17: Signal at the input of the piezoelectric actuator in green solid line and its simulated signal on the basis of the transfer function in green dashed line. Voltage measured at a 100kΩ resistor through which the output current of the β_R-multiplier in orange passes.

3.4 Conclusion and recommendations

This chapter aimed to characterize the CMOS strain sensor and analyze its dynamic behavior, particularly under the influence of temperature on its piezoresistive coefficients. Additionally, the temperature dependencies of different current terms, including the polysilicon resistance for the β_R-multiplier and the threshold voltage for the β_+-multiplier, were integrated into the analysis.

Thermal measurements demonstrated a good agreement between theoretical values, computed values, and measured temperature sensitivity for the β_+-multiplier. However, for the β_R-multiplier, there was a notable disparity, likely due to an oversimplified estimation of the polysilicon resistor's behavior. The temperature tests conducted on the sensor after bonding to a steel strip revealed significant divergences between expected and observed deformation levels. This difference was attributed to the initial current equations, which assumed uniaxial stress, whereas the bonded steel, being isotropic, deformed and generated stress in all directions.

The study highlighted the limitations of the current model in predicting sensor behavior when bonded to an isotropic material. However, the results suggest that the model could be adapted for use with anisotropic materials, where the directions and magnitudes of stress due to thermal expansion could be more accurately predicted and matched to the initial assumptions on the current expressions.

The frequency response of the CMOS strain sensor was evaluated, showing stable performance up to 3 kHz. However, unexpected resonance peaks were observed, affecting measurement accuracy. The source of these resonances remains unidentified, indicating the need for further investigation to isolate potential causes. The study demonstrated that the sensor can reliably capture the frequency response of a dynamic strain system up to 3 kHz, although this bandwidth might be limited by external factors rather than the sensor itself.

During the dynamic analysis, significant challenges were encountered, particularly with the durability of the setup. The setup experienced multiple failures, primarily due to the recurrent breakage of the gold wires used for wire bonding on the silicon chip. The device contained ten wire-bonded connections, but only five were actively used for measurements. Notably, it was observed that the majority of the breakages occurred in these five critical wires. It was assumed that breakages were linked to two factors:

- The vibrations and deformations generated by the piezoelectric actuator were observed. The system was subjected to mechanical resonance effects, which generated displacements of up to approximately 2 μm along the length of the actuator.
- The possibility of heat generation due to repeated and prolonged use of these connections.

Given these issues, future work should consider reinforcing the wire bonding welds on the

sensor side by providing additional mechanical support.

This chapter has enabled to experiment with the temperature dependence of the CMOS strain sensor and to analyse its dynamic behaviour. However, the challenges encountered, including uncertainties in the frequency response results and repeated connection failures, indicate the necessity of improvements of the sensor model and enhancements of the experimental setup for more reliable dynamic testing in the future.

Conclusion

This work enabled an in-depth exploration of the dynamic characterization of a CMOS strain sensor exploiting piezoresistive effects in silicium. The study was structured around three main chapters to aiming to answer various objectives included the development of a theoretical and experimental model to analyse the dynamic behaviour of strain sensors, as well as the evaluation of the impact of temperature on CMOS sensor operation.

The first chapter contextualized structural health monitoring techniques and the different types of sensors used in this field. This section placed the importance of the CMOS sensor developed in this work in relation to other available technologies, highlighting its high sensitivity, low power consumption and small size. This established the relevance and potential of the CMOS sensor for SHM applications and justified the subsequent technical studies.

The second chapter focused on developing and validating an experimental model using a silicon strain sensor coupled to a piezoelectric actuator to simulate structural vibrations. The model, based on a Butterworth Van Dyke topology, accurately predicted the system's frequency response, with experimental validation confirming its robustness. These results demonstrated the validity of the model with regards to the proposed setup, which demonstrated the functionality of the strain gage up to 4kHz. However, challenges such as noise and unexpected inductive effects highlighted the complexity of dynamic system modelling and the areas for potential future enhancement.

The third chapter investigated the dynamic behavior and thermal sensitivity of the CMOS strain sensor under various conditions. The dynamic analysis revealed that the sensor demonstrated a stable frequency response up to 3 kHz, validating its potential for high-frequency applications in SHM. However, the study also uncovered unexpected resonance peaks, which introduced inaccuracies in the measurements. These resonances were not fully understood, suggesting that further research is required to identify their sources and mitigate their effects. Thermal analysis of the sensor showed significant differences between the theoretically determined analytical expression and the measured results. This indicated the need for better modeling of different temperature dependencies of the equations, such as the polysilicon resistor, and a deeper understanding of the sensor's behavior when bonded to isotropic materials.

In summary, this work showed the CMOS strain sensor's dynamic capabilities and also

highlighted key areas for improvement, for example to model thermal behaviour and the robustness of the experimental setup. Future research could focus on solidifying the sensor connections and then improve the sensor model to account temperature variations more accurately, and further exploring the sensor's integration into complex systems. These developments will be essential for the realization of the sensor's full potential in aerospace engineering applications per example, where accurate and reliable measurements are essential for maintaining the safety and longevity of critical structures.

Bibliography

[1] Minhang Bao. "Chapter 1 - Introduction to MEMS Devices". In: *Analysis and Design Principles of MEMS Devices*. Ed. by Minhang Bao. Amsterdam: Elsevier Science, 2005, pp. 1–32. ISBN: 978-0-444-51616-9. DOI: https://doi.org/10.1016/B978-044451616-9/50002-3. URL: https://www.sciencedirect.com/science/article/pii/B9780444516169500023.

[2] Rahul Reddy Nagavally. "Composite materials-history, types, fabrication techniques, advantages, and applications". In: *Int. J. Mech. Prod. Eng* 5.9 (2017), pp. 82–87.

[3] Victor Giurgiutiu. "Chapter 1 - Introduction". In: *Structural Health Monitoring of Aerospace Composites*. Ed. by Victor Giurgiutiu. Oxford: Academic Press, 2016, pp. 1–23. ISBN: 978-0-12-409605-9. DOI: https://doi.org/10.1016/B978-0-12-409605-9.00001-5. URL: https://www.sciencedirect.com/science/article/pii/B9780124096059000015.

[4] Helena Rocha, Christopher Semprimoschnig, and João P. Nunes. "Sensors for process and structural health monitoring of aerospace composites: A review". In: *Engineering Structures* 237 (2021), p. 112231. ISSN: 0141-0296. DOI: https://doi.org/10.1016/j.engstruct.2021.112231. URL: https://www.sciencedirect.com/science/article/pii/S0141029621003813.

[5] Dongfang Zhao et al. "3D Printed and Embedded Strain Sensors in Structural Composites for Loading Monitoring and Damage Diagnostics". In: *Journal of Composites Science* 7.10 (2023). ISSN: 2504-477X. DOI: 10.3390/jcs7100437. URL: https://www.mdpi.com/2504-477X/7/10/437.

[6] *Vallen systeme - Structural Health Monitoring*. URL: https://www.vallen.de/applications/structural-health-monitoring-shm/ (visited on 07/15/2024).

[7] Onur Avci et al. "A review of vibration-based damage detection in civil structures: From traditional methods to Machine Learning and Deep Learning applications". In: *Mechanical Systems and Signal Processing* 147 (2021), p. 107077. ISSN: 0888-3270. DOI: https://doi.org/10.1016/j.ymssp.2020.107077. URL: https://www.sciencedirect.com/science/article/pii/S0888327020304635.

[8] Daniel Caicedo, Luis A. Lara-Valencia, and JosÃ© Brito. "Frequency-based methods for the detection of damage in structures: A chronological review". en. In: *DYNA* 88 (Sept. 2021), pp. 203–211. ISSN: 0012-7353. URL: http://www.scielo.org.co/scielo.php?script=sci_arttext&pid=S0012-73532021000300203&nrm=iso.

[9] Duong Huong Nguyen and Magd Abdel Wahab. "Damage detection in slab structures based on two-dimensional curvature mode shape method and Faster R-CNN". In: *Advances in Engineering Software* 176 (2023), p. 103371. ISSN: 0965-9978. DOI: https://doi.org/10.1016/j.advengsoft.2022.103371. URL: https://www.sciencedirect.com/science/article/pii/S0965997822002721.

[10] Raquel Almeida. "An assessment of frequency response curvature methods for damage localization". In: (Sept. 2014).

[11] M.C. Porcu et al. "Effectiveness of the FRF curvature technique for structural health monitoring". In: *Construction and Building Materials* 226 (2019), pp. 173–187. ISSN: 0950-0618. DOI: https://doi.org/10.1016/j.conbuildmat.2019.07.123. URL: https://www.sciencedirect.com/science/article/pii/S0950061819317957.

[12] Pengming Zhan et al. "Damage identification in beam-like structure using strain FRF-based damage index and artificial neural network". In: *Mechanics of Advanced Materials and Structures* 30 (Apr. 2022), pp. 1–19. DOI: 10.1080/15376494.2022.2055241.

[13] Alvar M. Kabe and Brian H. Sako. "Chapter 6 - Experimental structural dynamics". In: *Structural Dynamics Fundamentals and Advanced Applications*. Ed. by Alvar M. Kabe and Brian H. Sako. Academic Press, 2020, pp. 429–511. ISBN: 978-0-12-821615-6. DOI: https://doi.org/10.1016/B978-0-12-821615-6.00006-X. URL: https://www.sciencedirect.com/science/article/pii/B978012821615600006X.

[14] Robert Ebeling, Russell Green, and Samuel French. *Accuracy of Response of Single-Degree-of-Freedom Systems to Ground Motion*. Dec. 1997.

[15] Wenguang Liu and M. Barkey. "The Effects of Breathing Behaviour on Crack Growth of a Vibrating Beam". In: *Shock and Vibration* 2018 (Mar. 2018), pp. 1–12. DOI: 10.1155/2018/2579419.

[16] R.P.C. Sampaio, N.M.M. Maia, and J.M.M. Silva. "Damage detection using the frequency-response-function curvature method". In: *Journal of Sound and Vibration* 226.5 (1999), pp. 1029–1042. ISSN: 0022-460X. DOI: https://doi.org/10.1006/jsvi.1999.2340. URL: https://www.sciencedirect.com/science/article/pii/S0022460X99923404.

[17] Varsha Patil and Dhiraj Ahiwale. "Damage detection of warren truss bridge using frequency change correlation". In: *Materials Today: Proceedings* 56 (2022). International Conference on Materials, Machines and Information Technology-2022, pp. 18–28. ISSN: 2214-7853. DOI: https://doi.org/10.1016/j.matpr.2021.11.483. URL: https://www.sciencedirect.com/science/article/pii/S2214785321075052.

[18] C. Amara Chandra and Prasanta Kumar Samal. "Experimental determination of mode shapes of beams by roving impact test". In: *Materials Today: Proceedings* 46 (2021). International Mechanical Engineering Congress 2019, pp. 9159–9163. ISSN: 2214-7853. DOI: https://doi.org/10.1016/j.matpr.2020.01.119. URL: https://www.sciencedirect.com/science/article/pii/S2214785320301814.

[19] Tianxiang Huang et al. “A baseline-free damage detection method based on node displacement in mode shape”. In: 2016. URL: https://api.semanticscholar.org/CorpusID:113560990.

[20] Duong Huong Nguyen and Magd Abdel Wahab. “Damage detection in slab structures based on two-dimensional curvature mode shape method and Faster R-CNN”. In: *Advances in Engineering Software* 176 (2023), p. 103371. ISSN: 0965-9978. DOI: https://doi.org/10.1016/j.advengsoft.2022.103371. URL: https://www.sciencedirect.com/science/article/pii/S0965997822002721.

[21] D. Wu and S.S. Law. “Damage localization in plate structures from uniform load surface curvature”. In: *Journal of Sound and Vibration* 276.1 (2004), pp. 227–244. ISSN: 0022-460X. DOI: https://doi.org/10.1016/j.jsv.2003.07.040. URL: https://www.sciencedirect.com/science/article/pii/S0022460X03009878.

[22] Jon Wilson. *Sensor Technology Handbook*. Jan. 2005. DOI: 10.1016/B978-0-7506-7729-5.X5040-X.

[23] Woo-Tae Park. “Piezoresistivity”. In: *Encyclopedia of Nanotechnology*. Ed. by Bharat Bhushan. Dordrecht: Springer Netherlands, 2012, pp. 2111–2117. ISBN: 978-90-481-9751-4. DOI: 10.1007/978-90-481-9751-4_222. URL: https://doi.org/10.1007/978-90-481-9751-4_222.

[24] Y. Liu et al. “Thermal-Performance Instability in Piezoresistive Sensors: Inducement and Improvement”. In: *Sensors (Basel)* 16.12 (Nov. 2016), p. 1984. DOI: 10.3390/s16121984.

[25] Ville Kaajakari. *Practical MEMS*. Boca Raton, FL: CRC Press, 2009.

[26] Yongke Sun, Toshikazu Nishida, and Scott E. Thompson. “Piezoresistive Strain Sensors”. In: *Strain Effect in Semiconductors: Theory and Device Applications*. Boston, MA: Springer US, 2010, pp. 267–290. ISBN: 978-1-4419-0552-9. DOI: 10.1007/978-1-4419-0552-9_8. URL: https://doi.org/10.1007/978-1-4419-0552-9_8.

[27] Wojciech Sas, Katarzyna Gabrys, and Alojzy Szymański. “Determination of Poisson’s ratio by means of resonant column tests”. In: *Electronic Journal of Polish Agricultural Universities (EJPAU)* 16 (May 2015).

[28] Jianqiang Han et al. “A low cross-axis sensitivity piezoresistive accelerometer fabricated by masked-maskless wet etching”. In: *Sensors and Actuators A: Physical* 283 (2018), pp. 17–25. ISSN: 0924-4247. DOI: https://doi.org/10.1016/j.sna.2018.09.040. URL: https://www.sciencedirect.com/science/article/pii/S0924424718308045.

[29] Ferran Reverter et al. “Novel and low-cost temperature compensation technique for piezoresistive pressure sensors”. In: vol. 4. Sept. 2009.

[30] Soumendu Sinha et al. “Design and Simulation of MEMS Differential Capacitive Accelerometer”. In: (July 2014). DOI: 10.13140/2.1.1074.8809.

[31] *All about circuits - Introduction to Capacitive Accelerometers: Measuring Acceleration with Capacitive Sensing.* URL: https://www.allaboutcircuits.com/technical-articles/introduction-to-capacitive-accelerometer-measure-acceleration-capacitive-sensing/ (visited on 07/16/2024).

[32] Ghada Ahmed Khouqeer et al. "Design of MEMS capacitive comb accelerometer with perforated proof mass for seismic applications". In: *Journal of King Saud University - Science* 35.3 (2023), p. 102560. ISSN: 1018-3647. DOI: https://doi.org/10.1016/j.jksus.2023.102560. URL: https://www.sciencedirect.com/science/article/pii/S1018364723000228.

[33] "IEEE Standard on Piezoelectricity". In: *ANSI/IEEE Std 176-1987* (1988). DOI: 10.1109/IEEESTD.1988.79638.

[34] Sandeep Khandai and Sachin Jain. "Comparison of sensors performance for the development of wrist pulse acquisition system". In: Nov. 2017, pp. 2870–2875. DOI: 10.1109/TENCON.2017.8228351.

[35] Diederik Van Nuffel et al. "Calibration of dynamic piezoelectric force transducers using the hopkinson bar technique". In: 2012. URL: https://api.semanticscholar.org/CorpusID:58907807.

[36] Steve Vanlanduit et al. "Strain Monitoring". In: *Structural Health Monitoring Damage Detection Systems for Aerospace*. Ed. by Markus G. R. Sause and Elena Jasiūnienė. Cham: Springer International Publishing, 2021, pp. 219–241. ISBN: 978-3-030-72192-3. DOI: 10.1007/978-3-030-72192-3_8. URL: https://doi.org/10.1007/978-3-030-72192-3_8.

[37] Carlo Massaroni, Paola Saccomandi, and Emiliano Schena. "Medical Smart Textiles Based on Fiber Optic Technology: An Overview". In: *Journal of Functional Biomaterials* 6 (Apr. 2015), pp. 204–221. DOI: 10.3390/jfb6020204.

[38] S.-C Her and C.-Y Huang. "Thermal strain measured by fiber Bragg grating sensors". In: 28 (Jan. 2016), pp. 939–946. DOI: 10.18494/SAM.2016.1255.

[39] *BCM sensor - Semi conductor strain gauges datasheet.* URL: https://www.bcmsensor.com/wp-content/uploads/2015/09/210705_Semiconductor_Strain_Gauges.pdf.

[40] Omega Engineering. *Strain Gauge Technical Data.* 2023. URL: https://www.omega.co.uk/techref/pdf/strain_gage_technical_data.pdf (visited on 08/14/2024).

[41] A.S. Fiorillo, Davide C. Critello, and Salvatore Pullano. "Theory, Technology and Applications of Piezoresistive Sensors: a Review". In: *Sensors and Actuators A: Physical* 281 (July 2018). DOI: 10.1016/j.sna.2018.07.006.

[42] J. Fraden. *Handbook of Modern Sensors: Physics, Designs, and Applications.* Springer New York, 2010. ISBN: 9781441964663. URL: https://books.google.be/books?id=W0Emv9dAJ1kC.

[43] Min Su et al. "Textile-Based Flexible Capacitive Pressure Sensors: A Review". In: *Nanomaterials* 12 (Apr. 2022), p. 1495. DOI: 10.3390/nano12091495.

[44] Huikai Xie, Gary K. Fedder, and Robert E. Sulouff. "2.05 - Accelerometers". In: *Comprehensive Microsystems*. Ed. by Yogesh B. Gianchandani, Osamu Tabata, and Hans Zappe. Oxford: Elsevier, 2008, pp. 135–180. ISBN: 978-0-444-52190-3. DOI: https://doi.org/10.1016/B978-044452190-3.00053-7. URL: https://www.sciencedirect.com/science/article/pii/B9780444521903000537.

[45] Hussein Nesser and Gilles Lubineau. "Strain Sensing by Electrical Capacitive Variation: From Stretchable Materials to Electronic Interfaces". In: *Advanced Electronic Materials* 7 (Aug. 2021). DOI: 10.1002/aelm.202100190.

[46] Darrin Young et al. "A high-performance MEMS capacitive strain sensing system". In: *Sensors and Actuators A: Physical* 133 (Feb. 2007), pp. 272–277. DOI: 10.1016/j.sna.2006.06.015.

[47] K.I. Arshak, D. McDonagh, and M.A. Durcan. "Development of new capacitive strain sensors based on thick film polymer and cermet technologies". In: *Sensors and Actuators A: Physical* 79.2 (2000), pp. 102–114. ISSN: 0924-4247. DOI: https://doi.org/10.1016/S0924-4247(99)00275-7. URL: https://www.sciencedirect.com/science/article/pii/S0924424799002757.

[48] Hung Cao et al. "Development and Characterization of a Novel Interdigitated Capacitive Strain Sensor for Structural Health Monitoring". In: *IEEE Sensors Journal* 15.11 (2015), pp. 6542–6548. DOI: 10.1109/JSEN.2015.2461591.

[49] Michael Suster et al. "Low-noise CMOS integrated sensing electronics for capacitive MEMS strain sensors". In: Nov. 2004, pp. 693–696. DOI: 10.1109/CICC.2004.1358922.

[50] Robert Puers. "Capacitive sensors: When and how to use them". In: *Sensors and Actuators A: Physical* 37-38 (1993). Proceedings of Eurosensors VI, pp. 93–105. ISSN: 0924-4247. DOI: https://doi.org/10.1016/0924-4247(93)80019-D. URL: https://www.sciencedirect.com/science/article/pii/092442479380019D.

[51] Zhenjie Ji and Menglun Zhang. "Highly sensitive and stretchable piezoelectric strain sensor enabled wearable devices for real-time monitoring of respiratory and heartbeat simultaneously". In: *Nanotechnology and Precision Engineering* 5.1 (Feb. 2022), p. 013002. ISSN: 1672-6030. DOI: 10.1063/10.0009365. eprint: https://pubs.aip.org/tu/npe/article-pdf/doi/10.1063/10.0009365/19820931/013002_1_online.pdf. URL: https://doi.org/10.1063/10.0009365.

[52] PCB Piezotronics. *PCB Products*. 2023. URL: https://www.pcb.com/products?m=740b02 (visited on 08/14/2024).

[53] Kistler. *SAP Commerce - Download Original*. 2022. URL: https://kistler.cdn.celum.cloud/SAPCommerce_Download_original/000-823e.pdf (visited on 08/14/2024).

[54] Jayant Sirohi and Inderjit Chopra. "Fundamental Understanding of Piezoelectric Strain Sensors". In: *Journal of Intelligent Material Systems and Structures - J INTEL MAT SYST STRUCT* 11 (Apr. 2000), pp. 246–257. DOI: 10.1106/8BFB-GC8P-XQ47-YCQ0.

[55] Takahiro Yamashita et al. “Ultra-Thin Piezoelectric Strain Sensor Array Integrated on a Flexible Printed Circuit Involving Transfer Printing Methods”. In: *IEEE Sensors Journal* 16.24 (2016), pp. 8840–8846. DOI: 10.1109/JSEN.2016.2578936.

[56] Chris Wallbrink, James M. Hughes, and Andrei Kotousov. “Application of an advanced piezoelectric strain sensor for crack closure measurement”. In: *International Journal of Fatigue* 167 (2023), p. 107286. ISSN: 0142-1123. DOI: https://doi.org/10.1016/j.ijfatigue.2022.107286. URL: https://www.sciencedirect.com/science/article/pii/S0142112322005369.

[57] Ruiya Li et al. “Sensitivity Enhancement of FBG-Based Strain Sensor”. In: *Sensors* 18.5 (2018). ISSN: 1424-8220. DOI: 10.3390/s18051607. URL: https://www.mdpi.com/1424-8220/18/5/1607.

[58] Yongxing Guo et al. “Design and Investigation of a Reusable Surface-Mounted Optical Fiber Bragg Grating Strain Sensor”. In: *IEEE Sensors Journal* 16.23 (2016), pp. 8456–8462. DOI: 10.1109/JSEN.2016.2614009.

[59] Yinggang Liu et al. “Simultaneous measurement of temperature and strain based on SCF-based MZI cascaded with FBG”. In: *Appl. Opt.* 59.30 (Oct. 2020), pp. 9476–9481. DOI: 10.1364/AO.405670. URL: https://opg.optica.org/ao/abstract.cfm?URI=ao-59-30-9476.

[60] Jae-Min Kim et al. “Enhanced Strain Measurement Range of an FBG Sensor Embedded in Seven-Wire Steel Strands”. In: *Sensors* 17.7 (July 2017), p. 1654. DOI: 10.3390/s17071654.

[61] Honglin Zhang et al. “Dynamic Strain Measurement of Rotor Blades in Helicopter Flight Using Fiber Bragg Grating Sensor”. In: *Sensors* 23 (July 2023), p. 6692. DOI: 10.3390/s23156692.

[62] T.H. Loutas et al. “Intelligent health monitoring of aerospace composite structures based on dynamic strain measurements”. In: *Expert Systems with Applications* 39.9 (2012), pp. 8412–8422. ISSN: 0957-4174. DOI: https://doi.org/10.1016/j.eswa.2012.01.179. URL: https://www.sciencedirect.com/science/article/pii/S0957417412002072.

[63] Nicolas Roisin et al. “Low-power silicon strain sensor based on CMOS current reference topology”. In: *Sensors and Actuators A: Physical* 339 (2022), p. 113491. ISSN: 0924-4247. DOI: https://doi.org/10.1016/j.sna.2022.113491. URL: https://www.sciencedirect.com/science/article/pii/S0924424722001297.

[64] Nicolas Roisin. “Ultra-low-power strain SOI sensor for wind turbine applications”. Prom. : Flandre, Denis ; Francis, Laurent. MA thesis. Ecole polytechnique de Louvain, Université catholique de Louvain, 2019. URL: http://hdl.handle.net/2078.1/thesis:19433.

[65] *Physik instrumente - Stack multilayer piezo actuators datasheet*. URL: https://www.pi-usa.us/en/products/piezo-actuators-stacks-benders-tubes/p-882-p-888-picma-stack-multilayer-piezo-actuators-100810.

[66] Minhang Bao. “Chapter 1 - Introduction to MEMS Devices”. In: *Analysis and Design Principles of MEMS Devices*. Ed. by Minhang Bao. Amsterdam: Elsevier Science, 2005, pp. 1–32. ISBN: 978-0-444-51616-9. DOI: https://doi.org/10.1016/B978-044451616-9/50002-3. URL: https://www.sciencedirect.com/science/article/pii/B9780444516169500023.

[67] Author names (you should add the correct author names here). “The Plane Strain Young’s Modulus in Cubic Materials”. In: *Journal of Elasticity* 128 (Jan. 2017), pp. 147–173. DOI: 10.1007/s10659-017-9621-x. URL: https://doi.org/10.1007/s10659-017-9621-x.

[68] Toshiyuki Toriyama, Yoshihiko Yokoyama, and Susumu Sugiyama. “Isotropic piezoresistance in polycrystalline silicon for in-plane shear-and normal-stress gauges”. In: *Sensors and materials* 12.8 (2000), pp. 473–490.

[69] A. E. H. T. “(1) Lehrbuch der Kristallphysik (mit Ausschluss der Kristalloptik) (2) Leçons de Cristallographie (3) Die Kristallgruppen nebst ihren Beziehungen zu den Raumgittern”. In: *Nature* 86.2173 (June 1911). ISSN: 1476-4687. DOI: 10.1038/086544a0. URL: https://doi.org/10.1038/086544a0.

[70] *SNU open courseware Seoul National University - MEMS lecture 23 - Piezoresistive pressure sensor*. URL: https://ocw.snu.ac.kr/sites/default/files/NOTE/5374.pdf (visited on 07/18/2024).

[71] Kuan Lu et al. “Thermomechanical reliability of through-silicon vias in 3D interconnects”. In: *IEEE International Reliability Physics Symposium Proceedings* (Apr. 2011). DOI: 10.1109/IRPS.2011.5784487.

[72] Bharat Bhushan, ed. *Encyclopedia of Nanotechnology*. 2nd ed. Springer, 2016. ISBN: 978-94-017-9780-1. DOI: 10.1007/978-94-017-9780-1.

[73] Björn Richter, Jens Twiefel, and Jörg Wallaschek. “Piezoelectric Equivalent Circuit Models”. In: *Energy Harvesting Technologies*. Ed. by Shashank Priya and Daniel J. Inman. Boston, MA: Springer US, 2009, pp. 107–128. ISBN: 978-0-387-76464-1. DOI: 10.1007/978-0-387-76464-1_4. URL: https://doi.org/10.1007/978-0-387-76464-1_4.

[74] D W Dye. “The piezo-electric quartz resonator and its equivalent electrical circuit”. In: *Proceedings of the Physical Society of London* 38.1 (Jan. 1925), p. 399. DOI: 10.1088/1478-7814/38/1/344. URL: https://dx.doi.org/10.1088/1478-7814/38/1/344.

[75] *BCM sensor website*. URL: https://www.bcmsensor.com/ (visited on 07/18/2024).

[76] Amr A. Balbola, Mohammed O. Kayed, and Walied A. Moussa. “Studying the Influence of n-Type Strained (111) Silicon on the Piezoresistive Coefficients”. In: *IEEE Sensors Journal* 17.2 (2017), pp. 302–310. DOI: 10.1109/JSEN.2016.2616759.

[77] Wei-Wei Zhang et al. “Modelling of the elastic properties of crystalline silicon using lattice dynamics”. In: *Journal of Physics D: Applied Physics* 44 (Aug. 2011), p. 335401. DOI: 10.1088/0022-3727/44/33/335401.

[78] W. Merlijn van Spengen. "The electromechanical damping of piezo actuator resonances: Theory and practice". In: *Sensors and Actuators A: Physical* 333 (2022), p. 113300. ISSN: 0924-4247. DOI: https://doi.org/10.1016/j.sna.2021.113300. URL: https://www.sciencedirect.com/science/article/pii/S0924424721007639.

[79] Diego Stutzer et al. "Characterization and modeling of a planar ultrasonic piezoelectric transducer for periodontal scalers". In: *Sensors and Actuators A: Physical* 351 (2023), p. 114131. ISSN: 0924-4247. DOI: https://doi.org/10.1016/j.sna.2022.114131. URL: https://www.sciencedirect.com/science/article/pii/S092442472200766X.

[80] Amelie Bender. "Model-based condition monitoring of piezoelectric bending actuators". In: *Sensors and Actuators A: Physical* 357 (2023), p. 114399. ISSN: 0924-4247. DOI: https://doi.org/10.1016/j.sna.2023.114399. URL: https://www.sciencedirect.com/science/article/pii/S0924424723002480.

[81] S. Sherrit, H.D. Wiederick, and B.K. Mukherjee. "Accurate equivalent circuits for unloaded piezoelectric resonators". In: *1997 IEEE Ultrasonics Symposium Proceedings. An International Symposium (Cat. No.97CH36118)*. Vol. 2. 1997, 931–935 vol.2. DOI: 10.1109/ULTSYM.1997.661733.

[82] Lei Chen and Yao Wang. "Dependence of Modified Butterworth Van-Dyke Model Parameters and Magnetoimpedance on DC Magnetic Field for Magnetoelectric Composites". In: *Materials* 14.16 (2021). ISSN: 1996-1944. URL: https://www.mdpi.com/1996-1944/14/16/4730.

[83] B. Abdelaziz, K. Fouad, and S. Kemouche. "The Effect of Temperature and Doping Level on the Characteristics of Piezoresistive Pressure Sensor". In: *Journal of Sensor Technology* 4 (2014), pp. 59–65. DOI: 10.4236/jst.2014.42007.

[84] Y. Kanda. "A graphical representation of the piezoresistance coefficients in silicon". In: *IEEE Transactions on Electron Devices* 29.1 (1982), pp. 64–70. DOI: 10.1109/T-ED.1982.20659.

[85] Chegg. *Plot shows the carrier concentration as a function of temperature for extrinsic p-type Si and intrinsic Si.* Accessed: 2024-08-10. 2024. URL: https://www.chegg.com/homework-help/questions-and-answers/plot-shows-carrier-concentration-function-temperature-extrinsic-p-type-si-intrinsic-si-lab-q97328976#question-transcript.

[86] E.D.H. Green. *Temperature Dependence of Semiconductor Conductivity.* San Jose State University, Materials Engineering 25, LabNotes. Accessed: 2024-08-10. n.d. URL: https://www.iiserkol.ac.in/~ph324/StudyMaterials/ResistivityTdep.pdf.

[87] M. Aryafar, Mohsen Hamedi, and Mohammad Maghsoudi Ganjeh. "A novel temperature compensated piezoresistive pressure sensor". In: *Measurement* 63 (Mar. 2015). DOI: 10.1016/j.measurement.2014.11.032.

[88] J.J. Tzou et al. “The temperature dependence of threshold voltages in submicrometer CMOS”. In: *IEEE Electron Device Letters* 6.5 (1985), pp. 250–252. DOI: 10.1109/EDL.1985.26114.

[89] The Engineering ToolBox. *Thermal Expansion - Linear Expansion Coefficients*. https://www.engineeringtoolbox.com/linear-expansion-coefficients-d_95.html. (Visited on 08/15/2024).

[90] H. Watanabe, Naofumi Yamada, and Masahiro Okaji. “Linear Thermal Expansion Coefficient of Silicon from 293 to 1000 K”. In: *International Journal of Thermophysics* 25 (Jan. 2004), pp. 221–236. DOI: 10.1023/B:IJOT.0000022336.83719.43.

[91] Matthew A. Hopcroft, William D. Nix, and Thomas W. Kenny. “What is the Young’s Modulus of Silicon?” In: *Journal of Microelectromechanical Systems* 19.2 (2010), pp. 229–238. DOI: 10.1109/JMEMS.2009.2039697.

[92] Steve Vanlanduit et al. “Strain Monitoring”. In: *Structural Health Monitoring Damage Detection Systems for Aerospace*. Ed. by Markus G. R. Sause and Elena Jasiūnienė. Cham: Springer International Publishing, 2021, pp. 219–241. ISBN: 978-3-030-72192-3. DOI: 10.1007/978-3-030-72192-3_8. URL: https://doi.org/10.1007/978-3-030-72192-3_8.

[93] Hongwei Guo et al. “Fiber optic sensors for structural health monitoring of air platforms”. In: *Sensors (Basel)* 11.4 (2011), pp. 3687–3705. DOI: 10.3390/s110403687. URL: https://doi.org/10.3390/s110403687.

[94] Yu-Yin Chen et al. “A self-powered switching circuit for piezoelectric energy harvesting with velocity control”. In: *The European Physical Journal Applied Physics* 57 (Mar. 2012), p. 30903. DOI: 10.1051/epjap/2012110355.

[95] Mohammad Motamedi. *Nonlinear Vibration Analysis of Cracks in Aerospace Structures*. Feb. 2019.

[96] Yu Xu et al. “A Novel Piezoresistive Accelerometer with SPBs to Improve the Tradeoff between the Sensitivity and the Resonant Frequency”. In: *Sensors* 16.2 (2016). ISSN: 1424-8220. DOI: 10.3390/s16020210. URL: https://www.mdpi.com/1424-8220/16/2/210.

[97] Khaled Ahmida and J.R.F. Arruda. “On the relation between complex modes and wave propagation phenomena”. In: *Journal of Sound and Vibration - J SOUND VIB* 255 (Aug. 2002), pp. 663–684. DOI: 10.1006/jsvi.2001.4183.

[98] Saad Alkhfaji and Seamus Garvey. “Identification of Piezoelectric Actuators Using a Simple Test Technique”. In: Sept. 2010.

[99] Dennis Fitzpatrick. “Chapter 14 - Noise Analysis”. In: *Analog Design and Simulation using OrCAD Capture and PSpice*. Ed. by Dennis Fitzpatrick. Oxford: Newnes, 2012, pp. 175–185. ISBN: 978-0-08-097095-0. DOI: https://doi.org/10.1016/B978-0-08-097095-0.00014-3. URL: https://www.sciencedirect.com/science/article/pii/B9780080970950000143.

[100] Min Tae Kim. “Influence of substrates on the elastic reaction of films for the microindentation tests”. In: *Thin Solid Films* 283.1 (1996), pp. 12–16. ISSN: 0040-6090. DOI: https://doi.org/10.1016/0040-6090(95)08498-3. URL: https://www.sciencedirect.com/science/article/pii/0040609095084983.

[101] K.S. Van Dyke. “The Piezo-Electric Resonator and Its Equivalent Network”. In: *Proceedings of the Institute of Radio Engineers* 16.6 (1928), pp. 742–764. DOI: 10.1109/JRPROC.1928.221466.

UNIVERSITÉ CATHOLIQUE DE LOUVAIN
École polytechnique de Louvain
Rue Archimède, 1 bte L6.11.01, 1348 Louvain-la-Neuve, Belgique | **www.uclouvain.be/epl**